2020-06-11

Microfabricated Fluidic Devices for Biological Assays and Bioelectronics

Anna V. Bickham
Brigham Young University

Microfabricated Fluidic Devices for Biological Assays and Bioelectronics

Anna V. Bickham

A dissertation submitted to the faculty of
Brigham Young University
in partial fulfillment of the requirements for the degree of

Doctor of Philosophy

Adam T. Woolley, Chair
Gregory P. Nordin
Daniel E. Austin
Ryan T. Kelly

Department of Chemistry and Biochemistry

Brigham Young University

ABSTRACT

Microfabricated Fluidic Devices for Biological Assays and Bioelectronics

Anna V. Bickham
Department of Chemistry and Biochemistry, BYU
Doctor of Philosophy

Microfluidics miniaturizes many benchtop processes and provides advantages of low cost, reduced reagent usage, process integration, and faster analyses. Microfluidic devices have been fabricated from a wide variety of materials and methods for many applications. This dissertation describes four such examples, each employing different features and fabrication methods or materials in order to achieve their respective goals.

In the first example of microfluidic applications in this dissertation, thermoplastics are hot embossed to form t-shaped channels for microchip electrophoresis. These devices are used to separate six preterm birth (PTB) biomarkers and establish a limit of detection for each. The next chapter describes 3D printed devices with reversed-phase monoliths for solid-phase extraction and on-chip fluorescent labeling of PTB biomarkers. I demonstrate the optimization of the monolith and selective retention of nine PTB biomarkers, the first microchip study to perform an analysis on this entire panel. The third project describes the iterative design and fabrication of glass/polydimethylsiloxane (PDMS) devices with gold and nickel electrodes for the self-assembly of DNA nanotubes for site-selective placement of nanowires. Simple flow channels and "patch electrode" devices were successfully used, and DNA seeding was achieved on gold electrodes. Finally, a 3D printed device for cancer drug screening was developed as a replacement for one previously fabricated in PDMS. Devices of increasing complexity were fabricated, and those tested found to give good control over fluid flow for multiple inlets and valves.

Although the applications and methods of these projects are varied, the work in this dissertation demonstrates the potential of microfluidics in several fields, particularly for diagnostics, therapeutics, and nanoelectronics. Furthermore, it demonstrates the importance of applying appropriate tools to each problem to gain specific advantages. Each of the described devices has the potential for increased complexity and integration, which further emphasizes the advantages of miniaturized analyses and the potential for microfluidics for analytical testing in years to come.

Keywords: microfluidics, preterm birth, electrophoresis, solid-phase extraction, nanoelectronics, cancer therapeutics, point-of-care, 3D printing, porous polymer monolith

ACKNOWLEDGEMENTS

First, I would like to thank my family for always being there for me, specifically my parents for teaching me and helping me to become the person that I am, my siblings for always being there when I need a friend, and my husband Bryce for all of his help and support.

I'd also like to thank my advisor, Adam Woolley, for all of the training and growth I've had in his lab. I feel very fortunate to have been able to work with Adam and have appreciated both his guidance and the freedom to follow through with my ideas while working in his lab. Thanks also to Greg Nordin, whom I've also worked with closely the past few years. Greg has been very supportive of my research and I appreciate the input he has provided. I'd also like to thank the other faculty at BYU that have given me their time and support, particularly my other committee members: Daniel Austin, Matthew Linford, Paul Farnsworth, and Ryan Kelly.

Next, I'd like to thank all of the amazing people I've been able to work with. Many of them have become my friends and lightened the load including Mike Beauchamp, Ellen Parker, Robert Hansen, Haifa Almughamsi, and many others. Additionally, few people are lucky enough to work with their family, and I've been doubly lucky to work with my brother Jacob and my husband Bryce for several years.

Finally, I'd like to thank the funding sources that have paid for my graduate work. I've been supported by the National Institutes of Health (R01 EB006124 and R01 EB027096), the National Science Foundation (Grant #1562729) and several awards provided by the BYU Department of Chemistry and Biochemistry including the Nicholes-Maw New Graduate Fellowship, J. Rex and Marcia A. Goates Graduate Fellowship, Roland K Robins Graduate Research Fellowship, and Garth Lee Graduate Research Fellowship.

TABLE OF CONTENTS

LIST OF TABLES

LIST OF FIGURES

1. INTRODUCTION*

1.1 Microfluidics

A consistent driving force for many scientific advances has been to develop cheaper, easier, or more reliable technologies. Indeed, these specific ideas have interwoven many of the advances that led to the development of microfluidics and the miniaturization of laboratory processes to create lab-on-a-chip technologies and point-of-care diagnostics. Since the inception of microfluidics over 30 years ago,[1-3] the field has grown to encompass a variety of materials, methods, and applications, with thousands of articles being published each year.

Microfluidics are a popular methodology for many analyses compared to conventional benchtop methods due to the advantages of reduced cost, low reagent and sample consumption, and faster analyses. These advantages are especially prominent in genetics, proteomics, cellular assays, and point-of-care diagnostics.[4] This range of applications has also resulted in an increase in microfluidic device complexity as more processes are integrated onto a single platform,[5-7] as well as a number of commercialized point-of-care diagnostics.[8-10]

In this chapter, I discuss microfabrication methods and materials used for microfluidic device creation with particular focus on those methods and materials which are applied in chapters 2-4 of this dissertation. I also discuss a few of the experimental methods used to perform the research in this dissertation. Although each of these topics could be discussed in

---

* Section 1.2.3 and Figure 1.1 of this chapter are adapted with permission from the following:
- Nielsen, A. V.; Beauchamp, M. J.; Nordin, G. P.; Woolley, A. T. 3D printed microfluidics. *Annu. Rev.* **2020,** *13*, DOI: 10.1146/annurev-anchem-091619-102649.
- Nielsen, A. V.; Woolley, A. T. Device fabrication and fluorescent labeling of preterm birth biomarkers for microchip electrophoresis. In *Clinical Applications of Capillary Electrophoresis: Methods and Protocols*; Phillips, T. M.; Ed.; New York, 2019; 1972, pp. 175-184.

much greater detail than will be included here, each of these topics constitutes important background information for the research I have performed.

1.2 Fabrication and Materials

Since many of the advantages of microfluidics are due to the reduced feature size in the analytical devices, microfabrication method and material choice are a critical part of developing a microfluidic device. Current methods to produce microfluidic devices include micromachining, micromilling, hot embossing, injection molding, micropatterning, and 3D printing. These methods have been applied to many materials including silicon, glass, silicones, plastics, and paper. The variety, advantages, and reason for development of these materials have been reviewed many times.[11-13] Here, I will only discuss in detail those methods and materials which are most relevant to the work presented in this dissertation: polydimethylsiloxane (PDMS), thermoplastics, and 3D printing.

1.2.1 PDMS

Micropatterning of PDMS via soft lithography was first introduced in the late 1990s as an alternative to difficult glass and silicon micromachining.[14-15] Since then, the ease that PDMS yields to microfabrication has made it the most popular material choice for microfluidics. Fabrication via soft lithography involves cast molding, or the pouring of an unpolymerized PDMS mixture onto a micropatterned surface. After forming to the surface shape, the polymer can be cured to a solidified state and carefully peeled off of the surface, revealing a patterned piece of PDMS.[16] This method of device patterning is simple and allows a single mold to be reused many times, reducing the cost of fabrication and exposure to harsh chemicals. If enclosed

features are desired, PDMS surfaces can be bonded to each other or to glass either reversibly using van der Waals interactions or permanently via treatment with oxygen plasma.[16]

PDMS is a useful material for biological applications for several reasons in addition to simple fabrication. First, PDMS is naturally biocompatible and gas permeable, lending the material easily to cellular applications. Indeed, PDMS is the most popular material choice for microfluidic-based cellular studies because many other materials lack these properties. Additionally, the rubbery flexibility of PDMS has allowed for fabrication of membrane-based valves and pumps for fluid control,[17-19] which is not available in many other materials. Even if the bulk of the microfluidic device is constructed from another material, many researchers embed a PDMS membrane for valve construction,[20-21] because PDMS so easily yields itself to the flexibility and durability properties needed for such features.

Despite its wide usage within microfluidics, PDMS also comes with many disadvantages.[15,22] The polymer structure is prone to swelling in organic solvents and absorption of small molecules. This is especially detrimental for applications that require long analysis times or in which analyte concentrations are already low. Additionally, the process of soft lithography is relatively manual, lending itself well to prototyping but not industrial production.[23] This, in combination with a lack of device feature and interfacing standardization, has resulted in a large number of microfluidic applications which are unable to reach a marketable status because the manufacturing hurdle is too great to surpass.[24]

1.2.2 Thermoplastics

Around the same time as PDMS was first used, plastic materials were also making their debut to simplify microfluidic device fabrication. Some of the earliest thermoplastic microfluidic devices and fabrication methods included hot embossing of poly(methyl methacrylate)

(PMMA),[25] injection molding of an acrylic copolymer,[26] and laser photoablation of polystyrene, polycarbonate, cellulose acetate, and poly(ethylene terephthalate).[27] Since these early studies, a large variety of other thermoplastics including cyclic olefin (co)polymer, polyethylene, polypropylene, polyvinyl chloride, polyamide, polysulfone, polylactic acid, polytetrafluoroethylene, polyetherketone, and acrylonitrile butadiene styrene and fabrication methods including photolithography, etching, sputtering, micromilling, and CNC machining have been used to create microfluidic devices.[28]

One of the greatest advantages of thermoplastic microfluidics is the variety of plastics available. In addition to those plastics already mentioned, advances are being made with new and more versatile materials.[29-31] This variety has allowed each application to be matched to the best suited material, thus easing the transition of many macro-plastic processes, particularly biological applications, into the realm of microfluidics.[22,32] Unfortunately, material matching has also resulted in insufficient standardization in fabrication and fluidic design, which can complicate commercialization. However, the use of thermoplastics greatly eases the transition of many microfluidic applications into industrial-scale production,[33] and thermoplastics continue to be popular microfluidic device materials.

1.2.3 3D Printing

One technique that has recently gained traction for fabricating microdevices is 3D printing, which offers several advantages over traditional fabrication techniques. Designs for 3D prints are easily edited and reprinted, thus allowing for testing-based optimization. Additionally, 3D printed devices do not require a cleanroom fabrication environment. The consumables for 3D printing are often only the resin and solvent to remove support materials, so costs can be low.

Finally, 3D printing can fully utilize all three dimensions in device architecture, which should allow unique capabilities to be realized.

There are many types of 3D printers commercially available which can print fluidic features >200 μm including using stereolithography (SLA), PolyJet (PJ), or fused deposition modeling (FDM) 3D printers. Many excellent reviews are available describing the advantages of each of these printing types.[34-36] For many 3D printers, particularly for PJ and FDM, millifluidic features are the smallest that the printer is capable of producing.[37] Though many manufacturers advertise <100-μm resolution, deliverable fluidic feature size is typically many times larger than that. This is particularly true for internal features, which are significantly more difficult to create than surface structures. This discrepancy primarily exists because the creation of tiny features is not only dependent upon printer specifications (i.e., motor step size, nozzle diameter, pixel size, etc.), but also on the print material, the location and shape of the fluidic features being printed, and a host of parameters specific to the printer type (e.g., infill rate, light source power and wavelength, motor speed, etc.).

One of the most promising areas for 3D printing microfluidic devices involves using digital light processing (DLP)-based SLA. DLP-SLA functions by photopolymerizing a liquid polymer resin, one layer at a time, to form a 3D object. The polymer resin usually consists of a monomer, photoinitiator, and UV absorber. It is important that the latter two components be spectrally matched to the DLP light source, both to allow effective polymerization of the resin and to limit light penetration into void regions to allow formation of small, enclosed features.[38] Several groups have successfully leveraged DLP-SLA light sources[39-42] or custom printers and printing materials[39,43-44] to embed microfluidic structures with features routinely <50 μm. At

present, spectral matching of a DLP-SLA printer with the printing material is the only 3D printing method able to achieve truly microfluidic devices.

1.3 Microfluidic Methods and Features

Because microfluidic devices have been developed for such a wide variety of applications, a large number of methods and features have also been developed to accomplish these goals. Some of these tools can be incorporated using only the channel geometry while others require external connections or additional device processing to add a structure prior to usage. A few microfluidic methods and features which are most relevant to the work in this dissertation are discussed here, including microchip electrophoresis, porous polymer monoliths, droplet microfluidics, and valves and pumps.

1.3.1 Microchip Electrophoresis

Microchip electrophoresis (μCE), a miniaturized electrophoretic separation method, was one of the earliest applications of microfluidics.[45] The miniaturized form of capillary electrophoresis (CE), μCE is considered to be more convenient and simple than the benchtop form, offering potential advantages of portability, high-throughput, and cost effectiveness.[46] Additionally, the injection volume to perform a μCE separation is very small, allowing analysis of precious samples. However, some analytes and microchip materials are more prone to adsorption, making detection of these small sample volumes more difficult.[47] Furthermore, the reduced channel length compared to a traditional CE capillary can lead to a reduction in separation efficiency, making it more difficult to analyze complex samples.[48]

Similar to CE, analytes in μCE are primarily separated by size and charge. Figure 1.1 shows a typical μCE setup in which a simple t-shaped device is filled with buffer. Sample is injected when a low electric field is applied, and a small plug in the intersection is separated when a high electric field is applied to the separation channel. Analyte velocity is affected by the applied separation electric field, and the best separation efficiencies are usually achieved by maximizing the applied voltage while minimizing Joule heating.[45,49] Analyte mobility is further affected via electroosmotic flow by the surface properties of the separation channel, as determined by the device material and separation buffer. However, the electroosmotic flow can be altered by applying a surface modification. Dynamic coatings are more popular for plastic devices and are applied by adding a polymer or surfactant to the running buffer. Permanent modifications are more stable and don't require replenishing, but they are more laborious to apply. These permanent modifications are more commonly used for glass and silicon devices

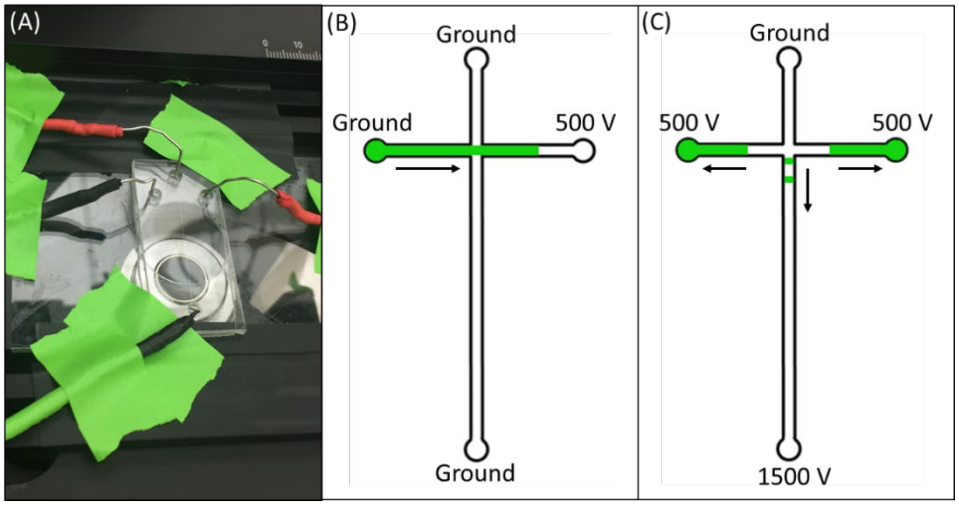

Figure 1.1. μCE device and electrode setup for voltage application. (A) Photograph of device and Pt electrode placement. (B) Schematic for injection voltage application. (C) Schematic for separation voltage application. Voltages other than those pictured here (500 and 1500 V) may be used, but the injection voltage should be lower than the separation voltage. Arrows indicate the flow direction of the green sample.

because they are generally considered less disposable and the surface modification chemistries are well known.[47]

μCE has been applied in the separation of many molecules including lipids, carbohydrates, nucleic acids, proteins, small molecules, and even cells for applications in biomarker analyses, pharmaceuticals, and biomedical research.[46,50-52] The broad usefulness of μCE has led to marketing of both μCE devices and complete μCE systems by several companies including PerkinElmer (LabChip), Shimadzu (MultiNA), and Agilent (2100 Bioanalyzer), . These applications have also made μCE a good choice for fast, quantitative separation and detection of analytes.[53]

1.3.2 Porous Polymer Monoliths

Monoliths are porous polymer structures that can be polymerized inside a capillary or microfluidic channel as a solid support structure for analytical applications. Monoliths are usually fabricated from either silica or organic polymers[54] and were originally developed for chromatography. Beyond chromatographic separation, monoliths have also found usage for extraction, microreactors (catalysis), and as scaffolds for tissue engineering.[55]

Monoliths are often advantageous as a replacement for a packed bead bed because they allow for *in situ* preparation, low back pressures, and no frit requirement due to secure wall anchoring.[54,56] Their most common disadvantages include monomer-dependent swelling in organic solvents and column capacity compared to other sorbent materials like packed silica beads.[56-57] However, this surface area difference is mainly due to analyte mass transfer ability, meaning that monoliths usually perform better for large mass molecules while packed beds are better for small molecules.

Monolith morphology is characterized primarily by pore size (macro- and meso-pores) and polymerized nodules (size and shape). This characterization is significant because morphology can affect the efficiency of the analytical process being performed.[58] For example, the presence of mesopores may enhance the performance of a chromatographic separation but hinder the effectiveness of confocal microscope imaging. While morphology can be tuned by changing the monolith recipe, it is important that characterization of a particular recipe only occur if the monolith has been treated under the same conditions as it will be used for in experiments; polymerization in a microchip or capillary can yield significantly different morphological features than polymerization in bulk solutions or suspensions.[56-57]

1.3.3 Droplet Microfluidics

Droplet microfluidics is the use of reagent and sample droplets enclosed within another fluidic phase, usually formed and manipulated inside of microfluidic channels. This branch of microfluidics was originally developed in order to create a high-throughput system to perform large number of analyses simultaneously as each droplet functions as an individual, isolated reaction chamber.[59-60] Because the droplets have a high surface area-to-volume ratio, chemical reactions can be performed faster due to rapid diffusion and heat and mass transfer rates.[61] Droplets can also be mixed, sorted, fused, split, or otherwise manipulated by flowing through different channel geometries or exposure to an electromagnetic field.[61]

Many studies have been performed demonstrating the ability to generate different sizes and numbers of droplets within microfluidic devices. These droplets can be created either actively by utilizing an electric, magnetic, or centrifugal field, or passively by utilizing channel geometry, fluid properties (velocity, viscosity, and surface tension), or device material properties (wettability and surface tension).[62] The most important feature is that the two fluid phases cannot

be miscible; two flows must have some kind of interfacial instability to allow droplet formation rather than co-flow or mixing, and the fluid flow must be laminar.[61]

Droplet microfluidics have been applied to many fields including chemical kinetics, protein crystallization, organic synthesis, nanoparticle synthesis, and microextraction.[63-64] However, one of the most important applications of droplets is for single-cell analysis. Although these single-cell assays sometimes require extra considerations to maintain cell viability (e.g., feeding, gas exchange, waste removal, etc.),[65] droplets enable many studies into the genomic, proteomic, epigenomic, metabolomic, and biophysical (mechanical and electrical) properties of isolated cells.[66-67] These single-cell analyses are particularly insightful as high-throughput, time-dependent, or high-replicate experiments when coupled to a high-throughput detection method such as barcoding.[69-70]

1.3.4 Valves and Pumps

Microfluidic integration often requires the increased fluid flow control achieved with on-chip valves and pumps. A large number of valving methods have been applied to microfluidics including piston, bubble, capillary, hydrogel, pneumatic, electrostatic, time-delayed, check, and electrowetting,[71-72] and most can also be placed and actuated in series to create fluid pumps. Each valving method lends itself more easily to specific fabrication methods and materials, and each gives specific advantages to corresponding applications.

The first pneumatic valves, termed "Quake valves,"[17] were constructed from PDMS and remain one of the most popular choices for microfluidic devices. However, other normally-open pneumatic valve designs are used include the plunger valve,[19] lateral deflection valve,[73] and line valve.[74] Additionally, normally-closed valves such as doormat,[75] curtain,[76] or lifting-gate[18] valves can be used if vacuum is used in place of pressure in the control channel.

As mentioned in Section 1.2.1, most pneumatic valves are fabricated from PDMS because the material is flexible and durable enough to allow for repeated actuation of a thin (often 5-15 μm) membrane. However, other materials can achieve similar results. For example, the Nordin lab at BYU recently created 1-mm diameter lateral deflection valves in 3D printed devices using a custom poly(ethylene glycol) diacrylate (PEGDA)-based resin.[77] They have since demonstrated the ability to shrink these valves to 300-μm diameter and to pack them tightly to create mixer pumps.[78] I anticipate future integration of these valves into several of the projects described in this dissertation.

1.4 Dissertation Overview

The use of microfluidics offers the potential for many benchtop, diagnostic, and manual processes to be miniaturized, automated, and integrated on a single platform. The number of fabrication methods, materials, and applications that have been applied to microfluidics has only scratched the surface of what may be possible in the future. This dissertation describes several microfluidics-based projects that demonstrate these capabilities. Each utilizes different microfabrication techniques to realize applications in biological assays or bioelectronics.

In Chapter 2, I describe the development of a microchip electrophoresis method to separate six peptide and protein preterm birth (PTB) biomarkers. Several separation buffers and applied voltages were tested to establish conditions that could include this many of the biomarkers. Electrophoretic separations were performed in COC devices with a photografted surface inside the channels to reduce electroosmotic flow. This separation was an important step to detect multiple PTB biomarkers preliminary to creating a complete PTB diagnostic test.

In Chapter 3, the development of a reversed-phase monolith for the solid-phase extraction of peptide and protein PTB biomarkers is described. The PTB biomarkers are selectively retained

on the monolith during flow through and on-chip labeling experiments. The microfluidic devices used for this work were 3D printed using the custom 3D printer and resin described in the literature.[39] The work described in this chapter is also the first time all nine biomarkers in this PTB risk biomarker panel have been used in a microchip analysis.

In Chapter 4, I describe the process of iterative improvements to a microfluidic device design to build up to a complete, integrated device. I describe two different projects that followed this approach and were performed in collaboration with other research institutions. The first project involves the fabrication of fluidic devices that have embedded gold and nickel electrodes for the seeding and growth of DNA nanotubes and their eventual metallization into nanowires. The fluidic devices were fabricated from glass and PDMS with gold and nickel electrodes for testing of the nanowire electrical properties. The second project involves the transition of a PDMS droplet microfluidic device for high-throughput cancer drug testing to a 3D printed design. This project highlights the design considerations and improvements inherent to 3D printing compared to conventional microfabrication.

In Chapter 5, I summarize conclusions from the previous three chapters. I also describe promising future directions for each project for continued improvement and integration with other microfluidic features.

1.5 References

1. Terry, S. C.; Jerman, J. H.; Angell, J. B. A gas chromatographic air analyzer fabricated on a silicon wafer. *IEEE Trans. Electron Devices* **1979,** *26,* 1880-1886.

2. Manz, A.; Miyahara, Y.; Miura, J.; Watanabe, Y.; Miyagi, H.; Sato, K. Design of an open-tubular column liquid chromatograph using silicon chip technology. *Sens. Actuators* **1990,** *B1,* 249-255.

3. Manz, A.; Graber, N.; Widmer, H. M. Miniaturized total chemical analysis systems: a novel concept for chemical sensing. *Sens. Actuators* **1990,** *B1,* 244-248.

4. Chiu, D. T.; DeMello, A. J.; Di Carlo, D.; Doyle, P. S.; Hansen, C.; Maceiczyk, R. M.; Wootton, R. C. R. Small but perfectly formed? Successes, challenges, and opportunities for microfluidics in the chemical and biological sciences. *Chem* **2017,** *2,* 201-223.

5. Kaminski, T. S.; Garstecki, P. Controlled droplet microfluidic systems for multistep chemical and biological assays. *Chem. Soc. Rev.* **2017,** *46,* 6210-6226.

6. Pagaduan, J. V.; Bhatta, A.; Romer, L. H.; Gracias, D. H. 3D hybrid small scale devices. *Small* **2018,** *14,* 1702397.

7. Sibbitts, J.; Sellens, K. A.; Jia, S. Klasner, S. A.; Culbertson, C. T. Cellular analysis using microfluidics. *Anal. Chem.* **2018,** *90,* 65-85.

8. Chin, C. D.; Linder, V.; Sia, S. K. Commercialization of microfluidic point-of-care diagnostic devices. *Lab Chip* **2012,** *12,* 2118-2134.

9. Volpatti, L. R.; Yetisen, A. K. Commercialization of microfluidic devices. *Trends Biotechnol.* **2014,** *32,* 347-350.

10.Becker, H.; Gärtner, C. Microfluidics-enabled diagnostic systems: markets, challenges, and examples. In: *Microchip diagnostics. Methods in molecular biology;* Taly, V.; Viovy, J. L.; Descroix, S.; Eds.: New Jersey, **2017;** 1547, pp. 3-21.

11. Nielsen, J. B.; Hanson, R. L.; Almughamsi, H. M.; Pang, C.; Fish, T. R.; Woolley, A. T. Microfluidics: innovations in materials and their fabrication and functionalization. *Anal. Chem.* **2020,** *92,* 150-168.

12. Nge, P. N.; Rogers, C. I.; Woolley, A. T. Advances in microfluidic materials, functions, integration, and applications. *Chem. Rev.* **2013,** *113,* 2550-2583.

13. Ren, K.; Zhou, J.; Wu, H. Materials for microfluidic chip fabrication. *Acc. Chem. Res.* **2013,** *46,* 2396-2406.

14. Effenhauser, C. S.; Bruin, G. J. M.; Paulus, A.; Ehrat, M. Integrated capillary electrophoresis on flexible silicone microdevices: analysis of DNA restriction fragments and detection of single DNA molecules on microchips. *Anal. Chem.* **1997,** *69,* 3451-3457.

15. Xia, Y.; Whitesides, G. M. Soft lithography. *Annu. Rev. Mater. Sci.* **1998,** *28,* 153-184.

16. McDonald J. C.; Duffy, D. C.; Anderson, J. R.; Chiu, D. T.; Wu, H.; Schueller, O. J. A.; Whitesides, G. M. Fabrication of microfluidic systems in poly(dimethylsiloxane). *Electrophoresis* **2000,** *21,* 27-40.

17. Unger, M. A.; Chou, H.; Thorsen, T.; Scherer, A.; Quake, S. R. Monolithic microfabricated valves and pumps by multilayer soft lithography. *Science* **2000,** *288,* 113-116.

18. Kim, J.; Kang, M.; Jensen, E. C.; Mathies, R. A. Lifting gate polydimethylsiloxane microvalves and pumps for microfluidic control. *Anal. Chem.* **2012,** *84,* 2067-2071.

19. Baek, J. Y.; Park, J. Y.; Ju, J. I.; Lee, T. S.; Lee, S. H. A pneumatically controllable flexible and polymeric microfluidic valve fabricated via *in situ* development. *J. Micromech. Microeng.* **2005,** *15,* 1015-1020.

20. Grover, W. H.; Skelley, A. M.; Liu, C. N.; Lagally, E. T.; Mathies, R. A. Monolithic membrane valves and diaphragm pumps for practical large-scale integration into glass microfluidic devices. *Sens. Actu. B* **2003,** *89,* 315-323.

21. Zhang, W.; Lin, S.; Wang, C.; Hu, J.; Li, C.; Zhuang, Z.; Zhou, Y.; Mathies, R. A.; Yang, C. J. PMMA/PDMS valves and pumps for disposable microfluidics. *Lab Chip* **2009,** *9,* 3088-3094.

22. Berthier, E.; Young, E. W. K.; Beebe, D. Engineers are from PDMS-land, biologists are from polystyrenia. *Lab Chip* **2012,** *12,* 1224-1237.

23. Mohammed, M. I.; Haswell, S.; Gibson, I. Lab-on-a-chip or chip-in-a-lab: challenges of commercialization lost in translation. *Proc. Technol.* **2015,** *20,* 54-59.

24. Volpatti, L. R.; Yetisen, A. K. Commercialization of microfluidic devices. *Trends Biotechnol.* **2014,** *32,* 347-350.

25. Martynova, L.; Lacascio, L. E.; Gaitan, M.; Kramer, G. W.; Christensen, R. G.; MacCrehan, W. A. Fabrication of plastic microfluid channels by imprinting methods. *Anal. Chem.* **1997,** *69,* 4783-4789.

26. McCormick, R. M.; Nelson, R. J.; Alonso-Amigo, M. G.; Benvegnu, D. J.; Hooper, H. H. Microchannel electrophoretic separations of DNA in injection-molded plastic substrates. *Anal. Chem.* **1997,** *69,* 2626-2630.

27. Robert, M. A.; Rossier, J. S.; Bercier, P.; Girault, H. UV laser machined polymer substrates for the development of microdiagnostic systems. *Anal. Chem.* **1997,** *69,* 2035-2042.

28. Gencturk, E.; Mutlu, S.; Ulgen, K. O. Advances in microfluidic devices made from thermoplastics used in cell biology and analyses. *Biomicrofluid.* **2017,** *11,* 051502.

29. Roy, E.; Stewart, G.; Mounier, M.; Malic, L.; Peytavi, R.; Clime, L.; Madou, M.; Bossinot, M.; Bergeron, M. G.; Veres, T. From cellular lysis to microarray detection, an integrated thermoplastic elastomer (TPE) point of care lab on a disc. *Lab Chip* **2015,** *15,* 406-416.

30. Roy, E.; Galas, J.; Veres, T. Thermoplastic elastomers for microfluidics: towards a high-throughput fabrication method of multilayered microfluidic devices. *Lab Chip* **2011,** *11,* 3193-3196.

31. Begolo, S.; Colas, G.; Viovy, J.; Malaquin, L. New family of fluorinated polymer chips for droplet and organic solvent microfluidics. *Lab Chip* **2011,** *11,* 508-512.

32. Ren, K.; Chen, Y.; Wu, H. New materials for microfluidics in biology. *Curr. Opin. Biotechnol.* **2014,** *25,* 78-85.

33. Yang, S.; DeVoe, D. L. Microfluidic device fabrication by thermoplastic hot-embossing. In *Methods in molecular biology (methods and protocols)*; Jenkins, G.; Mansfield, C.; Eds.: New Jersey, **2013;** 949, pp. 115-123.

34. Waheed, S.; Cabot, J. M.; Macdonald, N. P.; Lewis, T.; Guijt, R. M.; Breadmore, M. C. 3D printed microfluidic devices: enablers and barriers. *Lab Chip* **2016,** *16,* 1993-2013.

35. Bhattacharjee, N.; Urrios, A.; Kang, S.; Folch, A. The upcoming 3D-printing revolution in microfluidics. *Lab Chip* **2016,** *16,* 1720-1742.

36. Dixit, C. K.; Kadimisetty, K.; Rusling, J. 3D-printed miniaturized fluidic tools in chemistry and biology. *Trend. Anal. Chem.* **2018,** *106,* 37-52.

37. Beauchamp, M. J.; Nordin, G. P.; Woolley, A. T. Moving from millifluidic to truly microfluidic sub-100-μm cross-section 3D printed devices. *Anal. Bioanal. Chem.* **2017,** *409,* 4311-4319.

38. Gong, H.; Beauchamp, M.; Perry, S.; Woolley, A. T.; Nordin, G. P. Optical approach to resin formulation for 3D printed microfluidics. *RSC Adv.* **2015,** *5,* 106621-106632.

39. Gong, H.; Bickham, B.; Woolley, A. T.; Nordin, G. P. Custom 3D printer and resin for 18 μm x 20 μm microfluidic flow channels. *Lab Chip.* **2017,** *17,* 2899-2909.

40. Jonusauskas, L.; Gailevicius, D.; Rekstyte, S.; Juodkazis, S.; Malinauskas, M. Synchronization of linear stages and galvo-scanners for efficient direct laser fabrication of polymeric 3D meso-scale structures. *Proc. SPIE 10523, Laser 3D Manuf. V,* **2018,** 105230X.

41. Juskova, P.; Ollitrault, A.; Serra, M.; Viovy, J. L.; Malaquin, L. Resolution improvement of 3D stereolithography through the direct laser trajectory programming: application to microfluidic deterministic lateral displacement device. *Anal. Chim. Acta.* **2018,** *1000,* 239-247.

42. Mannel, M. J.; Selzer, L.; Bernhardt, R.; Thiele, J. Optimizing process parameters in commercial microstereolithoraphy for forming emulsions and polymer microparticles in nonplanar microfluidic devices. *Adv. Mater. Technol.* **2018,** *4,* 1800408.

43. Männel, M. J.; Weigel N.; Thiele J. Multifunctional microfluidic devices from tailored photopolymer formulations. *Proc. SPIE 10875, Microfluid., BioMEMS, Medi. Microsyst. XVII,* **2019,** 1087507.

44. Schmid, M. C.; Wussler, D.; Kotz, F.; Rapp, B. E. Wavelength-selective negative photoresist for photolithography suitable for generating microstructures with up to three distinct height levels. *Proc. SPIE 10915, Organic Photonic Mat. Devices XXI,* **2019,** 1091511.

45. Manz, A.; Harrison, D. J.; Verpoorte, E. M. J.; Fettinger, J. C.; Paulus, A.; Lüdi, H.; Widmer, H. M. Planar chips technology for miniaturization and integration of separation techniques into monitoring systems: Capillary electrophoresis on a chip. *J. Chrom.* **1992,** *593,* 253-259.

46. Nuchtavorn, N.; Suntornsuk, W.; Lunte, S. M.; Suntornsuk, L. Recent advances of microchip electrophoresis to biomedical analysis. *J. Pharm. Biomed. Anal.* **2015,** *113,* 72-96.

47. Belder, D.; Ludwig, M. Surface modification in microchip electrophoresis. *Electrophoresis* **2003,** *24,* 3595-3606.

48. Trenerry, V. C.; Rochfort, S. J. Natural products research and metabolomics. In: *Comprehensive Natural Products II;* Liu, H.; Mander, L.; Eds.: Elsevier, **2010,** pp. 595-628.

49. Petersen, N. J.; Nikolajsen, R. P. H.; Mogensen, K. B.; Kutter, J. P. Effect of Joule heating on efficiency and performance for microchip-based and capillary-based electrophoretic separation systems: a closer look. *Electrophoresis* **2004,** *25,* 253-269.

50. Pagaduan, J. V.; Sahore, V.; Woolley, A. T. Applications of microfluidics and microchip electrophoresis for potential clinical biomarker analysis. *Anal. Bioanal. Chem.* **2015,** *407,* 6911-6922.

51. Dolnik, V.; Liu, S. Applications of capillary electrophoresis on microchip. *J. Sep. Sci.* **2005,** *28,* 1994-2009.

52. Castro, E. R.; Manz, A. Present state of microchip electrophoresis: state of the art and routine applications. *J. Chrom. A* **2015,** *1382,* 66-85.

53. Breadmore, M. C. Capillary and microchip electrophoresis: challenging the common conceptions. *J. Chrom. A.* **2012,** *1221,* 42-55.

54. Svec, F. Porous polymer monoliths: Amazingly wide variety of techniques enabling their preparation. *J. Chrom. A.* **2010,** *1217,* 902-924.

55. Knob, R.; Sahore, V.; Sonker, M.; Woolley, A. T. Advances in monoliths and related porous materials for microfluidics. *Biomicrofluid.* **2016,** *10,* 032901.

56. Zou, H.; Huang, X.; Ye, M.; Luo, Q. Monolithic stationary phases for liquid chromatography and capillary electrochromatography. *J. Chrom. A* **2002,** *954,* 5-32.

57. Potter, O. G.; Hilder, E. F. Porous polymer monoliths for extraction: diverse applications and platforms. *J. Sep. Sci.* **2008,** *31,* 1881-1906.

58. Nischang, I. Porous polymer monoliths: Morphology, porous properties, polymer nanoscale gel structure and their impact on chromatographic performance. *J. Chrom. A* **2013,** *1287,* 39-58.

59. Stone, H. A.; Stroock, A. B.; Ajdari, A. Engineering flows in small devices: microfluidics toward a lab-on-a-chip. *Annu. Rev. Fluid Mech.* **2004,** *36,* 381-411.

60. Atencia, J.; Beebe, D. J. Controlled microfluidic interfaces. *Nature* **2005,** *437,* 648-655.

61. Teh, S.; Lin, R.; Hung, L.; Lee, A. P. Droplet microfluidics. *Lab Chip* **2008,** *8,* 198-220.

62. Zhu, P.; Wang, L. Passive and active droplet generation with microfluidics: a review. *Lab Chip* **2017,** *17,* 34-75.

63. Huebner, A.; Sharma, S.; Srisa-Art, M.; Hollfelder, F.; Edel, J. B.; DeMello, A. J. Microdroplets: a sea of applications? *Lab Chip* **2008,** *8,* 1244-1254.

64. Mashaghi, S.; Abbaspourraad, A.; Weitz, D. A.; van Oijen, A. M. Droplet microfluidics: a tool for biology, chemistry, and nanotechnology. *Trends Anal. Chem.* **2016,** *82,* 118-125.

65. Joensson, H. N.; Svahn, H. A. Droplet microfluidics—a tool for single-cell analysis. *Angew. Chem. Int. Ed.* **2012,** *51,* 12176-12192.

66. Matuła, K.; Rivello, F.; Huck, W. T. S. Single-cell analysis using droplet microfluidics. *Adv. Biosys.* **2020,** *4,* 1900188.

67. Wen, N.; Zhao, Z.; Fan, B.; Chen, D.; Men, D.; Wang, J.; Chen, J. Development of droplet microfluidics enabling high-throughput single-cell analysis. *Molecules* **2016,** *21,* 881.

68. Klein, A. M.; Mazutis, L.; Akartuna, I.; Tallapragada, N.; Veres, A.; Li, V.; Peshkin, L.; Weitz, D. A.; Kirschner, M. W. Droplet barcoding for single-cell transcriptomics applied to embryonic stem cells. *Cell* **2015,** *161,* 1187-1201.

69. Lan, F.; Demaree, B.; Ahmed, N.; Abate, A. R. Single-cell genome sequencing at ultra-high-throughput with microfluidic droplet barcoding. *Nat. Biotechnol.* **2017,** *35,* 640-646.

70. Zilionis, R.; Nainys, J.; Veres, A.; Savova, V.; Zemmour, D.; Klein, A. M.; Mazutis, L. Single-cell barcoding and sequencing using droplet microfluidics. *Nat. Protoc.* **2017,** *12,* 44-73.

71. Naik, A.; Zhou, Y. Microfluidic valves. In *ddd* [Online]; Perry, S., Saha, S., Eds. openwetware.org/wiki/Microfluidic_Valves_-_Aditi_Naik,_Yiliang_Zhou (accessed May 26, 2020).

72. Oh, K. W.; Ahn, C. H. A review of microvalves. *J. Micromech. Microeng.* **2006,** *16,* R13-R39.

73. Sundararajan, N.; Kim, D.; Berlin, A. A. Microfluidic operations using deformable polymer membranes fabricated by single layer soft lithography. *Lab Chip* **2005,** *5,* 350-354.

74. Park, C.; Hwang, K.; Jung, W.; Namkoong, K.; Chung, W.; Kim, J.; Huh, N. A PDMS membrane microvalve with one-dimensional line valve seat for robust microfluidics. *J. Micromech. Microeng.* **2014,** *24,* 027002.

75. Hosokawa, K.; Maeda, R. A pneumatically-actuated three-way microvalve fabricated with polydimethylsiloxane using the membrane transfer technique. *J. Micromech. Microeng.* **2000,** *10,* 415-420.

76. Voldman, J.; Gray, M. L.; Schmidt, M. A. An integrated liquid mixer/valve. *J. Microelectromech. Sys.* **2000,** *9,* 295-302.

77. Gong, H.; Woolley, A. T.; Nordin, G. P. High density 3D printed microfluidic valves, pumps, and multiplexers. *Lab Chip* **2016,** *16,* 2450-2458.

78. Gong, H.; Woolley, A. T.; Nordin, A. T. 3D printed selectable dilution mixer pumps. *Biomicrofluid.* **2019,** *13,* 014106.

2. MICROCHIP ELECTROPHORESIS SEPARATION OF A PANEL OF PRETERM BIRTH BIOMARKERS*

2.1 Introduction

Preterm birth (PTB) or birth before the 37th week of gestation is the leading cause of pregnancy-related complications and infant death.[1] The World Health Organization has estimated that over one in ten births is preterm, resulting in over one million infant deaths every year.[2] In addition to the high mortality rates for preterm infants, many struggle with incomplete development of vision, hearing, lungs, heart, or brain. While some of these complications can be resolved with proper intensive care treatment, others will last for the infant's entire life.[3] The cost to care for these complications was at least $26 billion in 2013 in the United States,[4] and these numbers have only increased in recent years.

Many PTB casualties are associated with incomplete development of vital organs. However, it is possible to increase developmental rates in some cases prior to birth if given enough advance notice to administer treatment. For example, treatment with antenatal corticosteroids prior to birth can improve lung development and reduce preterm infant mortality by over 370 thousand deaths annually.[2,5] The challenge is predicting PTB risk before the onset of early labor. While some factors such as environment, high blood pressure, a history of PTB, diabetes, or multiple pregnancies (i.e., twins, triplets, etc.)[6-9] are indicative of higher PTB risk,

---

* This chapter is adapted with permission from:
Nielsen, A. V., Nielsen, J. B., Sonker, M., Knob, R., Sahore, V., Woolley, A. T. Microchip electrophoresis separation of a panel of preterm birth biomarkers. *Electrophoresis* **2018,** *39*, 2300-2307.

there are many cases in which none of these factors is present. Unfortunately, for many women, the first indication of PTB risk is the occurrence of early contractions.

In addition to physical factors, many chemical factors have been studied[10-13] in an attempt to diagnose PTB risk early. Recently, Esplin et al.[14] found three serum peptides indicative of PTB risk. The combined detection of these three peptides and six previously identified protein and peptide biomarkers[9] (Table 2.1) at a gestational age of 28 weeks allowed for the diagnosis of PTB risk with 87% selectivity and 81% specificity four weeks prior to the onset of early labor. However, the method that Esplin et al. used to identify these biomarkers involved solvent treatment to access the low-molecular-weight proteome, followed by LCMS analysis. This type of analysis, though powerful, is difficult and expensive to automate, especially for large-scale preparation of samples.[15] Other approaches such as sandwich or competitive immunoassays are similarly limited by difficulty in multiplexing, the lack of two regions for antibody recognition in the smaller peptides, or lower sensitivity and specificity for competitive immunoassay.[16] Thus,

Table 2.1. Panel of nine PTB biomarkers and their molecular masses.

PTB Biomarker	Abbreviation	Mass (kDa)
PTB Peptide 1	P1	2.0
Corticotropin releasing factor	CRF	2.7
PTB peptide 2	P2	4.2
PTB peptide 3	P3	4.2
Defensins	Def	3-6
Tumor necrosis factor-α receptor type 1	TNF	26
Lactoferrin	LF	80
Thrombin-antithrombin III	TAT	95-110
Ferritin	Fer	470

an urgent, unmet need exists for a diagnostic platform capable of PTB biomarker analysis in a clinical environment. Ideally, this platform would be inexpensive, easy to use, and robust while allowing low limits of detection (LODs) even in a complex matrix.[17]

Microfluidics are uniquely situated to fill the needs posed for PTB biomarker analysis; indeed, integrated microfluidics allow many laboratory-based techniques and processes to be miniaturized onto a single platform.[17-22] Additionally, integrated microfluidics require less sample and reagent volumes than most benchtop methods, limit sample loss, and allow for automation of complete analyses. The field of integrated microfluidic biomarker analysis has been growing rapidly. Just in recent years, new microfluidic platforms for biomarker analysis have emerged with capabilities for colorimetric or electrochemical assays,[23-24] ELISA,[25] and other biosensors.[26-27] However, a common disadvantage of most of these studies is that they were only capable of analyzing a single analyte per device. Tang et al.'s work[24] was an exception where four cancer biomarkers were measured, but this analysis required off-chip sample preparation and an array of sensors to achieve multiplexing.

In an effort to create an integrated microfluidic PTB biomarker analysis system capable of multiplexing, the Woolley lab has previously demonstrated SPE enrichment of select PTB biomarkers and integration of this system with microchip electrophoresis (μCE) for subsequent separation.[28-30] Additionally, the ability to capture and purify PTB biomarkers from blood serum using immunoaffinity extraction coupled with μCE for subsequent separation has been demonstrated.[31] In each of these cases, studies were only performed with one or two biomarkers. For greater sensitivity and specificity in PTB risk analysis to be realized, more biomarkers need to be separated and analyzed.

Here, I describe the development of a μCE method capable of separating six of the nine PTB biomarkers in this panel. I found that the resolution between the biomarker peaks could be influenced by the running buffer concentration and voltage. Additionally, LODs were determined for each of the PTB biomarkers in the μCE separation. After future integration with sample preparation steps, this μCE method should play a critical role in an integrated microfluidic PTB risk diagnostic test and allow for multiplexed identification and quantification of PTB biomarkers.

2.2 Materials and methods

2.2.1 Reagents and materials

The following chemicals were ordered from Sigma (St. Louis, MO): 2-(cyclohexylamino)ethanesulfonic acid (CHES), hydroxypropyl cellulose (HPC; 106 Da), poly(ethylene glycol) diacrylate (PEGDA; 575 Da), inhibitor remover beads, dimethyl sulfoxide (DMSO), and benzoin methyl ether (BME). Fluorescein 5-isothiocyanate (FITC) was purchased from Life Technologies (Carlsbad, CA). PTB biomarkers were obtained from the following sources: ferritin (Fer) from EMD Millipore (Billerica, MA), lactoferrin (LF) from Sigma (St. Louis, MO), PTB peptide 1 (P1) and PTB peptide 2 (P2) from Biomatik (Wilmington, DE), corticotropin releasing factor (CRF) and FITC-labeled P1 from GenScript (Piscataway, NJ), and tumor necrosis factor-α receptor type 1 (TNF) from ProSpec (East Brunswick, NJ). All solutions were made with deionized water (18.3 MΩ•cm) from a Barnstead EASY-pure UV/UF system (Dubuque, IA). Methanol was purchased from Macron (Center Valley, PA), sodium hydroxide from Mallinckrodt Baker (Paris, KY), and sodium bicarbonate from Merck (Darmstadt,

Germany). 4-(2-hydroxyethyl)-1-piperazineethanesulfonic acid (HEPES), cyclohexane, and Amicon ultra 0.5 mL centrifugal (3, 10, 30, and 50 kDa cutoff) filters were purchased from EMD Millipore. Zeonor 1060R cyclic olefin copolymer (COC) was purchased in 1 and 2 mm thick sheets (Zeon Chemicals; Louisville, KY) cut to 2.2×5 cm^2 pieces with an industrial bandsaw. Silicon wafers were from Fairchild (Phoenix, AZ) and S1805 photoresist came from MicroChem (Westborough, MA).

2.2.2 Device fabrication

Fabrication of "T-shaped" microchips in COC was performed using methods described previously. Briefly, silicon wafers were patterned and etched using standard photolithography and etching techniques.[32] The pattern was transferred into a 1 mm thick piece of COC, which was subsequently bonded to a 2 mm thick piece of COC with corresponding reservoir holes made with a drill press (Cameron; Sonora, CA).[31,33] Finally, cyclohexane was applied to the device edges to enhance bonding. Channel dimensions were approximately 20 µm tall × 50 µm wide. A device photograph is given in Figure 2.1.

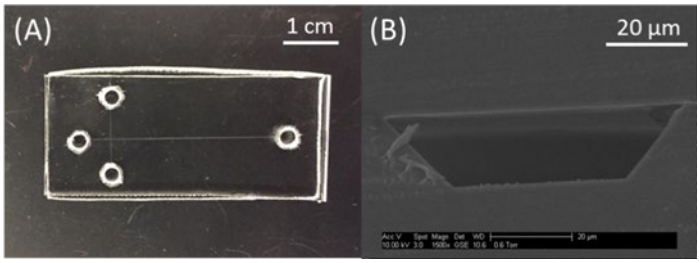

Figure 2.1. Microfluidic device used for PTB biomarker separations. (A) Device photograph. (B) SEM of channel cross-section.

Prior to µCE experiments, COC device channels were coated using a photografting method adapted from one used previously.[29] PEGDA was filtered through inhibitor remover

beads to remove the methyl ether hydroquinone polymerization inhibitor. A solution of 4% PEGDA and 1% BME was made in a 50:50 v/v mixture of water and methanol. The channels and reservoirs were filled with this solution, and the device was exposed to UV light (Uvitron; West Springfield, MA) for 12 min then flushed twice with water to remove excess photografting solution.

2.2.3 PTB biomarker preparation

To fluorescently label the PTB biomarkers, P1, P2, and CRF were dissolved in 10 mM bicarbonate buffer (BCB, pH 10). FITC was dissolved at a concentration of 10 mM in DMSO and added to the individual biomarker solutions such that the dye-to-biomarker molar ratio was 3:2, and these solutions were incubated overnight in the dark at 37°C. The other three biomarkers (LF, TNF, and Fer) were labeled under similar conditions except they were incubated at room temperature and with dye-to-biomarker molar ratios of 15:1, 20:1, and 30:1, respectively. All biomarkers except P1 were then filtered in the Amicon cutoff filter most closely correlated to the biomarker's size. Each was filtered four times for 15 min at 14000 RPM to remove excess dye. The dye-to-biomarker ratios were chosen based on visual inspection of the filtrate during filtration; if most of the excess dye was not removed by the fourth iteration, the labeling dye-to-biomarker ratio was reduced. Although this was a simple method for determining an adequate dye-to-biomarker labeling ratio, the visual inspection results were well correlated with μCE data. Finally, the biomarkers were diluted in 1 mM BCB (pH 9) prior to μCE.

2.2.4 Instrumentation

The LIF detection system (Figure 2.2) had a 488 nm laser (CrystaLaser; Reno, NV) aimed into a Zeiss Axio Observer.A1 inverted microscope (Jena, Germany) fitted with a Chroma ET-488 nm laser bandpass set (Rockingham, VT). Laser power exiting the 20× microscope objective was 4.8 mW. The microscope was fitted with a Hamamatsu PMT (Bridgewater, NJ) with a Stanford Research Systems SR-560 preamplifier (Sunnyvale, CA). Analog PMT voltage signal was converted to digital using a NI USB-6212 analog-to-digital converter (National Instruments; Austin, TX) and recorded at 20 Hz using LabVIEW software (National Instruments). μCE voltages were controlled using two high voltage power supplies (Stanford Research Systems) and a custom designed voltage switching box. Platinum electrodes ran from this box to the microchip reservoirs to apply the injection and separation voltages. Microchips were operated using pinched sample loading[34] with a 60 s injection time as described previously.[35] Separation fluorescence signal was measured 2 cm down the channel from the intersection. All separations were performed at room temperature.[36-37]

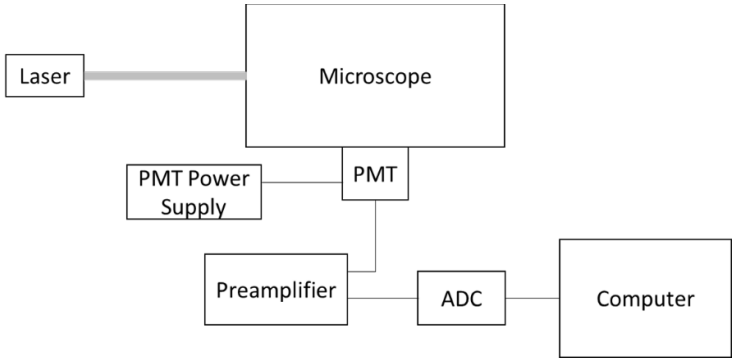

Figure 2.2. Schematic of LIF detection instrumentation involving a laser directed into a microscope fitted with a laser bandpass filter set, with filter wavelengths corresponding to the laser and fluorescence wavelengths. Fluorescent light exits the microscope and passes through a pinhole into the PMT creating an analog signal, which is first amplified and then converted to digital in the analog-to-digital converter (ADC). This digital signal is then recorded using LabVIEW software on the computer.

2.3 Results and Discussion

A critical component in developing a biomarker panel analysis for PTB risk is separation and quantification of these analytes. Factors that typically affect an electrophoretic separation include pH, buffer composition, surface properties, and analyte mobility. Each of these was investigated to develop a separation of this PTB biomarker panel.

Initial μCE experiments had inconsistent EOF between different COC devices. Specifically, sample continued to bleed into the separation channel from the injection arms, rather than being pulled back into the reservoirs once the separation voltage was applied. This flow was contrary to the expected direction of migration and was also observed by Sonker et al.,[29] who photografted the COC surface with PEGDA to yield more reproducible EOF. I used a similar photografting method to that of Sonker et al. with two minor differences. First, the use of a water-methanol solvent in the photografting mixture yielded more reliable results than using just methanol as the solvent. Second, I used a 4% PEGDA solution; 3% PEGDA was not sufficient to eliminate the undesired migration of analyte while 5% PEGDA tended to block the channels and prevent fluid flow. While these COC devices are compatible with standard 2D micromachining, I note that it is also feasible to 3D print microfluidic devices from PEGDA.[38-40] These 3D printed devices may be appealing for future analyses to avoid this photografting step.

Figure 2.3 shows a comparison of μCE in photografted and untreated devices. Electropherograms from photografted devices yielded a reproducible, symmetrical peak for Fer, while untreated devices yielded inconsistent results and had a rising baseline. Results from photografted devices were also comparable to electropherograms measured on a conventional CE system (Figure 2.4), showing the viability of these μCE devices for accurate and reproducible analyses.

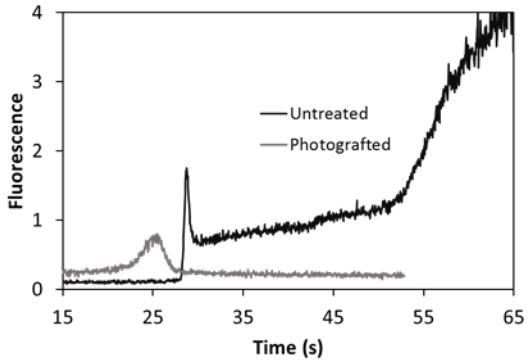

Figure 2.3. μCE of FITC-Fer (100 nM) in untreated and photografted COC devices. Buffer is 50 mM CHES (pH 9); separation at 500 V/cm.

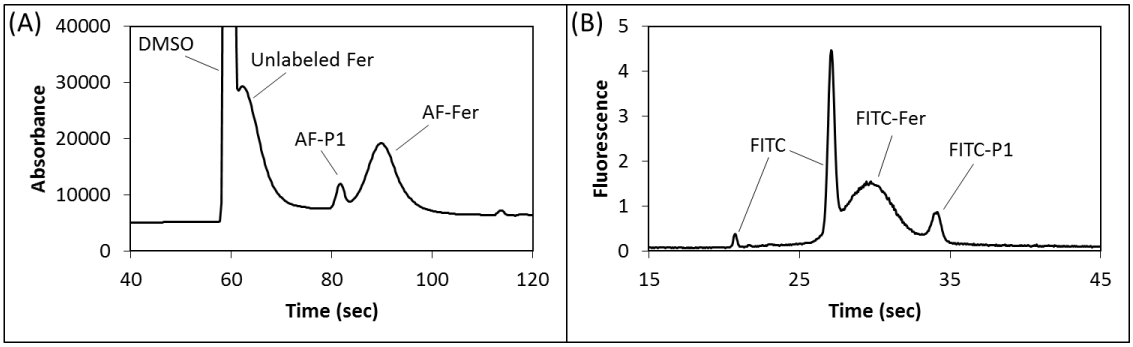

Figure 2.4. Comparison of CE and μCE separations. (A) Alexa Fluor 488 TFP-ester (AF; Thermo Fisher) labeled P1 (100 μM) and Fer (20 μM) separated in 25 mM phosphate buffer (pH 8) on a Beckman Coulter P/ACE MDQ (Brea, CA) at -1000 V/cm in a fused silica capillary (50 μm internal diameter, detection at 20 cm). Detection wavelength was 200 nm. (B) FITC labeled P1 (100 nM) and Fer (210 nM) separated in 25 mM HEPES buffer (pH 8) in a photografted COC microchip at 350 V/cm. The CE migration order is inverted from μCE due to the silica capillary EOF. The difference in detection concentrations is due to UV absorbance (CE) compared to fluorescence (μCE) detection systems. This difference in detection systems is also why peaks for DMSO and unlabeled Fer can be seen in conventional CE.

For optimization experiments, I used only a representative portion of the PTB biomarkers in the separations. This simplified the electropherograms for both visualization and quantification of results. Fer was chosen because, at 470 kDa, it is the largest biomarker. Likewise, P1 was used in many of these experiments because it is the smallest biomarker (2.0 kDa). LF was chosen both for its large size (80 kDa) and high pI value; initial experiments found

that biomarkers like LF and P2 with high pI values were more adsorptive to the microchannel surfaces and difficult to fluorescently label than biomarkers with lower pI values.

To test the dependence of separation efficiency on pH, two of the biomarkers, Fer and LF, were fluorescently labeled and separated in photografted COC devices at four different pHs from 7 to 10 (Figure 2.5). Because FITC fluorescence intensity is pH dependent (Figure 2.6), this range was chosen to encompass most of its fluorescent range. The results from these separations indicate that photografting largely suppressed EOF, resulting in the running buffer pH having little effect on separation efficiency. The most significant effect of running buffer pH was on the resolution of the dye peaks at the beginning of the run. Notably, the resolution of these dye peaks was greatest for the pH 8 and 10 runs. Likely, this difference is due to the higher ionic strength of these buffers compared to those at pH 7 and 9, which originates from titrating the buffer with greater amounts of NaOH to reach the desired pH. Differences in ionic strength were confirmed by monitoring the electrical current through the microchip channels during each separation, which revealed higher current for the pH 8 and 10 separations than the other two.

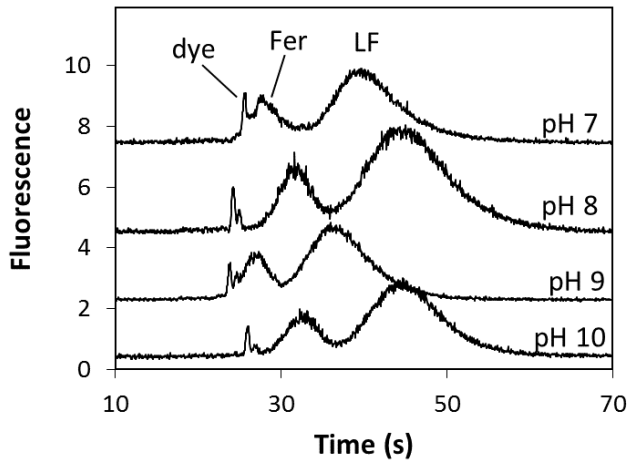

Figure 2.5. μCE of FITC-labeled Fer (10 nM) and LF (60 nM) at 500 V/cm with different running buffers: pH 7, 100 mM HEPES; pH 8, 100 mM HEPES; pH 9, 100 mM CHES; pH 10, 100 mM CHES. Signals are offset for clarity.

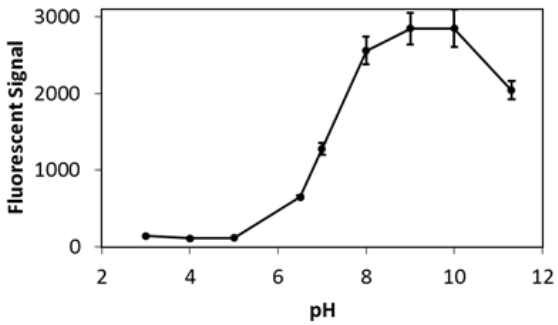

Figure 2.6. Fluorescence of 1 μM FITC as a function of pH in 25 mM acetate (pH 3-6), phosphate (pH 6-8), and bicarbonate (pH 8-11) buffers. Signal was measured on a Nanodrop 3300 Fluorospectrometer (Thermo Fisher; Waltham, MA).

The results from Figure 2.5 suggested that PTB biomarker separations were affected by ionic strength more than the pH of the running buffer between pH 7–10. To confirm this, separations of three biomarkers (Fer, P1, and LF) were performed with different running buffer concentrations (Figure 2.7). It was found that increasing the buffer concentration improved resolution for P1 and LF while diminishing the resolution for Fer and P1. It was also found that the resolution approached a maximum or minimum value as the buffer concentration continued to increase. This meant that the P1-LF resolution could be improved to a certain point without completely deteriorating the Fer-P1 resolution. However, using higher running buffer concentrations also increased the electrical current in the microchannels, which could lead to

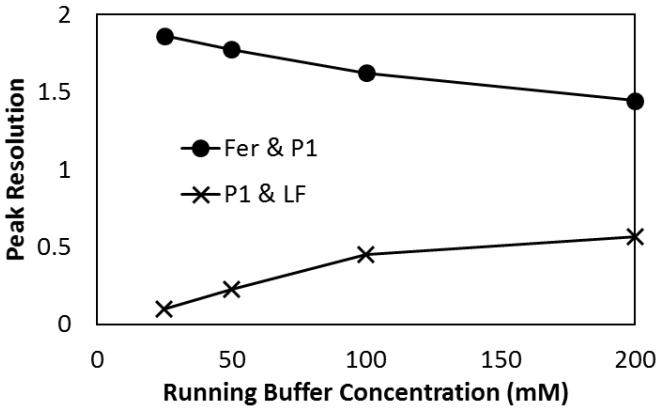

Figure 2.7. Resolution of Fer, P1, and LF with changing running buffer concentration. Separations were performed in HEPES buffer (pH 8) at 500 V/cm.

Joule heating and other deleterious effects. To balance improved P1-LF resolution with reasonable electrical current, a running buffer concentration of 100 mM was used for later experiments. While a resolution of 0.5 for P1-LF is enough to distinguish these peaks, it may not be sufficient to precisely quantitate these two biomarkers.

Another factor known to affect electrophoretic separation resolution and Joule heating is the applied voltage.[41-42] Separations were performed with the same three PTB biomarkers (Fer, P1, and LF) and 100 mM HEPES buffer having 0.5% HPC (pH 8) using different applied voltages. Figure 2.8A shows that increasing the applied voltage did not significantly affect the P1-LF resolution but did decrease the Fer-P1 resolution. As can be seen, if the applied voltage was doubled, the Fer-P1 resolution decreased by about a factor of two. The added HPC in the buffer increased viscosity and narrowed the biomarker peaks by reducing any residual biomarker-microchannel surface interactions that persisted after photografting. This improved the P1-LF resolution but resulted in closer Fer-P1 migration times, which degraded the Fer-P1 resolution.

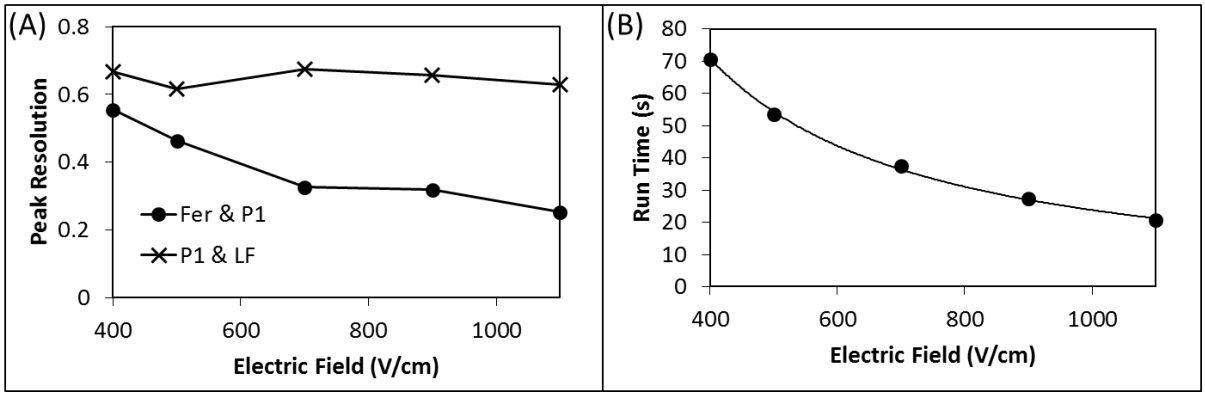

Figure 2.8. Effect of electric field on PTB biomarker separations. (A) Resolution of Fer and P1, and P1 and LF as a function of electric field. (B) Separation run time as a function of electric field. Separations were performed in 100 mM HEPES (pH 8) with 0.05% HPC.

Besides affecting peak resolution, increasing the applied electric field decreased the migration times of all analytes, as expected (Figure 2.8B). Higher electric field allows for a PTB analysis to be performed more quickly and limits the time in which diffusional band broadening can occur. To balance these benefits with the decreasing Fer-P1 resolution, 500 V/cm was applied to the microchannels in future separations. This allowed separation of the PTB biomarkers in one minute while maintaining satisfactory resolution between the biomarker peaks.

The conditions selected for the separation of the PTB biomarker panel were a photografted COC microchip run at 500 V/cm with a 100 mM running buffer of any pH between 7 and 10 at room temperature. Using these conditions, it was possible to separate six of the PTB biomarkers (Figure 2.9): Fer, P1, LF, P2, CRF, and TNF. This separation is significant because it is the first μCE separation of most of the components of this biomarker panel. It is also significant because of the large mass range of analytes in the panel—from 2 to 470 kDa. Finally,

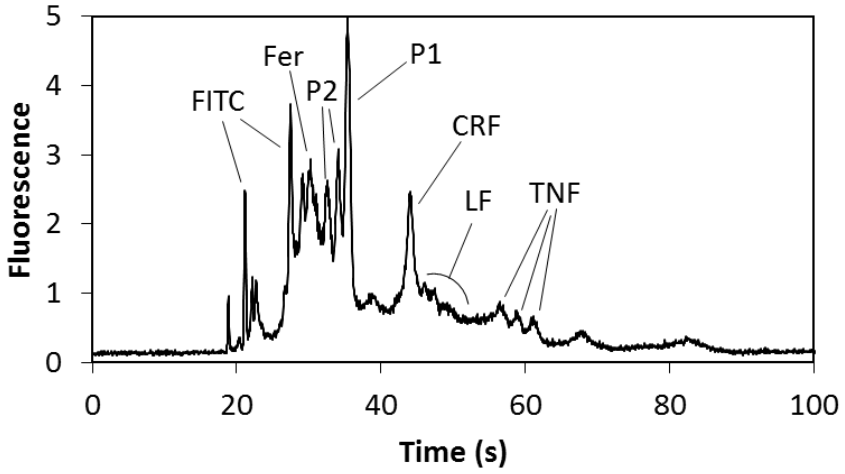

Figure 2.9. μCE of six PTB biomarkers labeled with FITC: Fer, 60 nM; P2, 130 nM; P1, 10 nM; CRF, 60 nM; LF, 60 nM; TNF, 140 nM. Running buffer was 100 mM CHES (pH 9) with 0.05% HPC; separation at 500 V/cm.

most protein μCE separations contain three or fewer (often model) analytes;[42] this separation contains three peptides in addition to three proteins that are implicated in PTB.

Several additional points arise from the electropherogram in Figure 2.9. First, P2 produced two peaks, which is attributed to an N-terminal asparagine (Table 2.2) that degrades in water to aspartic acid. Although it is possible to synthetically block the N-terminus to prevent this degradation, it was left uncapped to more closely simulate a clinical sample. Moreover, the larger protein biomarkers had broader peaks than the smaller peptide biomarkers in the electropherogram. This is likely due to the greater number of fluorescent labeling sites available, resulting in a broader distribution of charges on these proteins. The LF peak in particular is broad both because of this charge distribution and its high pI value, which makes it more prone to microchip surface adsorption than the other biomarkers. Finally, peak overlap occurs in some regions of the separation, which could hinder quantitation especially for real samples. Importantly, upstream sample preparation steps prior to μCE can be integrated on-chip for analyzing real samples. Indeed, CE data of serum samples after on-chip immunoaffinity extraction were comparable to results obtained from the same biomarkers in buffer.[31] Moreover, upstream immunoaffinity extraction can be used to split a biomarker panel to have any interfering biomarkers (i.e., CRF and LF) divided into separate μCE runs for easier quantitation.

Table 2.2. Amino acid sequences for three PTB peptide biomarkers.

PTB Peptide Biomarker	Amino Acid Sequence
P1	qlglpgppdvpdhaayhpf
P2	nvhsagaasrmnfrpgvlssrqlglpgppdvpdhaayhpf
P3	nvhsagaasrm(O)nfrpgvlssrqlglpgppdvpdhaayhpf

Of the nine PTB biomarkers in the panel,[14] three were omitted from the final separation: PTB peptide 3 (P3), defensins (Def), and thrombin-antithrombin III (TAT). P3 was excluded

because its amino acid sequence is nearly identical to that of P2; the only difference is where P2 contains a methionine, P3 contains an oxidized methionine (Table 2.2). As this oxidation contributes neither a significant charge nor mass difference to the peptide, P2 and P3 have indistinguishable electrophoretic mobilities, and only one was included in the biomarker separation. Def was excluded because it represents several different peptides;[9] its electropherogram had multiple peaks that interfered with the signal from other PTB biomarkers. Members of the Woolley lab are working to identify which specific Def peptide has the best diagnostic potential so it can be added to the biomarker separation. Finally, TAT was not included in this separation because it is not available commercially, and it is difficult to form the TAT complex under conditions where fluorescent labeling is also feasible. As appropriate conditions are developed, this biomarker could be added to the separation.

It is important to know how the LOD of each PTB biomarker compares with PTB risk levels. Peak height calibration curves were established for each biomarker on three different microchips (Figure 2.10). An LOD, the concentration at which the measured signal was three

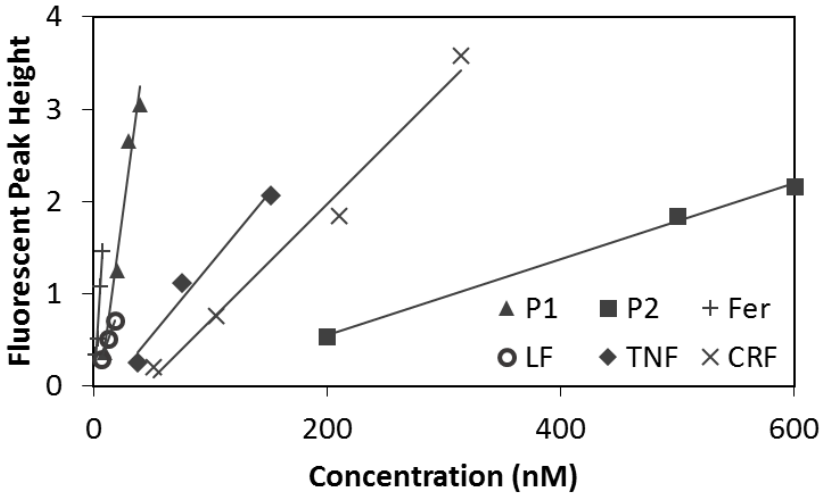

Figure 2.10. Calibration curves for LOD determination for six PTB biomarkers. Data from the devices that yielded the lowest LOD for each biomarker are shown.

times the standard deviation of the baseline noise, was calculated for each of these calibration curves. As seen in Table 2.3, the LOD for each of the biomarkers is in the nanomolar range. Except for P1, the trend is for the larger mass biomarkers to have a lower molar LOD. Likely, this is because larger biomarkers such as Fer and LF have more primary amines for reaction with FITC, resulting in multiple labels being incorporated per protein. In contrast, smaller biomarkers such as P2 and CRF, which contain a single primary amine labeling site (the N-terminus), can only incorporate one label.[30] In addition, the LOD for P2 is significantly higher than that of the other PTB biomarkers because its tertiary structure creates steric hindrance around the N-terminus, which reduces the FITC-labeling efficiency.[44] Although the efficiency was improved by heating the biomarker solution during labeling, P2 still has a higher LOD than the other biomarkers.

Table 2.3. Migration time, calibration curve linear regression (R^2), and the mean LOD (all determined from three different devices) for six PTB biomarkers. PTB risk levels where known are also given for reference. Running buffer was 100 mM HEPES (pH 8) with 0.05% HPC.

PTB Biomarker	Migration Time (s)	Calibration R^2	LOD (nM)	PTB Risk Level (nM)
P1	36.7±2.0	0.97	3	*
P2	34.7±1.6	0.99	190	*
CRF	44.4±4.3	0.92	90	0.075
TNF	61.5±3.6	0.99	30	0.06
LF	47.8±3.1	0.97	6	3
Fer	31.4±1.3	0.96	1	0.040

Table 2.3 also lists the biomarker concentrations in maternal blood serum[14] that are indicative of PTB risk. The LODs are approaching PTB risk levels for some biomarkers, but they are not as low as will be necessary for PTB risk analysis. Importantly, by using on-chip sample preparation steps prior to separation of the biomarkers, detection of these PTB biomarkers below

their risk levels should be possible. Using immunoaffinity extraction from blood serum[31] and solid phase extraction[28-30] as described previously, six-fold and 50-fold preconcentrations, respectively, should be achievable for a combined 300-fold enrichment of the biomarkers. These enrichment factors should lower the biomarker LODs to near or below the risk level concentrations. I also expect further improvement of preconcentration capabilities as these components are integrated into a single device.

There is an urgent need for a fast and inexpensive PTB risk diagnostic. This need could be met by developing a microfluidic device that integrates sample preparation with separation and detection of PTB risk biomarkers. Here, I have focused on the separation and detection of a panel of PTB biomarkers. I studied the dependence of peak resolution on the running buffer concentration and electric field. The dependence required a balance of parameters to be considered to improve the poorest resolution between peaks without significantly deteriorating others. Furthermore, I demonstrated a μCE separation for six combined protein and peptide biomarkers: the first performed on this PTB biomarker panel. Additional experiments should make it possible to add other biomarkers to this separation. Some of the PTB biomarker LODs are approaching PTB risk levels, but lower detection limits are still needed. It may be possible to achieve this using CE-LIF or CE-MS, but these methods would require larger sample volumes and external sample preparation prior to analysis. Using the current approach, lower biomarker LODs could be achieved via integration of this μCE separation with upstream sample preparation steps that extract, purify, and enrich biomarkers[28-31] from maternal blood serum samples. Additionally, biomarker LODs could be lowered by implementing sample stacking prior to μCE,[45-46] improving the labeling efficiency,[44,47] or use of a brighter fluorescent label

such as Alexa Fluor.[48-49] Once developed, such an integrated device has broad potential to be applied to many other clinical biomarker analyses.

2.4 References

1. Centers for Disease Control and Prevention. Reproductive health: preterm birth. https://www.cdc.gov/reproductivehealth/maternalinfanthealth/pretermbirth.htm (accessed January 23, 2020).

2. World Health Organization. *Born too soon: the global action report on preterm birth*. WHO, Geneva, 2012.

3. Simon, L.; Nusinovici, S.; Flamant, C.; Cariou, B.; Rouger, V.; Gascoin, G.; Darmaun, D.; Rozé, J.-L.; Hanf, M. Post-term growth and cognitive development at 5 years of age in preterm children: evidence from a prospective population-based cohort. *PLOS ONE* **2017,** *12,* e0174645.

4. Institute of Medicine of the National Academies. *Preterm Birth: Causes, Consequences, and Prevention.* IOM, Washington, DC, 2006.

5. Roberts, D.; Brown, J.; Medley, N.; Dalziel, S. R. Antenatal corticosteroids for accelerating fetal lung maturation for women at risk of preterm birth (review). *Cochrane Data. Sys. Rev.* **2017,** CD004454.

6. Wigle, D. T.; Arbuckle, T. E.; Turner, M. C.; Bérubé, A.; Yang, Q.; Liu, S.; Krewski, D. Epidemiologic evidence of relationships between reproductive and child health outcomes and environmental chemical contaminants. *J. Tox. Envir. Health. B* **2008,** *11,* 373–517.

7. Kramer, M. S.; Lydon, J.; Séguin, L.; Goulet, L.; Kahn, S. R.; McNamara, H.; Genest, J.; Dassa, C.; Chen, M. F.; Sharma, S.; Meaney, M. J.; Thomson, S.; Uum, S. V.; Koren, G.; Dahhou, M.; Lamoureux, J.; Platt, R. W. Stress pathsways to spontaneous preterm birth: the role

of stressors, psychological distress, and stress hormones. *Am. J. Epidemiol.* **2009,** *169,* 1319–1326.

8. Goldenberg, R. L.; Rouse, D. J. Prevention of premature birth. *N. Engl. J. Med.* **1998,** *339,* 313–320.

9. Goldenberg, R. L.; Iams, J. D.; Mercer, B. M.; Meis, P. J.; Moawad, A.; Das, A.; Miodovnik, M.; VanDorsten, P. J.; Caritis, S. N.; Thurnau, G.; Dombrowski, M. P. The preterm predictions study: toward a multiple-marker test for spontaneous preterm birth. *Am. J. Obstet. Gynecol.* **2001,** *185,* 643–651.

10. Al-Gubory, K. H.; Fowler, P. A.; Garrel, C. The roles of cellular reactive oxygen species, oxidative stress and antioxidants in pregnancy outcomes. *Int. J. Biochem. Cell Biol.* **2010,** *42,* 1634–1650.

11. Buhimschi, I. A.; Christner, R.; Buhimschi, C. S. Proteomic biomarker analysis of amniotic fluid for identification of intraamniotic inflammation. *BJOG* **2005,** *112,* 173–181.

12. Fortunato, S. J.; Menon, R. Distinct molecular events suggest different pathways for preterm labor and premature rupture of membranes. *Am. J. Obstet. Gynecol.* **2001,** *184,* 1399–1406.

13. Petraglia, F.; Imperatore, A.; Challis, J. R. G. Neuroendocrine mechanisms in pregnancy and parturition. *Endocrine Rev.* **2010,** *31,* 783–816.

14. Esplin, M. S.; Merrell, K.; Goldenberg, R.; Lai, Y.; Iams, J. D.; Mercer, B.; Spong, C. Y.; Miodovnik, M.; Simhan, H. N.; van Dorsten, P.; Dombrowski, M. Proteomic identification of serum peptides predicting subsequent spontaneous preterm birth. *Am. J. Obstet. Gynecol.* **2011,** *204,* 391.e1–8.

15. Grebe, S. K. G.; Singh, R. J. LC-MS/MS in the clinical laboratory—where to from here? *Clin. Biochem. Rev.* **2011,** *32,* 5–31.

16. Cross, T. G.; Hornshaw, M. P. Can LC and LC-MS ever replace immunoassays? *J. Appl. Bioanal.* **2016,** *2,* 108–116.

17. Yager, P.; Edwards, T.; Fu, E.; Helton, K.; Nelson, K.; Tam, M. R.; Weigl, B. H. Microfluidic diagnostic technologies for global public health. *Nature* **2006,** *442,* 412–418.

18. Nge, P. N.; Rogers, C. I.; Woolley, A. T. Advances in microfluidic materials, functions, integration, and applications. *Chem. Rev.* **2013,** *113,* 2550–2583.

19. Mark, D.; Haeberle, S.; Roth, G.; von Stetten, F.; Zengerle, R. Microfluidic lab-on-a-chip platforms: requirements, characteristics and applications. *Chem. Soc. Rev.* **2010,** *39,* 1153–1182.

20. Ohno, K.-i.; Tachikawa, K.; Manz, A. Microfluidics: applications for analytical purposes in chemistry and biochemistry. *Electrophoresis* **2008,** *29,* 4443–4453.

21. Pandey, C. M.; Augustine, S.; Kumar, S.; Kumar, S.; Nara, S.; Srivastava, S.; Malhotra, B. D. Microfluidics based point-of-care diagnostics. *Biotechnol. J.* **2018,** *13,* 1700047.

22. Sonker, M.; Sahore, V.; Woolley, A. T. Recent advances in microfluidic sample preparation and separation techniques for molecular biomarker analysis: a critical review. *Anal. Chim. Acta* **2017,** *986,* 1–11.

23. Garg, N.; Vallejo, D.; Boyle, D.; Nanayakkara, I.; Teng, A.; Pablo, J.; Liang, X.; Camerini, D.; Lee, A. P.; Felgner, P. Integrated on-chip microfluidic immunoassay for rapid biomarker detection. *Procedia Eng.* **2016,** *159,* 53–57.

24. Tang, C. K.; Vaze, A.; Shen, M.; Rusling, J. F. High-throughput electrochemical microfluidic immunoarray for multiplexed detection of cancer biomarker proteins. *ACS Sens.* **2016,** *1,* 1036–1043.

25. Liu, D.; Li, X.; Zhou, J.; Liu, S.; Tian, T.; Song, Y.; Zhu, Z.; Zhou, L.; Ji, T.; Yang, C. A fully integrated distance readout ELISA-Chip for point-of-care testing with sample-in answer-out capability. *Biosens. Bioelectron.* **2017,** *96,* 332–338.

26. Ali, M. A.; Mondal, K.; Jiao, Y.; Oren, S.; Xu, Z.; Sharma, A.; Dong, L. Microfluidic immune-biochip for detection of breast cancer biomarkers using hierarchical composite of porous graphene and titanium dioxide nanofibers. *ACS Appl. Mater. Interfaces* **2016,** *8,* 20570–20582.

27. Uludag, Y.; Narter, F.; Sağlam, E.; Köktürk, G.; Gök, M. Y.; Akgün, M.; Barut, S.; Budak, S. An integrated lab-on-a-chip-based electrochemical biosensor for rapid and sensitive detection of cancer biomarkers. *Anal. Bioanal. Chem.* **2016,** *408,* 7775–7783.

28. Kumar, S.; Sahore, V.; Rogers, C. I.; Woolley, A. T. Development of an integrated microfluidic solid-phase extraction and electrophoresis device. *Analyst* **2016,** *141,* 1660–1668.

29. Sonker, M.; Knob, R.; Sahore, V.; Woolley, A. T. Integrated electrokinetically driven microfluidic devices with pH-mediated solid-phase extraction coupled to microchip electrophoresis for preterm birth biomarkers. *Electrophoresis* **2017,** *38,* 1743–1754.

30. Sahore, V.; Sonker, M.; Nielsen, A. V.; Knob, R.; Kumar, S.; Woolley, A. T. Automated microfluidic devices integrating solid-phase extraction, fluorescent labeling, and microchip electrophoresis for preterm birth biomarker analysis. *Anal. Bioanal. Chem* **2018,** *410,* 933–941.

31. Sonker, M.; Parker, E. K.; Nielsen, A. V.; Sahore, V.; Woolley, A. T. Electrokinetically operated microfluidic devices for integrated immunoaffinity monolith extraction and electrophoretic separation of preterm birth biomarkers. *Analyst* **2018,** *143,* 224–231.

32. Kelly, R. T.; Woolley, A. T. Thermal bonding of polymeric capillary electrophoresis microdevices in water. *Anal. Chem.* **2003,** *75,* 1941–1945.

33. Nge, P. N.; Pagaduan, J. V.; Yu, M.; Woolley, A. T. Microfluidic chips with reversed-phase monoliths for solid phase extraction and on-chip labeling. *J. Chromatogr. A* **2012,** *1261,* 129–135.

34. Jacobson, S. C.; Hergenröder, R.; Koutny, L. B.; Warmack, R. J.; Ramsey, J. M. Effects of injection schemes and column geometry on the performance of microchip electrophoresis devices. *Anal. Chem.* **1994,** *66,* 1107–1113.

35. Sonker, M.; Yang, R.; Sahore, V.; Kumar, S.; Woolley, A.T. On-chip fluorescent labeling using reversed-phase monoliths and microchip electrophoretic separations of selected preterm birth biomarkers. *Anal. Meth.* **2016,** *8,* 7739–7746.

36. Guttman, A.; Kerekgyarto, M.; Jarvas, G. Effect of separation temperature of structure specific glycan migration in capillary electrophoresis. *Anal. Chem.* **2015,** *87,* 11630–11634.

37. Szigeti, M.; Guttman, A. High-resolution glycan analysis by temperature gradient capillary electrophoresis. *Anal. Chem.* **2017,** *89,* 2201–2204.

38. Beauchamp, M. J.; Nordin, G. P.; Woolley, A. T. Moving from millifluidic to truly microfluidic sub-100-μm cross-section 3D printed devices. *Anal. Bioanal. Chem.* **2017,** *409,* 4311–4319.

39. Gong, H.; Bickham, B. P.; Woolley, A. T.; Nordin, G. P. Custom 3D printer and resin for 18 μm x 20 μm microfluidic flow channels. *Lab Chip* **2017,** *17,* 2899–2909.

40. Gong, H.; Woolley, A. T.; Nordin, G. P. 3D printed high density, reversible, chip-to-chip microfluidic interconnects. *Lab Chip* **2018,** *18,* 639–647.

41. Jacobson, S. C.; Hergenröder, R.; Koutny, L. B.; Ramsey, J. M. High-speed separations on a microchip. *Anal. Chem.* **1994,** *66,* 1114–1118.

42. Tang, G. Y.; Yang, C.; Chai, J. C.; Gong, H. Q. Joule heating effect on electroosmotic flow and mass species transport in a microcapillary. *Int. J. Heat. Mass. Transfer* **2004,** *47,* 215–227.

43. Dawod, M.; Arvin, N. E.; Kennedy, R. T. Recent advances in protein analysis by capillary and microchip electrophoresis. *Analyst* **2017,** *142,* 1847–1866.

44. Kumar, S. Design, Fabrication, and Optimization of Miniaturized Devices for Bioanalytical Applications. Ph.D. Dissertation, Brigham Young University, Provo, UT, 2015, pp. 84–102.

45. Breadmore, M. C. Recent advances in enhancing the sensitivity of electrophoresis and electrochromatography in capillaries and microchips. *Electrophoresis* **2007,** *28,* 254–281.

46. Shihabi, Z. K. Stacking in capillary zone electrophoresis. *J. Chromatogr. A* **2000,** *902,* 107–117.

47. Goding, J. W. Conjugation of antibodies with fluorochromes: modifications to the standard methods. *J. Immunol. Meth.* **1976,** *13,* 215–226.

48. Panchuk-Voloshina, N.; Haugland, R. P.; Bishop-Stewart, J.; Bhalgat, M. K.; Millard, P. J.; Mao, F.; Leung, W.-Y.; Haugland, R. P. Alexa dyes, a series of new fluorescent dyes that yield exceptionally bright, photostable conjugates. *J. Histochem. Cytochem.* **1999,** *47,* 1179–1188.

49. Mahmoudian, J.; Hadavi, R.; Jeddi-Tehrani, M.; Mahmoudi, A. R.; Bayat, A. A.; Shaban, E.; Vafakhah, M.; Darzi, M.; Tarahomi, M.; Ghods, R. Comparison of photobleaching and photostability traits of Alexa Fluor 568- and fluorescein isothiocyanate- conjugated antibody. *Cell J.* **2011,** *13,* 169–172.

3. 3D PRINTED MICROFLUIDIC DEVICES FOR SOLID-PHASE EXTRACTION AND ON-CHIP FLUORESCENT LABELING OF PRETERM BIRTH RISK BIOMARKERS*

3.1 Introduction

Over the past 30 years, the field of microfluidics has established advantages of low sample and reagent consumption, fast analyses, and cost-effectiveness compared to many benchtop instruments and processes. These benefits are apparent in a variety of applications, including biomarker,[1] nucleic acid,[2] organ-on-a-chip,[3] single- and multi-cellular,[4-5] polymerase chain reaction,[6] and biosensor[7] analyses. Available microfabrication methods have previously limited the design capabilities of these microfluidic devices,[8] but the recent trend towards use of 3D printing has created new possibilities for researchers to miniaturize, iteratively customize, and integrate more sample preparation and analysis methods into fluidic chips.[9] Although the commercial availability of 3D printers capable of producing <100-μm channels is still limited,[10] this barrier can be breached to achieve enclosed, truly microfluidic features.[11]

For growing applications in microfluidics, there is a persistent need to detect lower analyte concentrations. Indeed, the use of small sample volumes in microchannels has a major influence on the approach needed for detection of analytes of interest.[12] Often, lowering the analyte limit of detection must begin during sample preparation by limiting losses and implementing preconcentration. Although there are many methods for preconcentration,[12] solid-

---

* This chapter is adapted from:
Bickham, A. V.; Pang, C.; George, B. Q.; Topham, D. J.; Nordin, G. P.; Woolley, A. T. 3D printed microfluidic devices for solid-phase extraction and on-chip fluorescent labeling of preterm birth risk biomarkers. *Anal. Chem.* Submitted.

phase extraction (SPE) is one of the most general ones, because it can be applied to relatively larger sample volumes.[13] Miniaturization of an SPE system allows for integration with other analysis steps and can be simple, fast, and effective. Many different SPE systems have been developed previously for microfluidic applications, including for analysis of alkaloids,[14] metal ions,[15-16] nucleic acids,[17-19] aromatic hydrocarbons,[20] and phosphopeptides.[21] These applications often utilize a variety of SPE sorbent beds such as packed beads, micro- or nanofibers, porous polymer monoliths, membranes, or other microstructures to achieve high surface areas and appropriate chemical properties for effective extraction.[17,22] Monoliths can be particularly useful because of their ease of *in situ* fabrication and morphological tuning.[23] Recent initial studies utilized monoliths in 3D printed fluidic devices for hydrogen/deuterium exchange,[24] immunoaffinity extraction,[25] liquid chromatography,[26] and SPE of alkyl esters on a gold nanoparticle modified monolith.[27] However, only for the immunoaffinity extraction were the 3D printed channels truly microfluidic, with cross sections smaller than 100 x 100 μm^2.

Each year, nearly 15 million infants are born prematurely, resulting in over 1 million deaths worldwide from either the direct effects of preterm birth (PTB) or later complications, such as respiratory difficulties or increased susceptibility to infection.[28] The World Health Organization has a number of recommended interventions to reduce mortality rates,[28] but they are mainly focused on care during labor and after delivery. In part, this is because no early clinical assessment currently exists to give warning of an imminent PTB prior to the onset of labor. Such an assessment may be possible with a panel of nine previously discovered protein and peptide biomarkers,[29] summarized in Table 3.1. Toward development of a PTB risk assessment, some of these protein and peptide biomarkers have been evaluated in microfluidic

Table 3.1 PTB biomarkers, their molecular masses, and a characterization of the hydrophobicity of their amino acid composition.

Biomarker	Mass (kDa)	Amino Acid Characterization		
		Hydrophobic	Neutral	Hydrophilic
Peptide 1	2.0	58%	21%	21%
CRF	2.7	49%	20%	32%
Peptide 2	4.2	50%	30%	20%
Peptide 3	4.2	48%	30%	23%
Defensins	3-20	41±7%	24±5%	35±6%
TNF	26	38%	38%	24%
Lactoferrin	80	39%	35%	25%
TAT	120	39%	33%	28%
Ferritin	420	37%	33%	30%

devices for immunoaffinity extraction,[25,30] electrophoretic separations,[31-32] and SPE.[33-34] However, this entire panel has not previously been evaluated in a microfluidic analysis format.

Here, I show the development of a reversed-phase monolith for SPE of PTB biomarkers. These monoliths are photopolymerized within 3D printed microfluidic device channels, allowing for easy and fast device fabrication. The SPE devices were evaluated for retention and elution of nine PTB biomarkers as well as a fluorescent label, Alexa Fluor 532 NHS ester. Finally, these 3D printed microfluidic devices were tested, using the same nine PTB biomarker analytes, for performing on-chip SPE and fluorescent labeling. Notably, these 3D printed devices and reversed-phase monoliths are well-suited for SPE retention and elution of PTB biomarkers during on-chip labeling. These results demonstrate nearly universal retention and elution performance for SPE of a diverse panel of protein and peptide biomarkers, marking an important step toward the development of a complete miniaturized PTB risk assessment.

3.2 Materials and Methods

3.2.1 Materials

The following chemicals were ordered from Sigma (St. Louis, MO): poly(ethylene glycol) diacrylate (PEGDA; MW 250 Da), phenylbis(2,4,6-trimethylenzoyl)phosphine oxide (Irgacure 819), acetonitrile (ACN), 1-dodecanol, ethylene dimethacrylate (EDMA), lauryl methacrylate (LMA), octyl methacrylate (OMA), 2,2-dimethoxy-2-phenylacetophenone (DMPA), 3-(trimethoxysilyl)propyl methacrylate, and dimethyl sulfoxide (DMSO). PTB biomarkers were purchased from the following sources: PTB peptides 1-3 (Biomatik, Wilmington, DE), corticotropin-releasing factor (CRF, GenScript, Piscataway, NJ), defensins (mixed human neutrophil peptides, Athens Research and Technology, Athens, GA), ferritin (EMD Millipore, Billerica, MA), lactoferrin (Sigma), tumor necrosis factor-α receptor type 1 (TNF, ProSpec, East Brunswick, NJ), thrombin and antithrombin (Haematologic Technology, Essex Junction, VT), and heparin (Alfa-Aesar, Haverhill, MA). Fluorescent labeling of biomarkers was performed using Alexa Fluor 532 NHS ester (Thermo Fisher, Fair Lawn, NJ) with filtering in Amicon Ultra 0.5 mL centrifugal cutoff filters (EMD Millipore). Bicarbonate buffer (BCB, pH 10) was prepared using sodium bicarbonate from Merck (Darmstadt, Germany) and sodium hydroxide from Mallinckrodt Baker (Paris, KY). 2-nitrophenyl phenyl sulfide (NPS, TCI Chemicals, Portland, OR) and glass slides (25 mm x 75 mm x 1 mm; VWR, Center Valley, PA) were purchased for 3D printing. Additional solvents of isopropyl alcohol (IPA) and toluene came from Macron. Finally, all water was purified to 18.3 MΩ·cm prior to use (Barnstead EASY-Pure UV/UF, Dubuque, IA).

3.2.2 3D Printing

Microfluidic devices are designed in the freeware computer-aided design (CAD) software, OpenSCAD (openscad.org); each print has 10-µm-thick layers and includes five identical devices. The design is adapted from one used by Parker et al.[25] A 6-pixel (46 µm) by 5-layer (50 µm) channel connects a 2.7 mm diameter x 0.75 mm deep reservoir to a 1.1 mm diameter horizontal port, into which PTFE tubing (0.022 in ID x 0.042 in OD; Cole Parmer, Vernon Hills, IL) is inserted for the application of vacuum for flow through the channel. The device also includes a 600 µm wide monolith polymerization window, placed 60 µm above the channel.[25] CAD designs of the devices can be seen in Figure 3.1A-B.

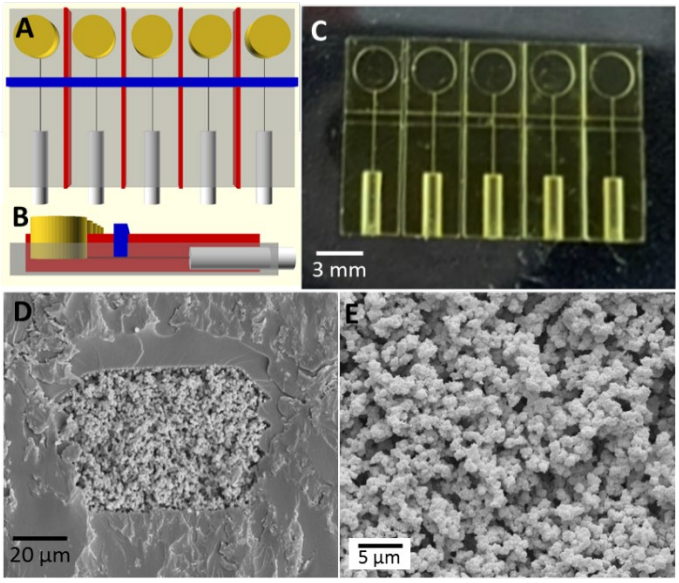

Figure 3.1. 3D printed microfluidic devices with monoliths for SPE and on-chip labeling experiments. (A-B) Top- and side-views of the CAD design of 3D printed devices, which have five identical channels (light blue) with reservoirs (yellow) and vacuum-attachment ports (gray). A polymerization window (blue) also runs perpendicular through the device, 60 µm above the channels. (C) Photograph of a 3D printed device. (D-E) SEM images of an LMA monolith polymerized within a 70 x 50 μm^2 channel, demonstrating wall adhesion and porosity.

Microfluidic devices were formed in a custom 3D printer with a 385 nm light source. The development of this printer and corresponding custom resin, consisting of 2% NPS and 1%

Irgacure 819 in PEGDA, have been described previously.[11] The exposure time for each layer in the bulk material was 600 ms with 200 ms less exposure in the 3 pixels (~22 μm) to the side of and 3 layers (~30 μm) above the channel region to widen the channels (70 μm x 50 μm) beyond the designed size, as detailed previously by Beauchamp et al.[35] All 3D prints were exposed with a measured optical irradiance of 21 $mW \cdot cm^{-2}$ in the image plane.

3.2.3 Monolith Preparation

Similar to previously described procedures,[33-34,36] reversed-phase monolithic columns were prepared using 1% DMPA photoinitiator in a mixture of monomer (LMA or OMA), crosslinker (EDMA), and porogens (1-dodecanol and/or cyclohexanol). Initially, these mixtures were polymerized in microcentrifuge tubes for 10 min under a UV lamp (Uvitron, West Springfield, MA) to analyze the degree of photopolymerization in each mixture. Analysis was performed by visual inspection. Once a suitable range of component compositions was identified using this approach, mixtures were polymerized in 3D printed device channels, sectioned with a razor blade and imaged using SEM[25] (Helios Nanolab 600 FEI, Fisher), and, in some cases, experimentally tested by performing SPE of a PTB biomarker. Each monolith formulation was analyzed for flow when vacuum was applied; morphology of nodules and pores; and PTB biomarker extraction, retention, and elution. These criteria allowed for a well-suited mixture to be decided upon and used for SPE and on-chip labeling of all nine PTB biomarkers.

After polymerization of monoliths within the 3D printed device channels, PTFE tubing was inserted into the horizontal port for each channel and affixed with hot glue, then IPA was drawn by vacuum through each channel for a minimum of 30 min. Cleaning was complete when a channel and monolith could be successfully brought to complete dryness by vacuum. If

residual liquid could not be removed by vacuum, additional IPA, device heating to ~35 °C, and vacuum were applied. Monoliths in microfluidic devices prepared in this manner could then be stored under ambient conditions until use.

3.2.4 Experimental Setup

PTB biomarkers were fluorescently labeled and filtered using previously described procedures[32,37] for prelabeled biomarker experiments. Thrombin-antithrombin complex (TAT) was prepared 24 h prior to fluorescent labeling.[32] For on-chip labeling experiments, PTB biomarkers were diluted to the desired concentration in 10 mM BCB.

SPE experiments were performed in a previously described microscope setup for laser-induced fluorescence detection.[25,37] Fluorescence images were collected with either a Photometrics Cool-SNAP HQ2 CCD camera (Tucson, AZ) or a Hamamatsu ORCA-Fusion CMOS camera (Bridgewater, NJ). Prior to biomarker extraction, a monolith was prepared by adding IPA to the reservoir and allowing the channel to fill to the monolith by capillary action. Next, the IPA was replaced with 10 mM BCB (pH 10) and vacuum was applied for 3 min. Then, the liquid in the reservoir was replaced with 30% ACN (in 10 mM BCB), with vacuum application for 90 s. Finally, the same was done with 90% ACN for another 90 s. This process of flowing buffer, 30% ACN, and 90% ACN was repeated three times to clean and equilibrate the channel. The flow rate was estimated to be 0.5-1 μL/min.

After equilibration, SPE experiments were performed. For prelabeled biomarkers, vacuum was used to drive the following flow steps: BCB for 3 min, sample loading for 90 s, BCB buffer rinse three times for 90 s each, 30% ACN for 90 s, and 90% ACN for 90 s. Although most analytes were tested at several concentrations, the following concentrations were used for

each analyte for the reported data: ferritin, 10 nM; TNF, 100 nM; peptide 1, 500 nM; defensins, 200 nM; CRF, peptides 2-3, TAT, and lactoferrin 1 μM; and Alexa Fluor, 2 μM. For on-chip labeling experiments, a similar procedure was performed except two loading steps were performed (PTB biomarker for 90 s, then Alexa Fluor labeling solution for 90 s) followed by a 30 min incubation prior to the buffer rinse. During the incubation time, the reservoir was refilled with labeling solution as needed to prevent evaporative drying. For the reported data, the following concentrations were used for each analyte: peptide 1, 500 nM; CRF, 1 μM; peptides 2-3, 600 nM; defensins, 200 nM; lactoferrin, 60 nM; TNF, 100 nM; TAT and ferritin, 50 nM; and Alexa Fluor, 20 μM.

After each flow step, a fluorescence image was captured using 200 ms exposure (for both detectors). All images were analyzed using Image J (NIH; imagej.nih.gov) to obtain the fluorescent signal present on the monolith after each step of the process. The background signal was subtracted from each, then the values were normalized to the signal after sample loading for each experiment. Average signals from three replicates for each experiment are reported.

3.3 Results and Discussion

3D printed microfluidic devices for SPE were based on a design used previously by Parker et al.[25] However, the design was changed slightly by creating a horizontal port for attachment of external tubing, which allowed for easier interfacing with vacuum to drive fluid flow (Figure 3.1A-C). Because 3D printing was used for device fabrication, design modifications were straightforward to apply; the CAD design could be edited, and new devices could be 3D printed in less than 30 min.

Although several similar reversed-phase monolith formulations have been reported previously,[33-34,36] a new formulation was developed for these SPE experiments both to avoid the use of Tween-20 and to improve formation consistency. For initial development of the new monolith, a number of mixtures containing OMA (10-28%), EDMA (7-25%), 1-dodecanol (45-70%), cyclohexanol (0-12%), and DMPA (1%) were mixed and polymerized in microcentrifuge tubes. Visual inspection found that mixtures containing too high of a porogen content (not enough monomer and crosslinker) were viscous and transparent, while mixtures that did not contain enough porogens (too much monomer and crosslinker) were also transparent from lack of a porous structure. The most opaque mixtures were judged to have formed the most porous monolithic structures; these occurred when the total porogen content was 60-70% and the EDMA crosslinker accounted for at least 15% of the mixture.

Using these results, another series of mixtures containing the same components was prepared, placed in 3D printed microfluidic channels for polymerization and imaged with SEM (Figure 3.2). From the formation and flow properties of these monoliths, several observations can be made. First, monoliths that contained a higher porogen (1-dodecanol and cyclohexanol) content had higher flow rates than those with lower porogen content: the flow rates of the monoliths shown in Figure 3.2A-B were slower than those in Figure 3.2C-D, which were slower than those in Figure 3.2E-F. This meant that after polymerization was complete, it was more difficult to clear the unpolymerized material from the monoliths in Figure 3.2A-B than those in Figure 3.2E-F. Thus, those low-porogen-content monoliths (Figure 3.2A-B) were judged too dense for use in SPE experiments.

A second observation from the Figure 3.2 images is distinct morphological differences when the entire porogen content is comprised of 1-dodecanol (Figure 3.2, right column) instead

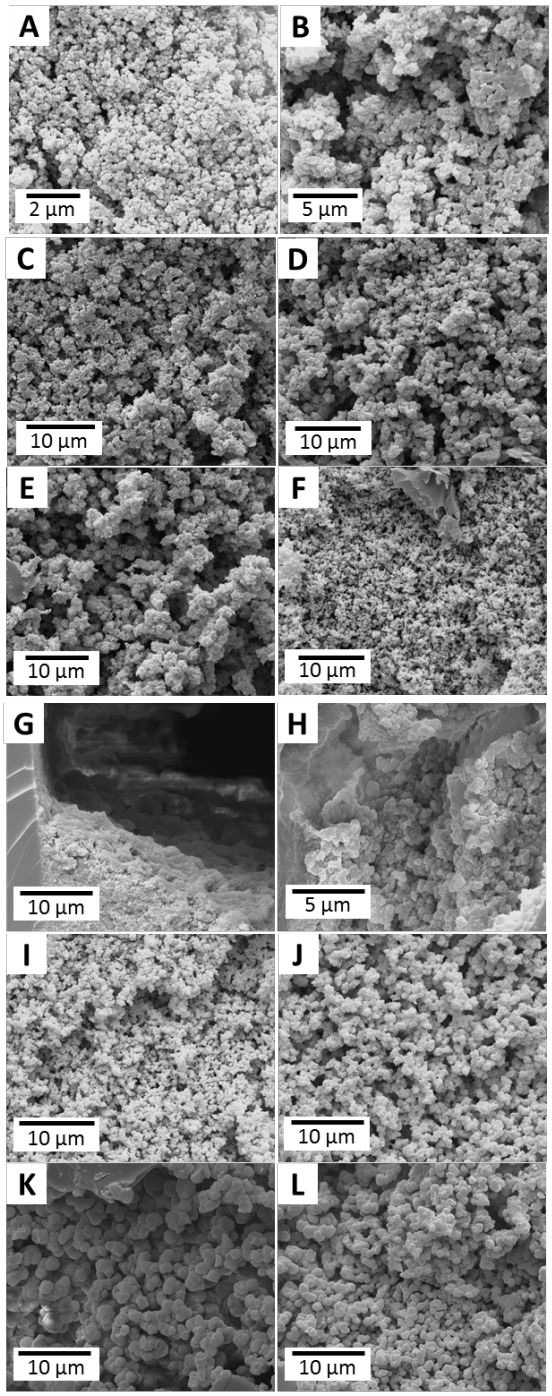

SEM	OMA	EDMA	1-Dodecanol	Cyclohexanol
A	20	20	50	10
B	20	20	60	
C	17.5	17.5	55	10
D	17.5	17.5	65	
E	15	15	60	10
F	15	15	70	
G	20	15	55	10
H	20	15	65	
I	15	20	55	10
J	15	20	65	
K	10	25	55	10
L	10	25	65	

M

Figure 3.2. SEM images of monoliths in 3D printed microfluidic channels. The monolith formulations consist of 1% DMPA initiator in a mixture of OMA, EDMA, 1-dodecanol, and cyclohexanol. (A-F) Monoliths in which the OMA:EDMA ratio was maintained at 1:1 while the OMA+EDMA:porogen ratio was varied. (G-L) Monoliths in which the porogen content was maintained at 65% total while the OMA:EDMA ratio was varied. (M) Table containing the monolith composition for each of the SEM images.

of if the mixture also contains 10% cyclohexanol (Figure 3.2, left column). I expected that the use of only 1-dodecanol would result in a greater number of smaller pores whereas the addition of cyclohexanol would result in fewer, but larger pores due to greater solubility of the OMA monomer in dodecanol.[38] However, these images suggest that the effects of these porogens may be more complex; morphological differences from porogen content, while significant, did not follow a simple trend.

A further observation from Figure 3.2G-L is the effect of maintaining constant porogen content while changing the ratio of OMA to EDMA (monomer to crosslinker). Figure 3.2G-H shows, similar to the microcentrifuge tube experiments described earlier, that monolith formation is inconsistent when there is not enough crosslinker present in the mixture. Thus, these images show that the monoliths are dense in some regions while other areas lack a monolith structure. It can also be observed that as the crosslinker concentration increases, the monolith pore and nodule sizes also increase (compare Figure 3.2I-J with K-L). This is likely because the greater number of reactive groups in EDMA draws the polymerizable units in the mixture into a larger, more rigid structure than when a higher percentage of OMA is present. These results indicate that the nodule and pore sizes, and thus the total surface area of the monolith, are tunable by changing the ratio of polymerizable groups in the monomer and crosslinker components.

These SEM results confirmed that several mixtures were good candidates for performing SPE. Specifically, those monolith mixtures shown in Figure 3.2C, F, J, and L appeared to be most promising, with good morphology and high surface area. To simplify formulations, the mixture from Figure 3.2C was excluded as it required two porogens. The remaining three monoliths were tested using a simple SPE experiment. I found that the vacuum-driven flow rate through monoliths as shown in Figure 3.2F was too high for efficient extraction to occur.

Although a smaller pressure drop might be able to slow the flow rate enough to correct this, no additional experiments were performed with this mixture. Extraction was also inefficient for the monolith mixture shown in Figure 3.2L, likely due to the low percentage of OMA in this formulation; the monolith was not hydrophobic enough to effectively extract ferritin, a model PTB protein biomarker.

The 15% OMA, 20% EDMA, and 65% 1-dodecanol monolith formulation was used in initial SPE experiments. Although the flow rate and hydrophobicity of this monolith were sufficient for extraction of ferritin, it did not allow for selective elution of excess fluorescent dye prior to the biomarker. For example, flow of just 30% ACN led to partial elution of ferritin. These results indicated that a more hydrophobic monolith was needed to retain all PTB biomarkers, particularly the smaller peptides. Since increasing the OMA percentage detrimentally altered the monolith morphology, instead, the OMA in the monolith from Figure 3.2J was replaced with LMA. This change had no noticeable effect on monolith morphology (compare Figure 3.1E with Figure 3.2J) but increased the hydrophobicity of the monolith enough to allow for PTB biomarker SPE with selective retention and elution. This LMA monolith was also found to have consistent attachment to the 3D printed channel surfaces (Figure 3.1D) and was well-confined to the polymerization window (Figure 3.3A).

With a suitable monolith formulation, the 3D printed microfluidic devices were ready for SPE experiments. In initial studies, I found that a fluorescent byproduct of Irgacure 819, the photoinitiator used during 3D printing, was present in the devices and soluble in the ACN eluent. This fluorescent impurity increased the background signal during point fluorescence detection experiments; however, imaging of fluorescence on the monoliths allowed effective monitoring of analyte present during extraction and elution without interference from the impurity.

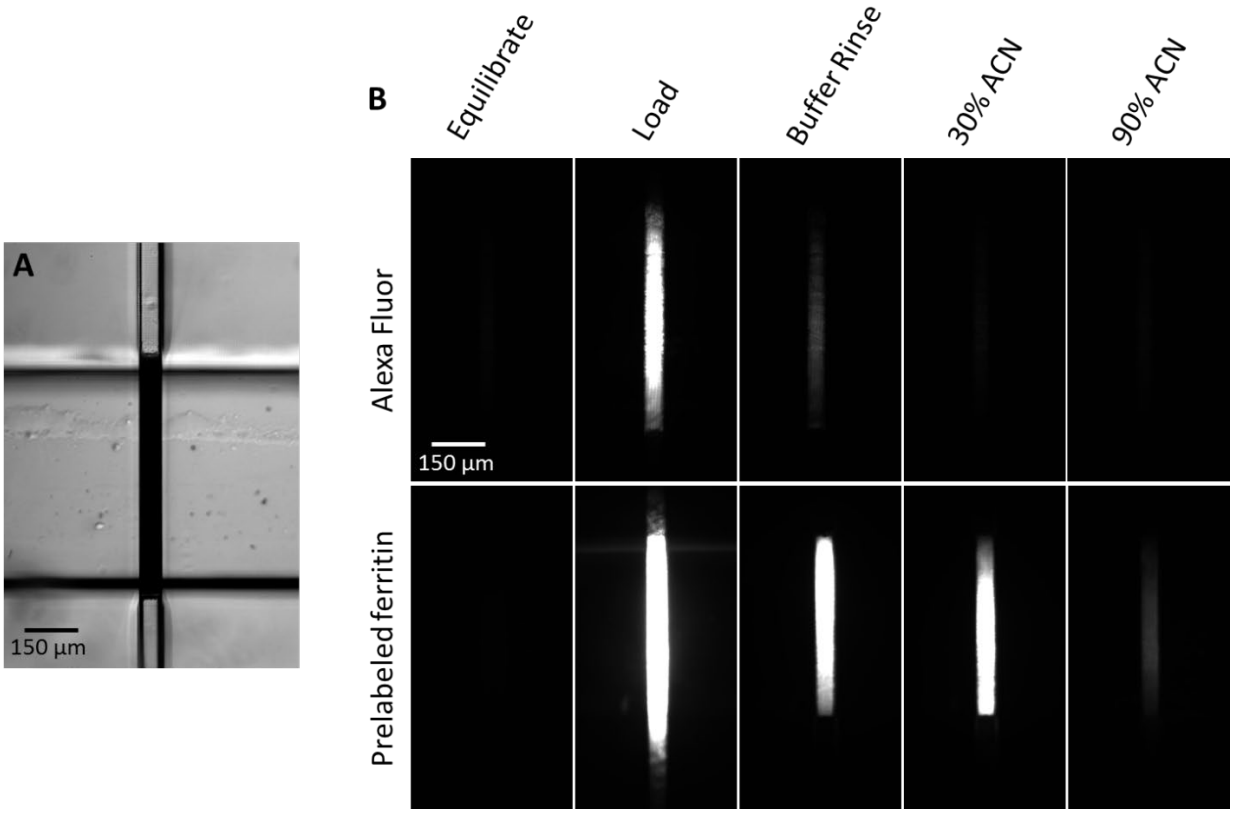

Figure 3.3. Images of reversed-phase LMA monoliths during SPE. (A) Photograph of a monolith showing formation and confinement within the polymerization window (visible as the two dark lines running horizontally through the image). (B) Fluorescence images of successive steps during SPE experiments including buffer equilibration, sample loading (Alexa Fluor or ferritin), buffer rinse, 30% ACN elution, and 90% ACN elution. Scale is the same in all images.

Using fluorescent imaging detection, the signal after the loading and elution of analytes could be monitored. I selected ferritin as a model biomarker analyte because its large size was expected to lead to strong retention on the reversed-phase monolith. To evaluate conditions for on-chip labeling, Alexa Fluor dye was used as another analyte for initial comparisons. The BCB (pH 10) used for loading also corresponds to the elution buffer of an immunoaffinity extraction system described earlier.[25] This matching of immunoaffinity eluent to SPE loading solution should facilitate integration of these two processes in a future PTB risk diagnostic.

The rinsing and elution solvents for Alexa Fluor and Alexa Fluor-labeled ferritin were chosen to allow for selective elution of the two analytes. Selective elution is essential for on-chip

labeling and should also allow biomarkers to be eluted in a small-volume, concentrated plug. Such an enriched band should help to lower limits of detection and enable heart-cut injection for subsequent microchip electrophoresis.[31,33] Similar to previous studies,[33-34] I found that Alexa Fluor could be eluted with only buffer or at low ACN concentrations. In contrast, the ferritin was strongly retained until 90% ACN was flowed through the monolith, at which time significant elution could be observed. Figure 3.3B shows representative images for both Alexa Fluor and ferritin elution. In each case, almost no fluorescent signal can be seen on the monolith during the buffer equilibration prior to sample loading. After loading, both monoliths show high fluorescent signal. In the Alexa Fluor experiments, the fluorescent signal is removed with buffer and 30% ACN, such that almost no fluorescent signal is visible in the image after 30% ACN flow. This indicates limited retention of Alexa Fluor with almost no material remaining after flowing 30% ACN. In contrast, the ferritin images show that the high fluorescent signal is maintained through the buffer and 30% ACN steps, demonstrating that ferritin is well retained. Lastly, the fluorescent signal on the monolith is lower after the 90% ACN elution, indicating good elution of the analyte and selective retention of ferritin compared to Alexa Fluor dye.

To show the versatility of this SPE system for additional analytes, a panel of nine PTB risk biomarkers (Table 3.1) was evaluated. These peptides and proteins were fluorescently labeled off chip, loaded on reversed-phase LMA monoliths using the established conditions, and then observed by fluorescence imaging after retention and elution. Figure 3.4A shows the relative fluorescent signal present on the monoliths for each analyte after loading and flowing buffer and two different percentages of ACN, demonstrating the retention and elution characteristics of the PTB biomarkers and fluorescent label. Figure 3.4B shows the percentage of each retained analyte eluted with 90% ACN. Of the nine proteins and peptides, four were well

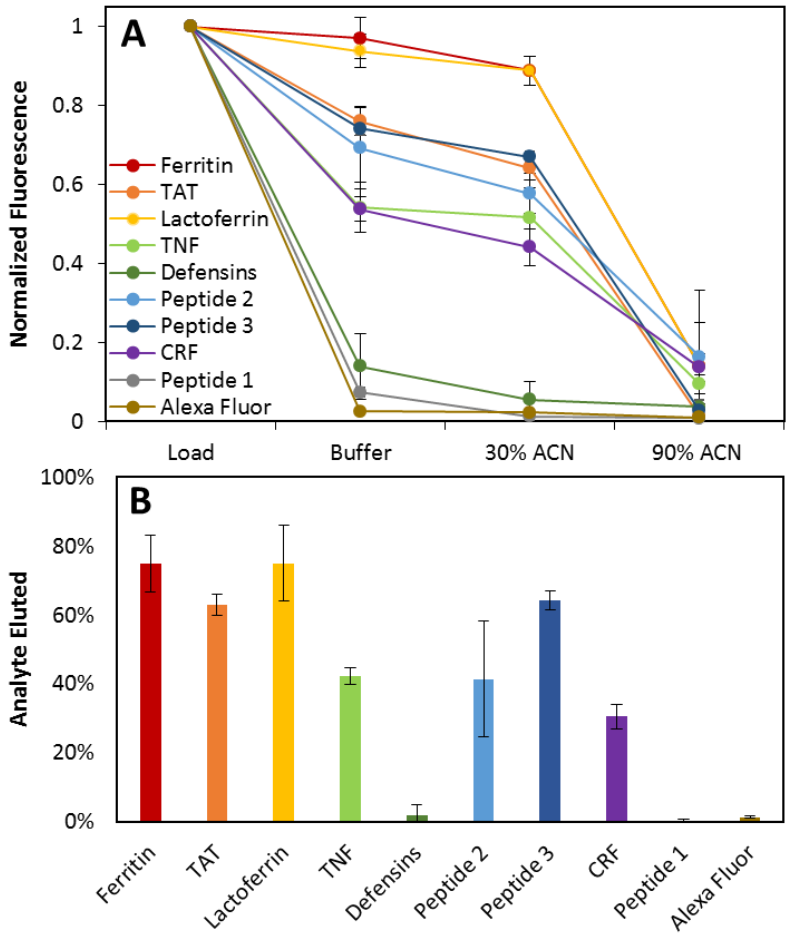

Figure 3.4 SPE of Alexa Fluor and prelabeled PTB biomarkers on LMA reversed-phase monoliths in 3D printed microfluidic devices. (A) Normalized fluorescent signal on the monolith after the load, buffer rinse, 30% ACN, and 90% ACN elution steps. (B) Percent of the total retained analyte eluted with 90% ACN. Error bars represent the standard deviation of three replicates.

retained during the buffer rinse and 30% ACN flow through steps, with >60% of the total captured material eluted during the 90% ACN step. Three additional biomarkers were moderately retained, with >30% of the total captured material eluted with 90% ACN. The final three analytes, Alexa Fluor, peptide 1, and defensins, were largely eluted during the buffer rinse step, indicating that these analytes were not strongly retained on the monolith.

As the conditions for the elution of analytes from these monoliths were chosen to selectively elute Alexa Fluor dye and retain ferritin, it is not surprising that different retention properties were seen for other analytes. It was expected for retention to correlate with the size of

the analyte, with large proteins well retained and small peptides having less retention. Table 3.1 shows that the panel of PTB biomarkers has more than a 100-fold range in masses and considerable variation in hydrophobic nature. Thus, the limited retention of peptide 1 was likely because of its small size, and the low retention of defensins was likely due to the higher relative hydrophilicity within its amino acid sequence. However, the remaining seven biomarkers were moderately or well retained, showing that this SPE system has potential to perform selective extraction through retention and elution of many proteins and peptides.

With these encouraging results for SPE of prelabeled proteins and peptides, I focused on coupling SPE with an on-chip fluorescent labeling reaction. In contrast with the previous experiments where PTB biomarkers were fluorescently labeled overnight in microcentrifuge tubes prior to extraction experiments, unlabeled biomarkers were loaded onto the monolith followed by labeling with Alexa Fluor at room temperature for 30 min prior to performing the rinsing and elution steps. Similar to Figure 3.4, Figure 3.5A shows relative fluorescence signal from monoliths after each step in the process for all 9 biomarkers plus the fluorescent label, whereas Figure 3.5B further shows the percentage of each retained analyte that was eluted with 90% ACN. Analysis of these elution percentages shows moderate to good selectivity for 90% ACN elution of all nine biomarkers relative to the Alexa Fluor label, whose elution is complete in 30% ACN. These results show the ability to perform on-chip fluorescent labeling of proteins and peptides having a variety of masses and hydrophobicities, with selective retention relative to the fluorescent dye. Importantly, these results also demonstrate the first use of 3D printed devices for on-chip labeling and purification of an entire panel of PTB biomarkers. The data further establish the ability to achieve good retention of all nine PTB biomarkers in SPE

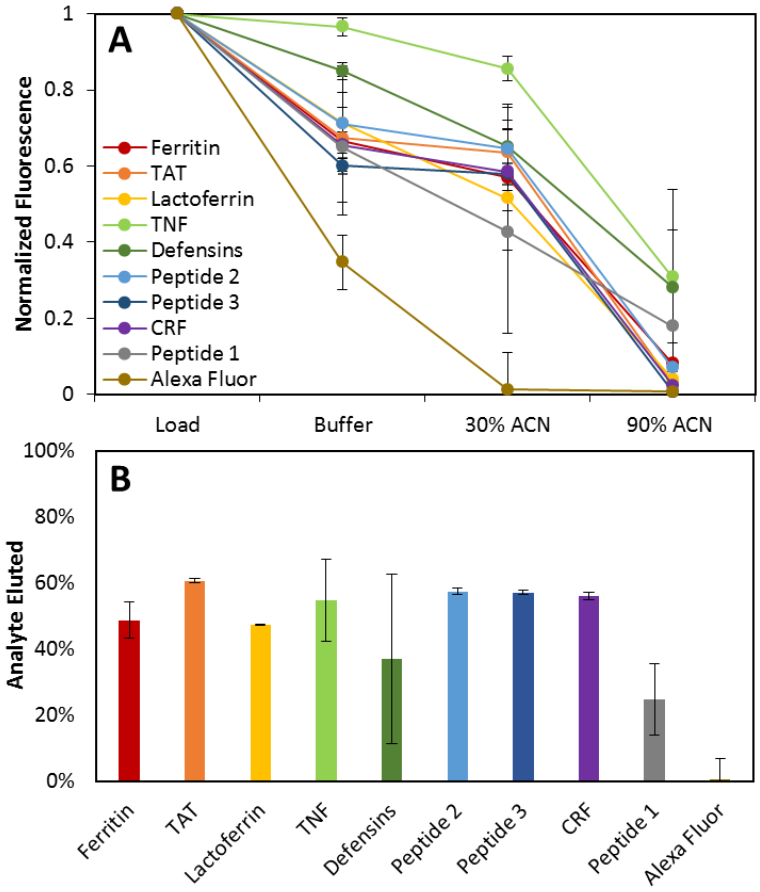

Figure 3.5. SPE and on-chip fluorescent labeling of PTB biomarkers on LMA reversed-phase monoliths. (A) Normalized fluorescent signal on the monolith after loading/labeling, buffer rinse, 30% ACN, and 90% ACN elution steps. (B) Percent of the total retained analyte eluted with 90% ACN.

combined with selective elution of excess dye prior to biomarker elution, all under identical conditions, a key step for streamlined on-chip sample preparation.

The on-chip labeling data in Figure 3.5 also shows that, unlike for the prelabeled biomarkers (Figure 3.4), retention for peptide 1 and defensins is significantly increased compared to the fluorescent dye. I hypothesized that this difference was due to the longer (30 min) labeling/incubation time, which increased interaction with the reversed-phase monolith for retention. To test the effect of the incubation time, peptide 1 prelabeled with Alexa Fluor was loaded with a 30-min extraction period prior to rinsing and elution. This extension of the

extraction period raised the percentage of peptide 1 eluted with 90% ACN to >25%, the same as observed for peptide 1 during on-chip labeling experiments. Thus, retention of small or hydrophilic analytes can be improved by increasing extraction time, further extending the utility of this SPE system to a variety of peptide and protein analytes.

In this work, I have demonstrated the feasibility of using 3D printed microfluidic devices to combine SPE and fluorescent labeling of nine individual analytes in a disease risk biomarker panel. The use of 3D printing for fabrication can make such devices widely available to other researchers. Moreover, 3D printing streamlines the integration of microfluidic assay components such as valves and pumps[39] and makes possible the combination of SPE and labeling with further sample preparation or separation steps.[25,35] Furthermore, this work is the first to evaluate the entire panel of nine PTB biomarkers in a miniaturized assay, which constitutes an important step toward the development of a complete PTB risk diagnostic. Finally, the ability for these processes to be applied to analytes that have different masses or hydrophobicities demonstrates the broad versatility of 3D printed microfluidic SPE systems for use in other peptide- and protein-based analysis applications.

3.4 References

1. Sonker, M.; Sahore, V.; Woolley, A. T. Recent advances in microfluidic sample preparation and separation techniques for molecular biomarker analysis: a critical review. *Anal. Chim. Acta* **2017,** *986,* 1-11.

2. Zhang, L.; Ding, B.; Chen, Q.; Feng, Q.; Lin, L.; Sun, J. Point-of-care-testing of nucleic acids by microfluidics. *Trends Anal. Chem.* **2017,** *94,* 106-116.

3. Kimura, H.; Sakai, Y.; Fujii, T. Organ/body-on-a-chip based on microfluidic technology for drug discovery. *Drug Metabol. Pharmacokin.* **2018,** *33,* 43-48.

4. Rothbauer, M.; Zirath, H.; Ertl, P. Recent advances in microfluidic technologies for cell-to-cell interaction studies. *Lab Chip* **2018,** *18,* 249-270.

5. Prakadan, S. M.; Shalek, A. K.; Weitz, D. A. Scaling by shrinking: empowering single-cell 'omics' with microfluidic devices. *Nat. Rev. Genet.* **2017,** *18,* 345-361.

6. Ahrberg, C. D.; Manz, A.; Chung, B. G. Polymerase chain reaction in microfluidic devices. *Lab Chip* **2016,** *16,* 3866-3884.

7. Kim, J.; Campbell, A. S.; de Ávila, B.E.; Wang, J. Wearable biosensors for healthcare monitoring. *Nat. Biotechnol.* **2019,** *37,* 389-406.

8. Wu, J.; Gu, M. Microfluidic sensing: state of the art fabrication and detection techniques. *J. Biomed. Optics* **2011,** *16,* 080901.

9. Nielsen, A. V.; Beauchamp, M. J.; Nordin, G. P.; Woolley, A. T. 3D printed microfluidics. *Annu. Rev. Anal. Chem.* **2020,** *13,* DOI: 10.1146/annurev-anchem-091619-102649.

10. Beauchamp, M. J.; Nordin, G. P.; Woolley, A. T. Moving from millifluidic sub-100-μm cross-section 3D printed devices. *Anal. Bioanal. Chem.* **2017,** *409,* 4311-4319.

11. Gong, H.; Bickham, B. P.; Woolley, A. T.; Nordin, G. P. Custom 3D printer and resin for 18 μm x 20 μm microfluidic flow channels. *Lab Chip.* **2017,** *17,* 2899-2909.

12. Zhao, C.; Ge, Z.; Yang, C. Microfluidic techniques for analytes concentration. *Micromachines* **2017,** *8,* 28.

13. Yu, C.; Davey, M. H.; Svec, F.; Fréchet, J. M. J. Monolithic porous polymer for on-chip solid-phase extraction and preconcentration prepared by photoinitiated in situ polymerization within a microfluidic device. *Anal. Chem.* **2001,** *73,* 5088-5096.

14. Farahani, A.; Sereshti, H. An integrated microfluidic device for solid-phase extraction and spectrophotometric detection of opium alkaloids in urine samples. *Anal. Bioanal. Chem.* **2020,** *412,* 129-138.

15. Park, M.; Seo, T. S. An integrated microfluidic device with solid-phase extraction and graphene oxide quantum dot array for highly sensitive and multiplex detection of trace metal ions. *Biosens. Bioelectron.* **2019,** *126,* 405-411.

16. Wu, Q.; He, J.; Meng, H.; Wang, Y.; Zhang, Y.; Li, H.; Feng, L. A paper-based microfluidic analytical device combined with home-made SPE column for the colorimetric determination of copper(II) ion. *Talanta.* **2019,** *204,* 518-524.

17. Campos, C. D. M.; Gamage, S. S. T.; Jackson, J. M.; Witek, M. A.; Park, D. S.; Murphy, M. C.; Godwin, A. K.; Soper, S. A. Microfluidic-based solid phase extraction of cell free DNA. *Lab Chip* **2018,** *18,* 3459-3470.

18. Mauk, M. G.; Song, J.; Liu, C.; Bau, H. H. Simple approaches to minimally-instrumented, microfluidic-based point-of-care nucleic acid amplification tests. *Biosensors.* **2018,** *8,* 17.

19. Brassard, D.; Geissler, M.; Descarreaux, M.; Tremblay, D.; Dauod, J.; Clime, L.; Mounier, M.; Charlebois, D.; Veres, T. Extraction of nucleic acids from blood: unveiling the potential of active pneumatic pumping in centrifugal microfluidics for integration and automation of sample preparation processes. *Lab Chip* **2019,** *19,* 1941-1952.

20. Zhang, Y.; Xiang, J.; Wang, Y.; Qiao, Z.; Wang, W. A 3D printed centrifugal microfluidic platform for spilled oil enrichment and detection based on solid phase extraction (SPE). *Sens. Actu. B: Chem.* **2019,** *296,* 126603.

21. Deng, J.; Ikenishi, F.; Smith, N.; Lazar, I. M. Streamlined microfluidic analysis of phosphopeptides using stable isotope-labeled synthetic peptides and MRM-MS detection. *Electrophoresis* **2019,** *39,* 3171-3184.

22. Buszewski, B.; Szultka, M. Past, present, and future of solid phase extraction: a review. *Crit. Rev. Anal. Chem.* **2012,** *42,* 198-213.

23. Knob, R.; Sahore, V.; Sonker, M.; Woolley, A. T. Advances in monoliths and related porous materials for microfluidics. *Biomicrofluidics* **2016,** *10,* 032901.

24. Svejdal, R. R.; Dickinson, E. R.; Sticker, D.; Kutter, J. P.; Rand, K. D. Thiol-ene microfluidic chip for performing hydrogen/deuterium exchange of proteins at subsecond time scales. *Anal. Chem.* **2019,** *91,* 1309-1317.

25. Parker, E. K.; Nielsen, A. V.; Beauchamp, M. J.; Almughamsi, H. M.; Nielsen, J. B.; Sonker, M.; Gong, H.; Nordin, G. P.; Woolley, A. T. 3D printed microfluidic devices with immunoaffinity monoliths for extraction of preterm birth biomarkers. *Anal. Bioanal. Chem.* **2019,** *411,* 5405-5413.

26. Gupta, V.; Beirne, S.; Nesterenko, P. N.; Paull, B. Investigating the effect of column geometry on separation efficiency using 3D printed liquid chromatographic columns containing polymer monolithic phases. *Anal. Chem.* **2018,** *90,* 1186-1194.

27. Carrasco-Correa, E. J.; Cocovi-Solberg, D. J.; Herrero-Martínez, J. M.; Simó-Alfonso, E. F.; Miró M. 3D printed fluidic platform in *in-situ* covalently immobilized polymer monolithic column for automatic solid-phase extraction. *Anal. Chim. Acta* **2020,** *1111,* 40-48.

28. *Survive and thrive: transforming care for every small and sick newborn*; World Health Organization: Geneva, 2019.

29. Esplin, M. S.; Merrell, K.; Goldenberg, R.; Lai, Y.; Iams, J. D.; Mercer, B.; Spong, C. Y.; Miodovnik, M.; Simhan, H. N.; van Dorsten, P.; Dombrowski, M. Proteomic identification of serum peptides predicting subsequent spontaneous preterm birth. *Am. J. Obstet. Gynecol.* **2011.** *204,* e1-8.

30. Sonker, M.; Parker, E. K.; Nielsen, A. V.; Sahore, V.; Woolley, A. T. Electrokinetically operated microfluidic devices for integrated immunoaffinity monolith extraction and electrophoretic separation of preterm birth biomarkers. *Analyst.* **2018,** *143,* 224-231.

31. Beauchamp, M. J.; Nielsen, A. V.; Gong, H.; Nordin, G. P.; Woolley, A. T. 3D printed microfluidic devices for microchip electrophoresis of preterm birth biomarkers. *Anal. Chem.* **2019,** *91,* 7418-7425.

32. Nielsen, J. B.; Nielsen, J. B.; Carson, R. H.; Lin, H.-J. L.; Hanson, R. L.; Sonker, M.; Mortensen, D. N.; Price, J. C.; Woolley, A. T. Analysis of thrombin-antithrombin complex formulation using microchip electrophoresis and mass spectrometry. *Electrophoresis* **2019,** *40,* 2853-2859.

33. Sahore, V.; Sonker, M.; Nielsen, A. V.; Knob, R.; Kumar, S.; Woolley, A. T. Automated microfluidic devices integrating solid-phase extraction, fluorescent labeling, and microchip electrophoresis for preterm birth biomarker analysis. *Anal. Bioanal. Chem.* **2018,** *410,* 933-941.

34. Kumar, S.; Sahore, V.; Rogers, C. I.; Woolley, A. T. Development of an integrated microfluidic solid-phase extraction and electrophoresis device. *Analyst.* **2016,** *141,* 1660-1668.

35. Beauchamp, M. J.; Gong, H.; Woolley, A. T.; Nordin, G. P. 3D printed microfluidic features using dose control in X, Y, and Z dimensions. *Micromachines* **2018,** *9,* 326.

36. Yang, R.; Pegaduan, J. V.; Yu, M.; Woolley, A. T. On chip preconcentration and fluorescence labeling of model proteins by use of monolithic columns: device fabrication, optimization, and automation. *Anal. Bioanal. Chem.* **2015,** *407,* 737-747.

37. Nielsen, A. V.; Nielsen, J. B.; Sonker, M.; Knob, R.; Sahore, V.; Woolley, A. T. Microchip electrophoresis separation of a panel of preterm birth biomarkers. *Electrophoresis* **2018,** *39,* 2300−2307.

38. Vlakh, E. G.; Tennikova, T. B. Preparation of methacrylate monoliths. *J. Sep. Sci.* **2007,** *30,* 2801-2813.

39. Gong, H.; Woolley, A. T.; Nordin, G. P. High density 3D printed microfluidic valves, pump, and multiplexers. *Lab Chip* **2016,** *16,* 2450-2458.

4. ITERATIVE DEVELOPMENT OF FLUIDIC DEVICES FOR BIOLOGICAL APPLICATIONS

4.1 Introduction

When developing a fluidic device for a biological application, several aspects should be considered such as the material of the device. Many applications with specific compatibility or reagent requirements are only compatible with a limited number of materials.[1] A similar consideration is the ease of fabrication. As discussed in Chapter 1.2, some microfabrication techniques are simpler than others. However, materials that are compatible with simpler fabrication methods may not be compatible with the application or analytical methods being developed.[2]

Regardless of material and fabrication method choice, most fluidic devices require several iterations of fabrication and testing when being developed for a new application.[3] Often, these developmental iterations will begin with a simplified design then increase in complexity to allow relevant experimental techniques and procedures to be established in a controlled manner. Indeed, good scientific investigations often proceed by step-by-step improvements to existing protocols and procedures. Furthermore, incremental improvements help to establish proof of concept, the priority and importance of experimental procedures, and efficient problem solving.[3]

This chapter describes two projects that involve developing fluidic devices for biological applications. In both cases, I performed device design and fabrication at BYU, while most testing and feedback on device performance occurred via collaboration with researchers at another institution. Although the material and fabrication requirements of each project were different,

both required iterative enhancements to a simple device design to improve performance and increase the design complexity to reach a larger goal.

4.2 Device Design and Fabrication for Point-to-Point DNA Nanowire Assembly

4.2.1 Introduction

For many years, electrical components, particularly transistors, have been decreasing in size. The miniaturization of electronics for embedded systems, memory storage devices, and computers has become the focal point of many nanofabrication techniques.[4-5] While the size decrease to the nano-scale comes with high cost, waste, and complexity for typical top-down fabrication methods, alternate bottom-up fabrication can avoid many of these disadvantages.[6] One such bottom-up fabrication method is the use of DNA origami as a scaffold for selective metallization to form electrical components such as wires, diodes, and transistors. This process involves the simple, yet selective, folding of DNA scaffold and staple strands into a specific 2- or 3-dimensional shape.[7-9] The origami can then be modified to form nanowires,[10-11] metal-metal junctions,[12] or metal-semiconductor junctions.[13-14]

As research into DNA-based nanoelectronics progresses, a method is needed to selectively connect the nanocomponents, particularly when the exact location or orientation of these components is not predetermined. One proposed method to solve this problem involves the integration of work previously performed in Dr. Rebecca Schulman's lab at Johns Hopkins University (JHU) and the Woolley lab at BYU. Such integration involves the self-assembly of a DNA nanotube between two terminals, successful metallization of the nanotube to form a

nanowire, and use of the connected electrodes to electrically characterize the nanowire. This work would constitute an important contribution to self-assembled nanoelectronics.

Previous work by the Schulman lab[15] has shown that it is possible to self-assemble DNA nanotubes between two glass surfaces. In this process (Figure 4.1), glass coverslips are separately modified with seeding solutions for DNA attachment. The two surfaces are glued together (10 µm spacing) and filled with a DNA "tile" solution, which self-assembles to form DNA nanotubes with selective attachment to the two seeded surfaces.

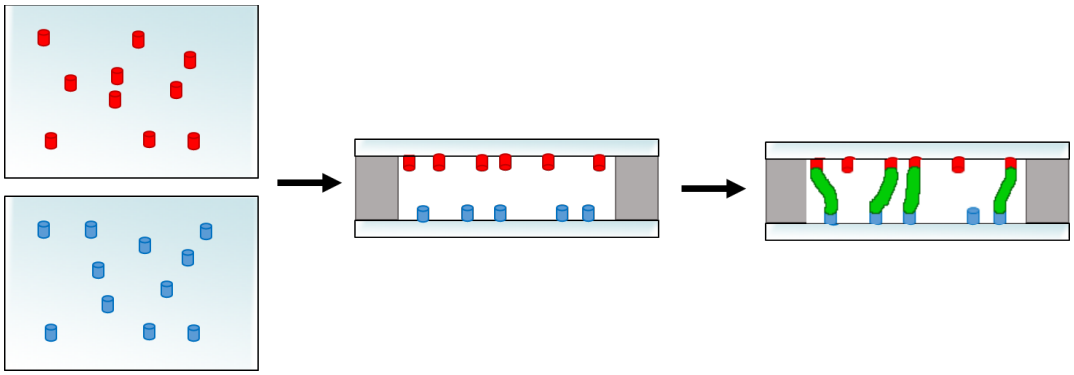

Figure 4.1. Point-to-point attachment of DNA. Glass slides are separately modified with DNA seeds (red and blue). The glass slides are placed together with a spacer. The gap is filled with seeding solution and the edges are glued to prevent evaporation. The glass device is incubated to grow DNA nanotubes between the two seeded surfaces.

To further develop the JHU method for DNA nanotube growth for downstream metallization and nanowire characterization, experimental changes need to be implemented. First, the seeding modification for DNA nanotube growth needs to occur selectively on surfaces other than glass. Direct attachment of the nanotube to patterned electrodes would allow for electrical characterization of the nanowire, once formed. Next, consideration would need to be taken during device or experimental design to allow characterization of a single nanowire. Finally, a more controlled method of fluid input would be needed to control nanotube and

nanowire formation; such fluid control can be easily implemented using milli- or micro-fluidic channels.

To realize these goals, I designed and fabricated a series of millifluidic devices for DNA surface seeding and nanotube formation. Fabrication utilized both multi-layer photolithography and soft lithography methods. Additionally, I incorporated electrodes fabricated from two metals, gold and nickel, as surfaces for seeding attachment and future characterization of the nanowires. The series of fluidic devices are described in this chapter.

4.2.2 Materials and Methods

Materials. Devices were fabricated from either glass slides (75 mm x 50 mm x 1 mm) purchased from Corning (Corning, NY) or coverslips (22 mm x 40 mm x 0.2 mm) from VWR (Center Valley, PA). Photolithography was performed with S1805 photoresist from MicroChem (Westborough, MA) and MF-26A developer from Dow (Midland, MI). Feature patterns on the glass were fabricated from gold, nickel, or Sylgard 184 polydimethylsiloxane (PDMS) from Dow. Devices were cleaned either with deionized water or methanol from Macron (Center Valley, PA). Nanoport fittings for world-interfacing came from IDEX (Lake Forest, IL).

Fluidic Device Fabrication. Fluidic devices were fabricated using either glass slides or coverslips by spin coating S1805 photoresist and exposing the resist through a photomask on a Suss aligner (Corona, CA) and developing with MF-26A developer. After patterning, some fluidic devices had 100 nm-thick gold or nickel metal deposited onto the surface using a Denton vacuum e-beam evaporator (Moorestown, NJ) or a custom thermal evaporator, respectively. Excess metal and photoresist were lifted off using methanol and sonication (Branson 2510, North Olmstead, OH). If a PDMS layer was being patterned on the surface, the glass was treated to a similar photolithography procedure followed by spin coating deposition of PDMS (10:1 base-to-

curing agent and degassed for 30 min). Coated devices were placed in a 90 °C oven for one hour to cure. Once cooled, the PDMS could be cut using a VLS4.60 laser cutter (Universal Laser Systems, Scottsdale, AZ) set at 40% power, 100% speed, and 500 pulses per inch, and holes were drilled in the glass using a 1-mm diameter diamond-tipped drill bit (Drilax, Warren, NJ). Once fabricated, fluidic devices were carefully packaged to prevent breakage and shipped to the JHU collaborators for testing.

4.2.3 Results and Discussion

To create a fluidic device for DNA nanotube and nanowire formation and characterization, plans were made to create electrode junctions from gold and nickel placed 4-10 µm apart and enclosed within fluidic channels (Figure 4.2). The use of these two metals would allow each to be selectively seeded for DNA growth and, after metallization of the DNA, would be electrically conductive for nanowire characterization. The fluidic channel enclosure would be ~1 mm x 20-50 µm to allow easy use of syringe pumps to drive fluid flow. Later, these channel dimensions could be reduced to use less reagent. In order to allow for imaging of electrode

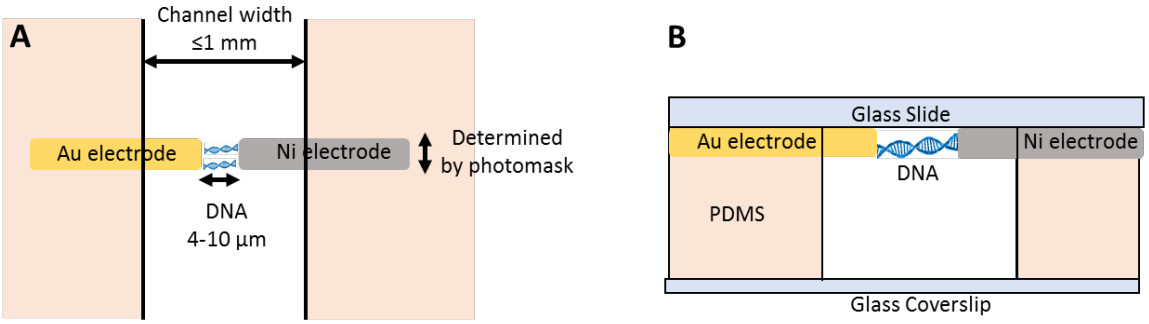

Figure 4.2. Schematic of the proposed fluidic device for DNA nanowire formation and characterization. A fluidic channel is enclosed using PDMS and glass. Gold and nickel electrodes protrude into the fluidic channels for selective DNA seeding and growth of DNA nanotubes. Each fluidic channel contains several of these electrode junctions for multiple measurements. (A) Top view of an electrode junction in a fluidic channel. (B) Cross-sectional view.

junctions using the JHU confocal microscope, the top and bottom surfaces of the device would be glass while the side walls were patterned PDMS. The use of PDMS would allow for either permanent or reversible closure of device channel via plasma bonding or van der Waals interactions, respectively.[16] Each glass-PDMS channel would enclose a series of electrode junctions for simultaneous experiments.

To realize the goals presented by this fluidic device conceptualization, I began by fabricating a simple flow channel device using glass and PDMS (Figure 4.3). This device would allow the researchers at JHU to practice *in situ* fabrication including attachment of Nanoport interface connectors and reversible bonding of glass-PDMS devices. Additionally, these devices would provide a simple system to determine appropriate flow conditions for future experiments

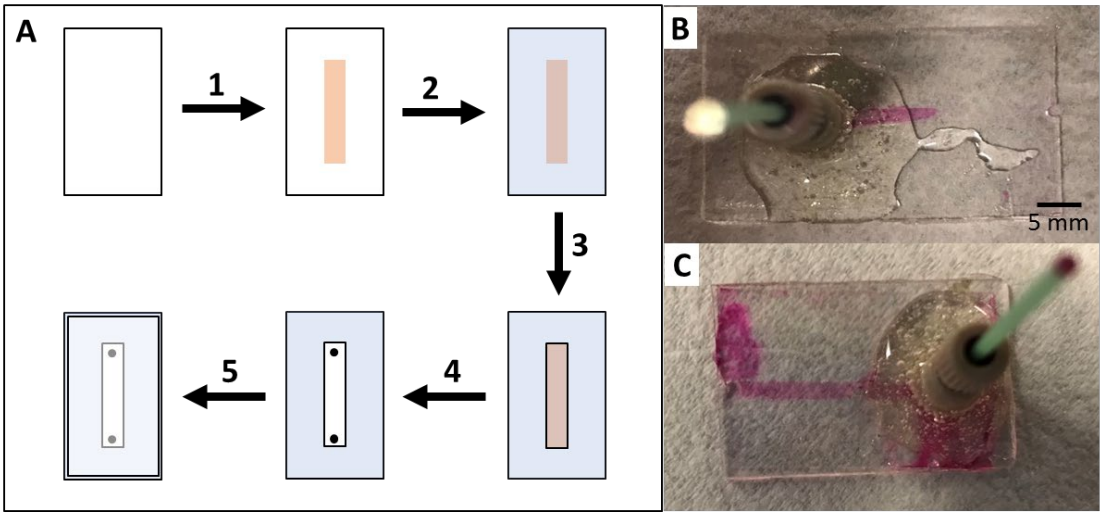

Figure 4.3. Microfluidic device fabrication for 3D DNA point-to-point attachment. (A) (1) A channel (5 mm x 25 mm x 100 nm) is patterned onto a glass slide using photolithography. (2) A 4-20 µm thick layer of PDMS is spun onto the glass slide. (3) After curing, the PDMS layer only is cut along the channel pattern using a laser cutter, allowing solvent access to the underlying photoresist. (4) The photoresist is dissolved with methanol, lifting off the PDMS in the channel area. Holes are drilled into the glass at the top and bottom of the channel area. (5) The PDMS-patterned glass is reversibly sealed to glass coverslips using van der Waals interactions. Nanoports may be affixed to the openings for syringe-pump assisted fluid flow. (B-C) Devices fabricated at BYU (steps 1-4) and assembled at JHU (step 5) show good flow of rhodamine through the channel. Photographs were taken by Dr. Sisi Jia at JHU.

within these fluidic systems. These simple fluidic devices were created (Figure 4.3A) using photolithography to pattern a 1 mm x 100 nm channel-like feature on the glass with photoresist. Next, I spin-coated a 4-20 μm layer of PDMS on top of the glass and photoresist. After curing, I used a laser cutter to selectively cut through the PDMS surface layer without damaging the underlying glass. This cut allowed for solvent-assisted liftoff of the PDMS within the channel region. After holes were drilled into the glass, the devices were shipped to JHU, where my collaborators were able to perform flow experiments with them. Figure 4.3B shows two devices in which the JHU collaborators reversibly bound a glass coverslip to the PDMS surface, attached a Nanoport connector, and flowed rhodamine dye through the channel.

The next step to realizing an integrated nanowire formation fluidic device was to establish conditions for DNA seeding on gold and nickel surfaces. To test such seeding, a design for "patch electrodes" was proposed (Figure 4.4A). These patch electrodes consist of metal squares placed either 5 or 10 μm apart on a glass surface. These devices could then be exposed to seeding and tile solutions for seeding of the metal surface and DNA nanotube growth. Since gold-attachment chemistry via a thiol is well known, initial experiments used gold patch electrode devices.

Based on the single patch electrode design (Figure 4.4A), I made two devices which would provide 18 connection points each for DNA seeding and nanotube growth experiments on top of 22 x 40 mm^2 glass surfaces (Figure 4.4B-C). Fabrication of these devices involved photolithography on a glass coverslip followed by 100-nm thick gold layer deposition on a chromium adhesion layer. Excess gold could be lifted off using a combination of a solvent and sonication. Although sonication resulted in a faster liftoff, prolonged exposure to sonication (>30 s) caused the gold patches to pit and lift off from the glass surface (Figure 4.4D). However,

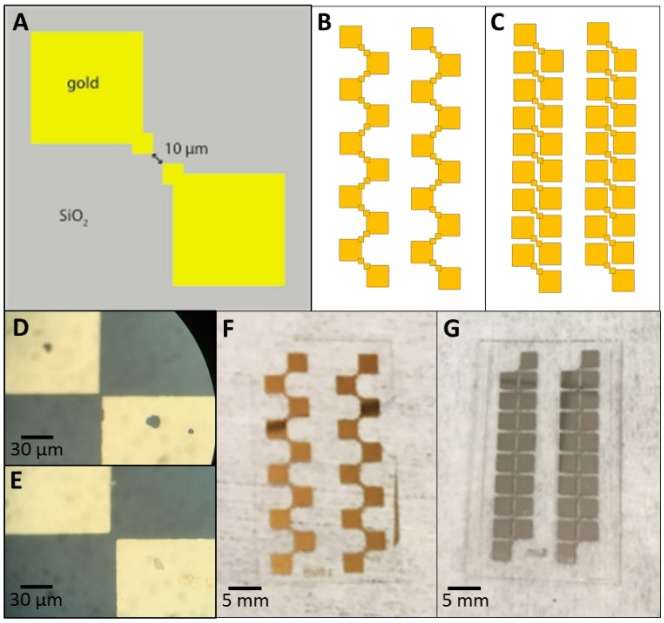

Figure 4.4. Patch electrode device designs for testing of DNA attachment and nanotube growth on a metal surface. (A) Schematic of gold metal patch electrodes fabricated on a glass surface. The gap between the electrodes during fabrication is either 5 or 10 µm. (B) Schematic design of zig-zag patch electrodes on a glass coverslip providing 18 electrode gaps for DNA nanotube growth. (C) Schematic design of packed patch electrodes on a glass coverslip. This design also provides 18 electrode gaps. (D) Microscope photograph of a gap between two gold electrodes (5 µm gap spacing, light color is the gold patch electrodes, dark gray is the glass surface), showing pitting and defects in the gold surface due to excess sonication. (E) Microscope photograph of the gap between two gold electrodes (10 µm gap spacing) in which the electrodes are well formed. (F) Photograph of a gold zig-zag patch electrode device. (G) Photograph of a nickel packed patch electrode device.

shorter sonication times allowed the patch electrodes to be cleanly and quickly fabricated (Figure 4.4E-F). Building on these results with gold, nickel patch electrodes were fabricated in a similar manner (Figure 4.4G).

Initial experiments of DNA seeding onto gold patch electrode surfaces were encouraging. Figure 4.5 shows confocal microscope images of DNA seeds attached to the gold surfaces near the patch electrode junction points. While a few DNA seeds are also visible on the glass surfaces, the JHU collaborators were optimistic that gold seeding was occurring and that the seeding process would be more selective in a fluidic device. However, they found that these devices were

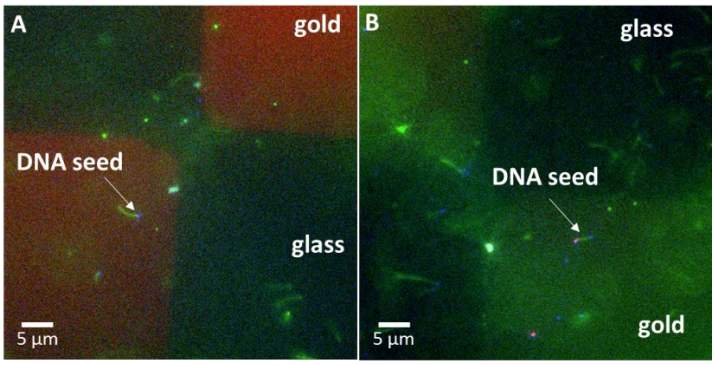

Figure 4.5. Confocal microscope images showing DNA seeded onto gold patch electrode devices. DNA seeds are visible as in both images as blue dots and light green rods on the surface of the device. Images obtained from Dr. Sisi Jia at JHU.

difficult to image due to the need to flip the device upside-down on the confocal microscope. Furthermore, they found that it was difficult to replace the buffer solution in the device for DNA nanotube growth due to liquid runoff.

To address the imaging and solvent problems associated with initial patch electrode devices, it was determined to pattern a layer of PDMS on top of the patch electrode devices already being used (Figure 4.6A-B). This PDMS layer would create a boundary to hold the buffer mixtures in place over the regions of interest while also providing a way to reversibly seal these regions for microscope imaging. Figure 4.6C shows a schematic outline of how such a device would be utilized to perform and characterize successive steps of DNA nanotube growth.

Similar to past devices, these PDMS-patch electrode devices were fabricated using photolithography and metal deposition/liftoff to pattern the electrodes followed by photolithography, spin-coating, and selective laser cutting to fabricate the PDMS layer on top. A batch of these devices was fabricated at BYU and sent to JHU for experiments. Unfortunately, the JHU researchers were not able to successfully remove the glass coverslip and re-hydrate the device surface after imaging (Figure 4.6C, step 4). Additionally, although several methods were

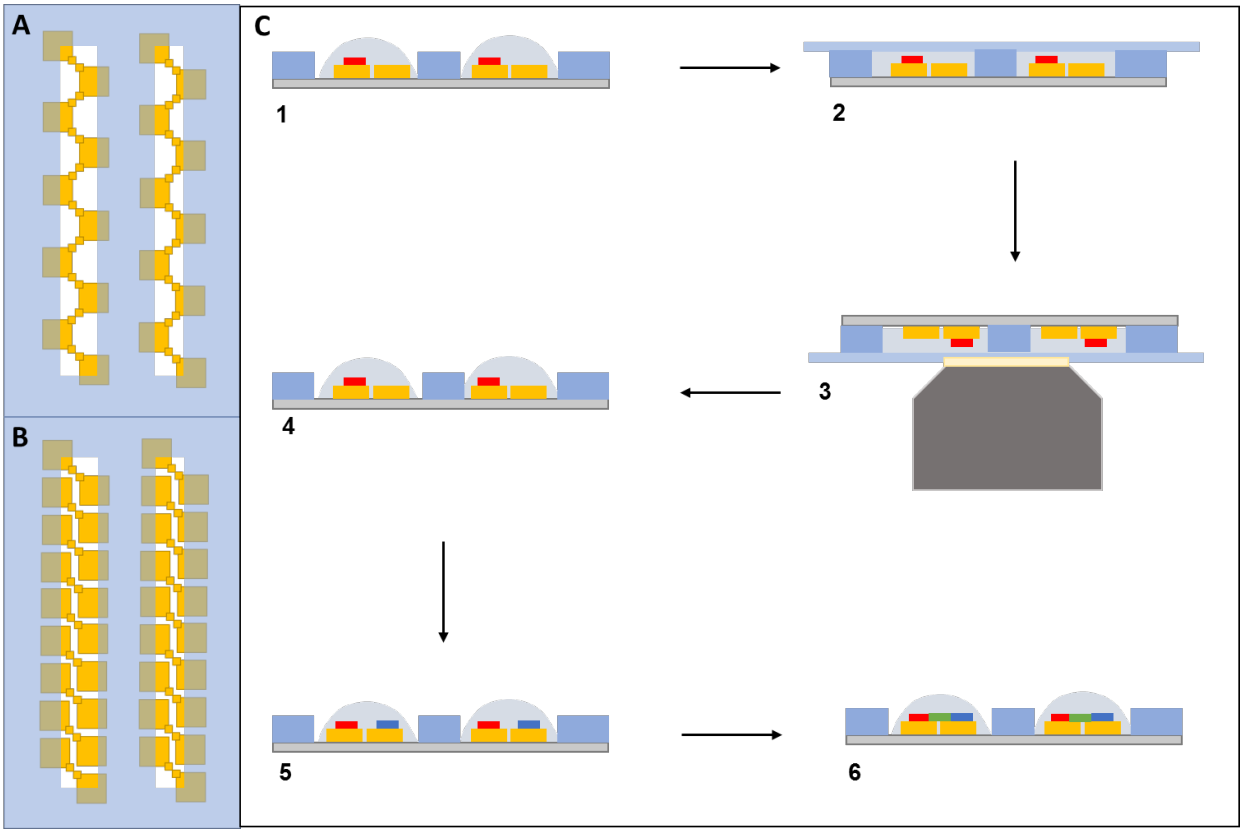

Figure 4.6. Schematic of the addition of a PDMS layer to the patch electrode design and the experimental procedure for DNA nanotube growth on these devices. (A-B) PDMS layer (blue) patterned on top of patch electrode devices (see Figure 4.4). (C) Experimental process to grow DNA nanotubes on the patch electrodes. (1) A-seeds (red) in buffer are put onto the device to seed the metal surface. (2) A coverslip is gently pressed to the surface to prevent solvent loss. (3) The device is imaged upside down on a confocal microscope to confirm seeding distribution. (4) The coverslip is removed, and lost buffer is restored. (5) B-seeds (blue) are attached to the gold surface. Steps 2-4 are repeated to check distribution. (6) Tile mixture is added to form DNA nanotubes (green) between the A- and B-seeds. Steps 2-4 are repeated to image tube formation. Schematic obtained from Dr. Sisi Jia at JHU.

proposed for the selective attachment of DNA seeds to nickel electrodes,[17-18] successful selective seeding procedures have yet to be established.

4.3 Design and Fabrication of Multi-Inlet Droplet Formation Devices for Cellular Drug Testing

4.3.1 Introduction

It is well known in medicine that a given treatment will not have the same effect on different people.[19] It has only been within the last few decades that pharmaceutical response has been linked to the patient's genetic makeup.[20-21] The discovery of this linkage has given rise to the potential of personalized medicine, where individual treatment options can be offered based on the combined use of personal health history, molecular and genetic information, and general clinical information.[22] Indeed, pharmacogenomics, or the study of treatment efficiency dependence on genetic makeup, has been hailed as one of the greatest promises for future medicine.[23-24]

The implementation of pharmacogenomics into cancer treatment is both difficult and promising. Although a tumor from a particular tissue and patient will usually share the same mutations, the genomic makeup of cancer variants between different tissues and patients is quite broad.[25] These variations can result in a chemotherapy treatment with toxicity to both healthy and cancer cells. However, with the correct pharmacogenomic information, treatment can be personalized to target a specific patient's cancer tissue rather than generalized cellular toxicity.[26]

The difficulty in developing a pharmacogenetic approach to cancer treatment is that it requires extensive drug testing to be completed with only the limited number of cells provided by a biopsy.[27] To solve this problem, researchers in Dr. Christoph Merten's lab at the European Molecular Biology Laboratory (EMBL) have developed a PDMS microfluidic device capable of inputting and mixing up to 16 samples and reagents (further expansion is possible) and droplet

generation from these solutions for fast, high-throughput cancer treatment testing.[27] Furthermore, this microfluidic device can be coupled to upstream cancer cell sorting and downstream barcode reading to further automate and further increase the throughput of drug screening.[28]

Like many other microfluidics researchers, those in the Merten lab found that traditional microfabrication methods became more challenging to manufacture for future commercialization as the complexity of the device increased (see Chapter 1.2). Having seen capabilities of the custom 3D printer in the Nordin lab at BYU,[29] the Merten group saw 3D printing as an attractive option for future fabrication of their cancer screening devices. Thus, I had the opportunity to work with several EMBL researchers to design and test increasingly complex 3D printed microfluidic devices which could be used in a similar way to the aforementioned PDMS devices. These 3D printed devices utilized all three spatial dimensions, and had 50 x 50 μm^2 channels, 150-300 μm diameter pneumatic valves, and a series of interface ports to both mimic and miniaturize the PDMS design. The devices I developed are simple and small enough to allow for many input solutions, though additional testing and material considerations will need to be addressed prior to full implementation.

4.3.2 Materials and Methods

Materials. Glass slides (25 mm x 75 mm x 1 mm) were purchased from VWR (Center Valley, PA), scored into thirds, and chemically modified using a 10% solution of 3-(trimethoxysilyl)propyl methacrylate from Sigma (St. Louis, MO) in toluene from Macron (Center Valley, PA) prior to 3D printing. 3D printing resin was made from poly(ethylene glycol) diacrylate (PEGDA; MW 250 Da) and phenylbis(2,4,6-trimethylenzoyl)phosphine oxide (Irgacure 819) from Sigma and 2-nitrophenyl phenyl sulfide (NPS) from TCI Chemicals

(Portland, OR). Isopropyl alcohol (IPA) and acetone were from Macron. Finally, PTFE tubing (0.022 in ID x 0.042 in OD) from Cole Parmer (Vernon Hills, IL) was glued into 3D printed devices using a UV curable glue (DecorRom, Shenzhen, China).

3D Printing. Using input from EMBL collaborators, a previously published microfluidic device design[27] was modified using OpenSCAD (openscad.org) into a design that could be created with Nordin's 3D printer. Considerations included total device size, valve structure, 3D geometry, and chip-to-world interfacing. The designs varied in complexity, from two to five solution input ports and from two to eight valve pneumatic control ports. All fluidic channels were designed to be 6 pixels (46 μm) wide by 5 layers (50 μm) tall while pneumatic control channels were 14 pixels (106 μm) wide by 7 layers (70 μm) tall. The valves were 20-40 pixels (150-300 μm) in diameter with 5-15 μm thick membranes.

The microfluidic devices were fabricated on a custom 3D printer with a 365 nm LED using a custom resin consisting of 1% Irgacure 819 and 2% NPS in PEGDA.[29] The bulk material of the devices consisted of 10 μm layers, exposed for 600 ms each. The 3 pixels and 3 layers immediately surrounding fluidic channels were only exposed for a shorter 400 ms interval to ensure that channels were void of polymerized material for easier flushing. Valve membrane layers were 5 μm thick and were exposed for 350 ms.

After printing, the microfluidic devices were flushed to remove all unpolymerized resin from the voids using a combination of IPA, vacuum, and up to 35 psi air. The devices were post-exposed for 20-30 min using a 405 nm LED with 11 $mW \cdot cm^{-2}$ irradiance to increase device strength and valve membrane durability.[29-30] Then, devices were visually inspected with a microscope for feature fidelity. In some cases, PTFE tubing was glued into the ports, and 15-20

psi air was used to check valve membrane function. Finally, 3D printed devices were packaged and shipped to EMBL for further testing.

4.3.3 Results and Discussion

As described above, the EMBL collaborators had previously developed and tested PDMS microfluidic devices for multi-input generation of aqueous droplets separated by oil interfaces for cancer drug testing.[27] Two of their CAD designs with 4- and 8-sample input ports are shown in Figure 4.7. In these devices, the input ports are interfaced to syringe pumps for continuous fluid flow. The aqueous analytes flow through the device to the valve region, where each flow is split. The direction of flow is controlled by a series of 400 µm-wide chambers or valves resting

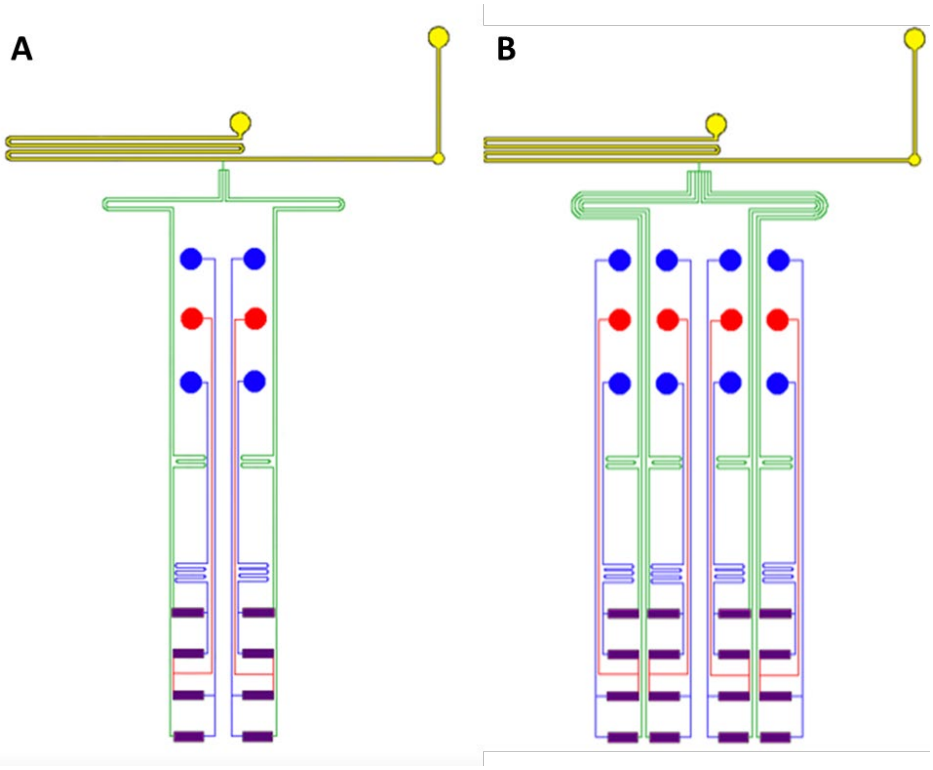

Figure 4.7. CAD designs of PDMS microfluidic devices for the flow of cells or other analytes into an oil medium for droplet formation. Blue corresponds to analyte entry ports and channels, purple are Braille valve chambers, green are aqueous analyte flow channels toward the oil region, yellow are oil flow channels and ports, and red are analyte waste channels and ports. (A) Four-input design. (B) Eight-input design.

on top of a Braille display with pins that can alternate pushing on the chambers to open and close each direction to fluid flow. One direction of flow goes into a waste channel where sample exits the device and is disposed while the other direction flows to a junction where all sample channels are merged before joining with the oil channel where droplet formation occurs.

The transition of the Figure 4.7 designs into a 3D printing design required several modifications. First, the build area of the 3D printer is over 10 times smaller than the corresponding PDMS chips, which required a more compact design while still being able to accommodate up to 16 inputs in the final integrated device. Next, the total travel distance or channel length of each analyte needed to remain the same. In the PDMS device, several serpentine regions were added to normalize the distance each analyte would travel through the device. Similar accommodations were made in the 3D printed design. Finally, the PDMS device used Braille valves to control the flow direction of the analytes. In replacement, the 3D printed device included pneumatic valves, each requiring an interface control connection.

Due to the complexity of creating a complete multi-inlet device, similar, simplified test devices were designed and 3D printed first. The first test devices (Figure 4.8A-B) utilized a signal input channel which split into two directions under control by two valves. The waste channels exiting these valves joined into a single waste port for collection. This microfluidic test device was small enough that five units could be 3D printed simultaneously in about 30 min.

After preliminary testing, the EMBL collaborators found that it was difficult to monitor the function of the pneumatic valves. Since the waste channels joined before exiting the device, the EMBL researchers couldn't always determine if the valves were successfully blocking fluid flow in that direction. To make this monitoring easier, a second waste port and channel were incorporated in a new design (Figure 4.8C-D). With this modification, the EMBL collaborators

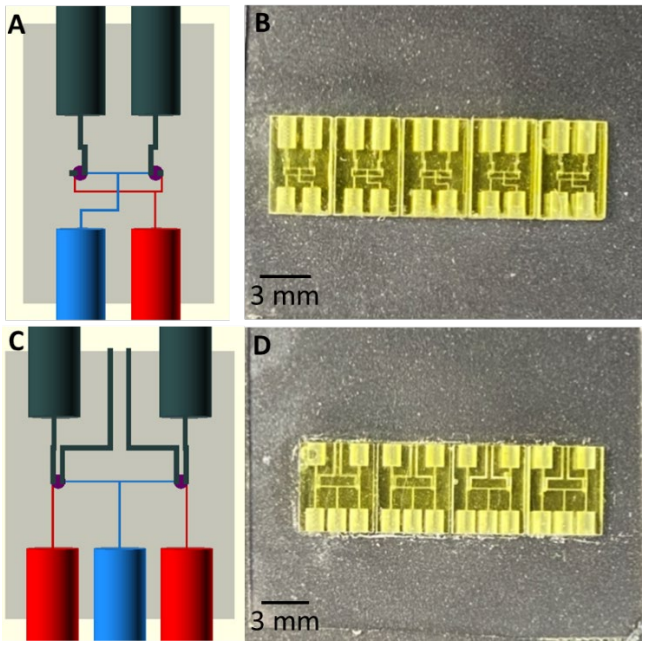

Figure 4.8. Simple devices for testing experimental conditions transitioning from PDMS devices to 3D printed valves and channels. Devices contain pneumatic valve control lines (dark gray), two pneumatic valves (purple), one sample input line (blue) and either one or two waste lines (red). (A-B) Schematic and photograph of the original test device with one input and one output. (C-D) Schematic and photograph of the modified test device with one input and two outputs.

were able to successfully flow different solutions into the device and monitor flow control by alternating which valve was open. As a preliminary step toward creating aqueous droplets in a future device, a droplet emulsion flow was monitored. Figure 4.9 includes several images demonstrating good flow control in a test device. Valve actuation was used to control flow direction and emulsion droplets were seen flowing through open channels (Figure 4.9B) and entering through the input port (Figure 4.9C-E).

With these encouraging results, the EMBL collaborators were ready to test a more complex, 4-valve system. These devices could include either one sample and one oil inlet or two sample and one oil inlet (Figure 4.10A-B). For initial testing, aqueous dyes would be used in the place of cancer or drug analytes. Similar to the 2-valve test device, fluid flow would be driven continuously by syringe pumps, and the direction of flow would be controlled by pneumatic

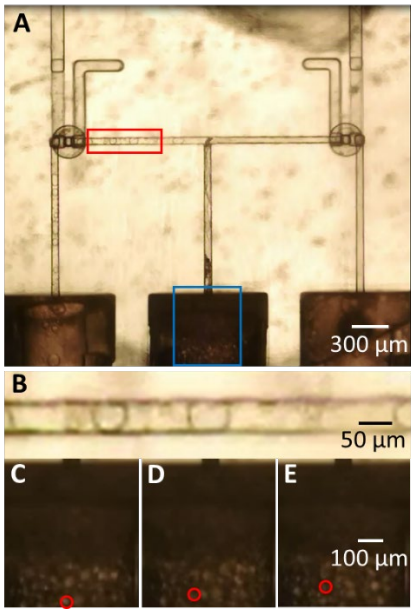

Figure 4.9. Aqueous droplet emulsion flow through a 2-valve test device. (A) Photograph of the emulsion flow through the right-side channels while flow in left-side channels is halted by closing the left valve. (B) Zoomed view from the red box showing stationary emulsion droplets in the microfluidic channels. (C-E) Zoomed view of the blue box showing the movement of emulsion droplets through the port into the microfluidic channels. Images are taken 200 ms apart. The red circle tracks the position of a single emulsion droplet, showing fluid flow. Images obtained from Dr. Ramesh Utharala of EMBL.

valves. Subsequently, the requested designs from EMBL (Figure 4.10A-B) were translated into 3D CAD designs (Figure 4.10C-D) and devices were 3D printed (Figure 4.10E-F).

It was anticipated that these 4-valve devices could be used to establish conditions for droplet formation, fluid control, and mixing, but these 3D printed devices did not fully allow for this testing. The PEGDA bulk material used for 3D printing was too hydrophilic to allow for aqueous droplet formation. Although all channels and valves functioned as designed, the testing was incomplete, and no droplet formation could be obtained with these microfluidic devices.

Even though droplet formation was not possible in the 4-valve devices, the EMBL collaborators and I still chose to test the 3D printing and control of more complex designs. Specifically, we wanted to test general flow and valve control in a 4-analyte input (in addition to oil), 8-valve 3D printed device. Several iterations of this device, shown in Figure 4.11, were

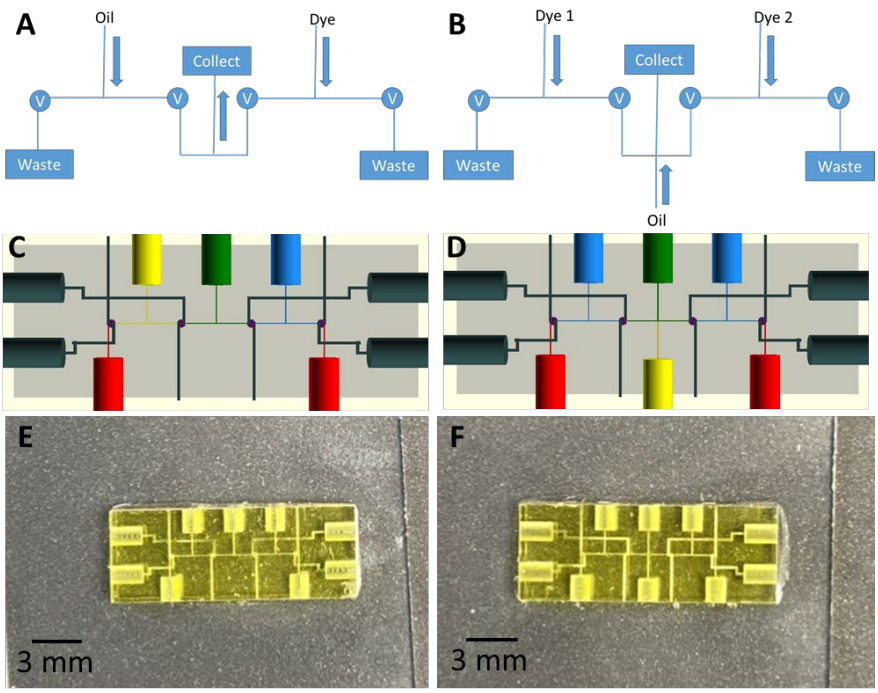

Figure 4.10. Four-valve devices for testing of droplet formation by combining oil and aqueous dye flows. (A-B) Drawing of devices with labels for flow directions and fluid types. The designs incorporate an oil input and either one or two dye inputs. (C-D) Schematics of designed devices showing connection ports and channels for oil input (yellow), sample input (blue), pneumatic connections (dark gray), valves (purple), droplet output (green), and waste output (red). (E-F) Photographs of 3D printed devices.

designed and created. The fluidic portion of these devices condensed the original PDMS chip design (Figure 4.7A) from a ~10 cm^2 device with long routing channels and serpentines into a multi-layer "plus"-shaped design that was <1 cm^2 (Figure 4.11A). The fluidic and pneumatic connection ports for this design were originally routed vertically (Figure 4.11B-C) to maintain simplicity of channel connections and a condensed surface area. The EMBL collaborators found it difficult to glue tubing into these ports due to their high surface density, so a second, similar device was designed and printed wherein the fluidic and pneumatic connection ports were located horizontally on the sides of the devices (Figure 4.11D-F). While this design addressed the issues from the previous layout, there was still difficulty interfacing with these ports. In response, I created deeper ports to help keep the tubing inside the prints during the gluing

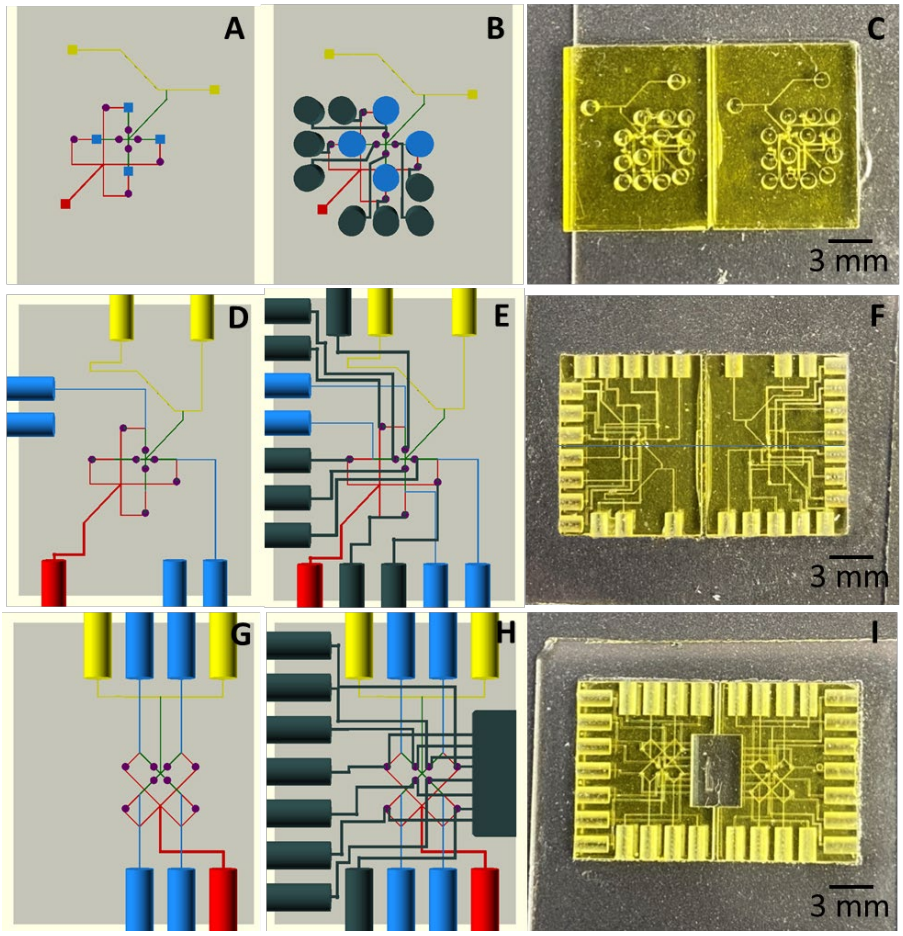

Figure 4.11. Three iterative designs for five-input (one oil, four analyte), eight-valve 3D printed microfluidic devices. For each design, the first schematic shows only the fluidic elements including oil inputs and channels (yellow), sample inputs and channels (blue), valves (purple), waste channels and valves (red), and sample-to-oil connection channels (green). In the second schematic, pneumatic valve connections are also visible (dark gray). Finally, a photograph of each type of 3D printed device is also included. (A-C) Initial design for an eight-valve device incorporating vertical connection ports and a plus-shaped fluidic input/output structure. (D-F) An updated design that still uses the plus-shaped fluidic structure but incorporates a more complex pneumatic control system to allow for horizontal connection ports. (G-I) A further improved design which rotates the plus-shaped fluidic structure in order to simplify the arrangement of fluidic and pneumatic connections. This design further incorporates a void region in the center of the design for ease of sealing pneumatic flushing channels.

process; I also increased the symmetry of the connection ports to simplify user interaction (Figure 4.11G-I). This final 8-valve design appeared to have most of the desirable features of the PDMS devices used in former studies. To date, only limited testing has been performed for valve function and fluid flow, but more extensive testing is anticipated in the coming months as the

EMBL collaborators become more expert in 3D printing and are able to use hydrophobic, biocompatible resins for the creation of their droplet microfluidic devices.

4.4 References

1. Zhang, X.; Haswell, S. J. Materials matter in microfluidic devices. *MRS Bulletin* **2006,** *31,* 95-99.

2. Baharudin, L. Microfluidics: fabrications and applications. *Instrum. Sci. Technol.* **2008,** *36,* 222-230.

3. Aurigemma, J.; Chandrasekharan, S.; Nersessian, N. J.; Newstetter, W. Turning experiments into objects: the cognitive processes involved in the design of a lab-on-a-chip device. *J. Eng. Educ.* **2013,** *102,* 117-140.

4. Keyes, R. W. Miniaturization of electronics and its limits. *IBM J. Res. Develop.* **1988,** *32,* 24-28.

5. Lundstrom, M. Moore's law forever? *Science* **2003,** *299,* 210-211.

6. Biswas, A.; Bayer, I. S.; Biris, A. S.; Wang, T.; Dervishi, E.; Faupel, F. Advances in top-down and bottom-up surface nanofabrication: techniques, applications, and future prospects. *Adv. Colloid Interface Sci.* **2012,** *170,* 2-27.

7. Rothemund, P. W. K. Folding DNA to create nanoscale shapes and patterns. *Nature.* **2006,** *440,* 297-302.

8. Andersen, E. S.; Dong, M.; Nielsen, M. M.; Jahn, K.; Subramani, R.; Mamdouh, W.; Golas, M. M.; Sander, B.; Stark, H.; Oliviera, C. L. P.; Pedersen, J. S.; Berkedal, V.; Besenbacher, F.; Gothelf, K. V.; Kjems, J. Self-assembly of a nanoscale DNA box with a controllable lid. *Nature* **2009,** *459,* 73-76.

9. Douglas, S. M.; Dietz, H.; Liedl, T.; Högberg, B.; Graf, F.; Shih, W. M. Self-assembly of DNA into nanoscale three-dimensional shapes. *Nature* **2009,** *459,* 414-418.

10. Pearson, A. C.; Liu, J.; Pound, E.; Uprety, B.; Woolley, A. T.; Davis, R. C.; Harb, J. N. DNA origami metallized site specifically to form electrically conductive nanowires. *J. Am. Chem. Soc.* **2012,** *116,* 10551-10560.

11. Liu, J.; Uprety, B.; Gyawali, S.; Woolley, A. T.; Myung, N. V.; Harb, J. N. Fabrication of DNA-templates Te and Bi_2Te_3 nanowires by galvanic displacement. *Langmuir* **2013,** *29,* 11176-11184.

12. Uprety, B.; Gates, E. P.; Geng, Y.; Woolley, A. T.; Harb, J. N. Site-specific metallization of multiple metals on a single DNA origami template. *Langmuir* **2014,** *30,* 1134-1141.

13. Weichelt, R.; Ye, J.; Banin, U.; Eychmüller, A.; Seidel, R. DNA-mediated self-assembly and metallization of semiconductor nanorods for the fabrication of nanoelectronic interfaces. *Chem. Eur. J.* **2019,** *25,* 9012-9016.

14. Aryal, B. R.; Ranasighe, D. R.; Westover, T. R.; Calvopiña, D. G.; Davis, R. C.; Harb, J. N.; Woolley, A. T. DNA origami mediated electrically connected metal-semiconductor junctions. *Nano Res.* **2020,** DOI: 10.1007/s12274-020-2672-5.

15. Mohammed, A. M.; Šulc, P.; Zenk, J.; Schulman, R. Self-assembling DNA nanotubes to connect molecular landmarks. *Nature Nano.* **2017,** *12,* 312-316.

16. McDonald J. C.; Duffy, D. C.; Anderson, J. R.; Chiu, D. T.; Wu, H.; Schueller, O. J. A.; Whitesides, G. M. Fabrication of microfluidic systems in poly(dimethylsiloxane). *Electrophoresis* **2000,** *21,* 27-40.

17. Vallee, A.; Humblot, V.; Pradier, C. Peptide interactions with metal and oxide surfaces. *Acc. Chem. Res.* **2010,** *43,* 1297-1306.

18. Seto, H.; Yamishita, C.; Kamba, S.; Kondo, T.; Hasegawa, M.; Matsuno, M.; Ogawa, Y.; Hoshino, Y.; Miura, Y. Biotinylation of silicon and nickel surfaces and detection of streptavidin as biosensor. *Langmuir* **2013,** *29,* 9457-9463.

19. US Food and Drug Administration. As You Age: You and Your Medicines. www.fda.gov/drugs/drug-information-consumers/you-age-you-and-your-medicines (accessed May 30, 2020).

20. Kleyn, P. W.; Vesell, E. S. Genetic variation as a guide to drug development. *Science* **1998,** *281,* 1820-1821.

21. Madian, A. G.; Wheeler, H. E.; Jones, R. B.; Dolan, M. E. Relating human genetic variation to variation in drug responses. *Trends Genet.* **2012,** *28,* 487-495.

22. Voegenberg, F. R.; Barash, C. I.; Pursel, M. Personalized medicine. Part 1: evolution and development into theranostics. *P&T.* **2010,** *35,* 560-576.

23. Scott, S. A. Personalizing medicine with clinical pharmacogenetics. *Genet. Med.* **2011,** *13,* 987-955.

24. Relling, M. V.; Evans, W. E. Pharmacogenomics in the clinic. *Nature* **2015,** *526,* 343-350.

25. Garnett, M.; J.; Edelman, E. J.; Heidorn, S. J.; Greenman, C. D.; Dastur, A.; Lau, K. W.; Greninger, P.; Thompson, I. R.; Luo, X.; Soares, J.; Liu, Q.; Iorio, F.; Surdez, D.; Chen, L.; Milano, R. J.; Bignell, G. R.; Tam, A. T.; Davies, H.; Stevenson, J. A.; Barthorpe, S.; Lutz, S. R.; Kogera, F.; Lawrence, K.; McLaren-Douglas, A.; Mitropoulos, X.; Mironenko, T.; Thi, H.; Richardson, L.; Zhou, W.; Jewitt, F.; Zhang, T.; O'Brien, P.; Boisvert, J. L.; Price, S.; Hur, W.; Yang, W.; Deng, X.; Butler, A.; Choi, H. G.; Chang, J. W.; Baselga, J.; Stamenkovic, I.; Engelman, J. A.; Sharma, S. V.; Delattre, O.; Saez-Rodriguez, J.; Gray, N. S.; Settleman, J.; Futreal, P.; A.; Haber, D. A.; Stratton, M. R.; Ramaswamy, S.; McDermott, U.; Benes, C. H.

Systematic identification of genomic markers of drug sensitivity in cancer cells. *Nature* **2012,** *483,* 570-577.

26. Anand, G.; Akash, C.; Vaishali, J.; Ashish, J. Pharmacogenetics: current application in chemotherapy and its future trends. *Int. J. Pharm. Sci. Rev. Res.* **2019,** *56,* 59-65.

27. Eduati, F.; Utharala, R.; Madhavan, D.; Neumann, U. P.; Longerich, T.; Cramer, T; Saez-Rodriguez, J.; Merten, C. A. A microfluidics platform for combinatorial drug screening on cancer biopsies. *Nat. Commun.* **2018,** *9,* 2434.

28. Merten, C.; Tseng, Q.; Utharala, R.; Frese, L. Microfluidic sorting device. US Patent 10,569,272, Feb. 25, 2020.

29. Gong, H.; Bickham, B. P.; Woolley, A. T.; Nordin, G. P. Custom 3D printer and resin for 18 x 20 µm microfluidic flow channels. *Lab Chip.* **2017,** *17,* 2899-2909.

30. Gong, H.; Woolley, A. T.; Nordin, G. P. 3D printed selectable dilution mixer pumps. *Biomicrofluid.* **2018,** *12,* 060401.

5. CONCLUSIONS AND FUTURE WORK

5.1 PTB Biomarker Separations

Chapter 2 described the development of an electrophoretic method to separate six preterm birth (PTB) biomarkers. The separation was an important step towards the development of a complete PTB diagnostic and demonstrated the capability of microchip electrophoresis as a separation and detection method for this biomarker panel. The ability to separate six protein and peptide biomarkers ranging from 2 to 470 kDa in ~1 min shows high potential for the rapid analysis of the entire PTB biomarker panel on a single microfluidic device. This separation was also the first microfluidic assay to include the majority of the PTB biomarkers in a single analysis.

While this six biomarker separation showed many important capabilities, several improvements are needed before a complete PTB risk diagnostic can be realized including: analysis of all nine PTB biomarkers, transition from conventional fabrication to 3D printing, incorporation of valves and pumps for greater automation and fluidic control, and integration with upstream sample preparation. Each of these improvements is addressed in the subsequent paragraphs.

As noted in Chapter 2, three of the PTB biomarkers from the published panel[1] were not included in the analysis. Since publication of that work, my lab colleagues been able to form the thrombin-antithrombin complex and perform a seven-biomarker separation.[2] Additionally, other group members are starting to perform mass spectrometric analysis on control and clinical maternal blood serum samples to determine which defensins are relevant to PTB risk. This testing will allow for future inclusion of the defensin biomarker in an electrophoretic separation.

Recently, the first microchip electrophoretic separations were performed in 3D printed microfluidic devices, including analysis of three PTB biomarkers,[3] and the seven-biomarker separation will be performed in 3D printed devices soon. This transition to 3D printed devices allows for fast device fabrication and simple incorporation of valves and pumps for automation. I have begun integrating these valves and pumps, but valve function in the presence of an applied voltage was inconclusive. To allow future testing of these valves, I designed two t-shaped electrophoresis devices: one with a valve on each arm of the device (Figure 5.1A) and the other including these valves and a pump on the injection channel (Figure 5.1B). These designs should allow for optimization of valve function with an applied voltage, pneumatic-pump driven injections, and later, easier integration with upstream sample preparation methods.

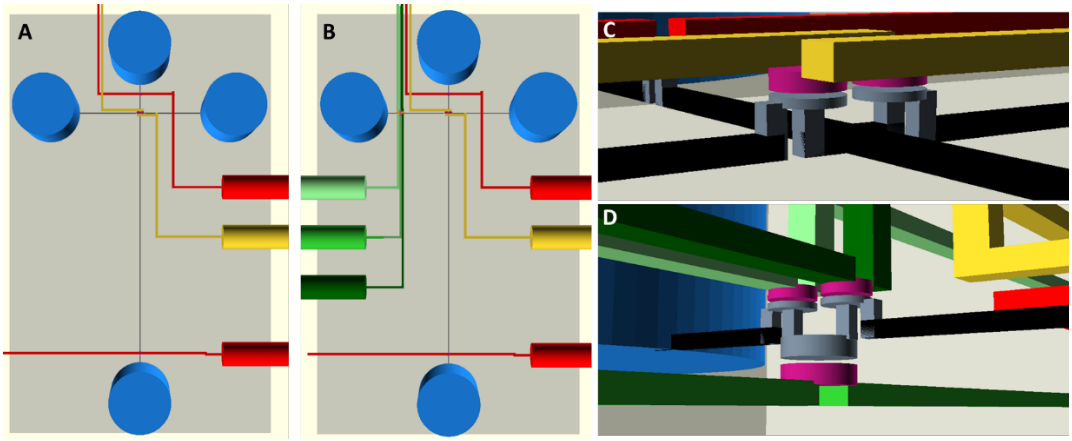

Figure 5.1. Schematics for 3D printed microchip electrophoresis devices with four reservoirs (blue), t-shaped fluidic channels (black), and pneumatic valve control channels and ports (red and yellow). (A) Electrophoresis microchip with valves on each channel. (B) Electrophoresis microchip with valves and a pneumatically controlled pump (green) on the injection channel. (C) Zoomed image of the valves near the fluid channel intersection. (D) Zoomed image of the fluid pump from the part B schematic.

Integration of sample preparation with microchip electrophoresis has been performed previously in Woolley's lab;[4-5] however, these studies were performed in conventionally fabricated devices and have only included one or two PTB biomarkers. Since that time, sample

preparation has also been performed using immunoaffinity monoliths[6] and reversed-phase monoliths (Chapter 3) in 3D printed devices. These monoliths will subsequently be combined on a single 3D printed device with an electrophoresis channel. Such a device should be capable of performing a complete analysis of maternal blood serum and diagnosing PTB risk. It would also have the potential to be adapted for other biomarker analyses.

5.2 Solid-Phase Extraction and On-Chip Labeling of PTB Biomarkers

The work in Chapter 3 described the development of reversed-phase monoliths in 3D printed devices for the extraction, on-chip fluorescent labeling, and selective retention of PTB biomarkers. The monolith formulation chosen for these experiments selectively retained the protein and peptide biomarkers while eluting excess fluorescent dye. Despite the range of sizes and hydrophobicities of the nine PTB biomarkers used in this study, I was able to show good retention of seven biomarkers when sample loading was immediately followed by rinse and elution steps. When the biomarkers incubated for 30 min after loading, all nine biomarkers were successfully retained on the monolith. Importantly, this study demonstrated the first usage of all nine PTB biomarkers in a microchip analysis.

One of the disadvantages of the Chapter 3 work was that all analyte detection was performed using a fluorescent imaging system which did not allow for quantification of monolith capacity or analyte enrichment. This limitation was due to the presence of a photopolymerization byproduct in the bulk of the 3D printed device that interfered with the point detection system. This byproduct appears to be from the photoinitiator in the 3D printing resin, so I developed a new resin consisting of 0.5% avobenzone UV absorber and 2% benzoin methyl ether photoinitiator in poly(ethylene glycol) diacrylate (PEGDA). Figure 5.2 shows 3D printed devices

from both the normal resin (1% Irgacure 819, 2% 2-nitrophenyl phenyl sulfide in PEGDA) and this new formulation. The new resin yields devices that are transparent and colorless while maintaining comparable feature sizes. Although additional adjustments to the resin formulation may be needed to increase the polymer strength, initial results are promising that these devices could be used for point detection experiments.

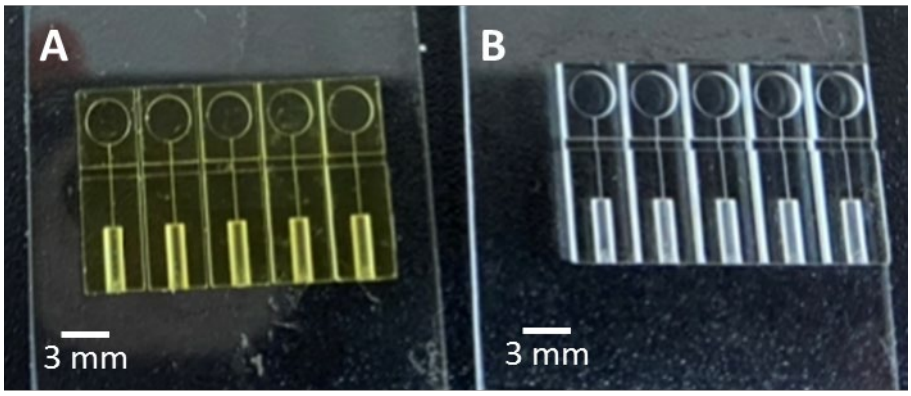

Figure 5.2. Photograph of 3D printed devices printed with the (A) normal and (B) newly formulated resins.

Similar to the electrophoretic separations described in Chapter 2, future improvements to solid-phase extraction include increased automation via incorporation of valves and pumps and integration with other sample preparation and separation elements. An immediate way to increase automation is to include multiple inlet channels with corresponding valves to open and close the channels for fluid flow (Figure 5.3A). Such a system eliminates the need for manual replacement of solvents between each step of the analysis. Increased automation can also be achieved by incorporating a pneumatic pump (Figure 5.3B). This pump would allow for controlled pumping rates and times resulting in more consistent fluid flow during experiments than can be achieved by applying vacuum. These designed valves and pumps shown in

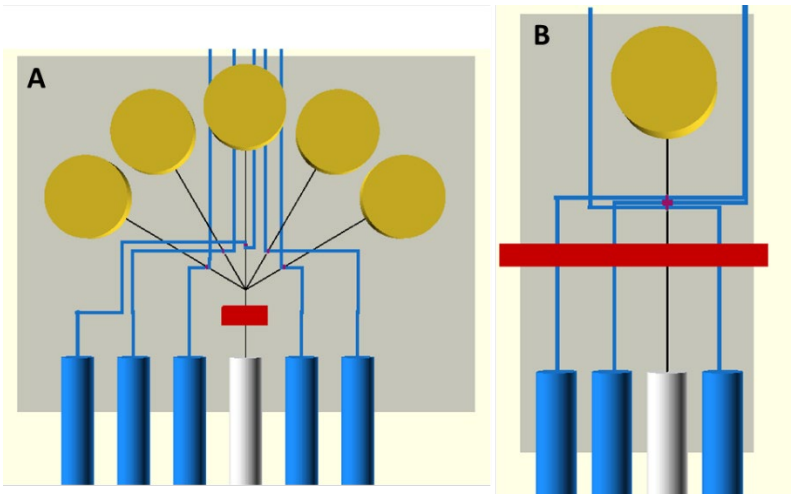

Figure 5.3. Schematics of microfluidic devices to increase the automation of a solid-phase extraction system. Devices include fluidic channels (black), fluid reservoirs (yellow), a waste port (light gray), pneumatic valve control channels and ports (blue), and a monolith polymerization window (red). (A) Design for a microfluidic device with five inlets that combine to flow through a single monolith. (B) Design for a device with pneumatic pump driven flow.

Figure 5.3 will allow for easier integration of this monolith extraction system with upstream sample preparation and downstream separation.

5.3 Fluidic Devices for DNA Nanowire Growth and Characterization

In Chapter 4.2, I described the design, fabrication, and improvement of fluidic devices for DNA nanotube growth, metallization, and characterization. These devices utilized glass, polydimethylsiloxane (PDMS), gold, and nickel to create a fluidic platform for DNA tiles to be seeded and grown into nanotubes as scaffolds for nanowire formation. The fluidic devices mainly focused on establishing initial conditions for fluidic channel formation and the selective attachment of DNA seeds to gold and nickel electrodes for nanotube growth. The JHU collaborators were able to successfully assemble glass-PDMS devices fabricated at BYU, seed DNA, and image my gold “patch electrode” devices.

While conditions for selective attachment of DNA seeds to the gold electrodes followed well-established procedures (thiol attachment), a different method is still needed to attach DNA seeds to nickel electrodes. As mentioned in Chapter 4.2.3, several possible methods were proposed, but none have been tested to determine if the seeding attachment is sufficient for DNA nanotube growth. After an appropriate method is determined, this process will be combined with the gold electrode seeding for DNA nanotube growth between the two different electrodes. For this experiment, I planned to fabricate patch electrode devices with half gold and the other half nickel (Figure 5.4). Such fabrication would be performed by repeating the photolithography and metal deposition steps described in Chapter 4.2.2 for each metal. Proper care must be taken during photolithography to align the fabricated layers so that the desired gap between the electrodes (5-10 μm) is obtained accurately and consistently.

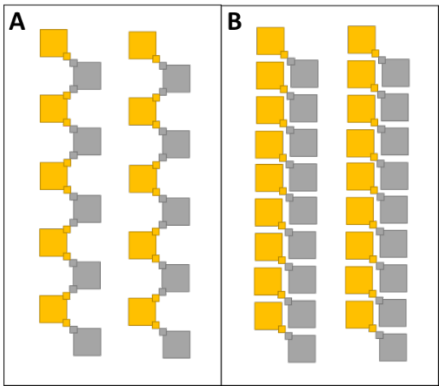

Figure 5.4. Schematics of patch electrode devices with electrode junctions comprised of 5-10 μm gaps between gold and nickel electrodes on glass slides. (A) Zig-zag patch electrode device. (B) Packed patch electrode design.

The final integrated device for DNA nanotube growth and nanowire formation includes gold and nickel electrode junctions within fluidic channels. My design and expected fabrication process are shown in Figure 5.5. Each gold and nickel electrode has two external connection points to enable testing of electrode fidelity prior to nanowire growth. Furthermore, each

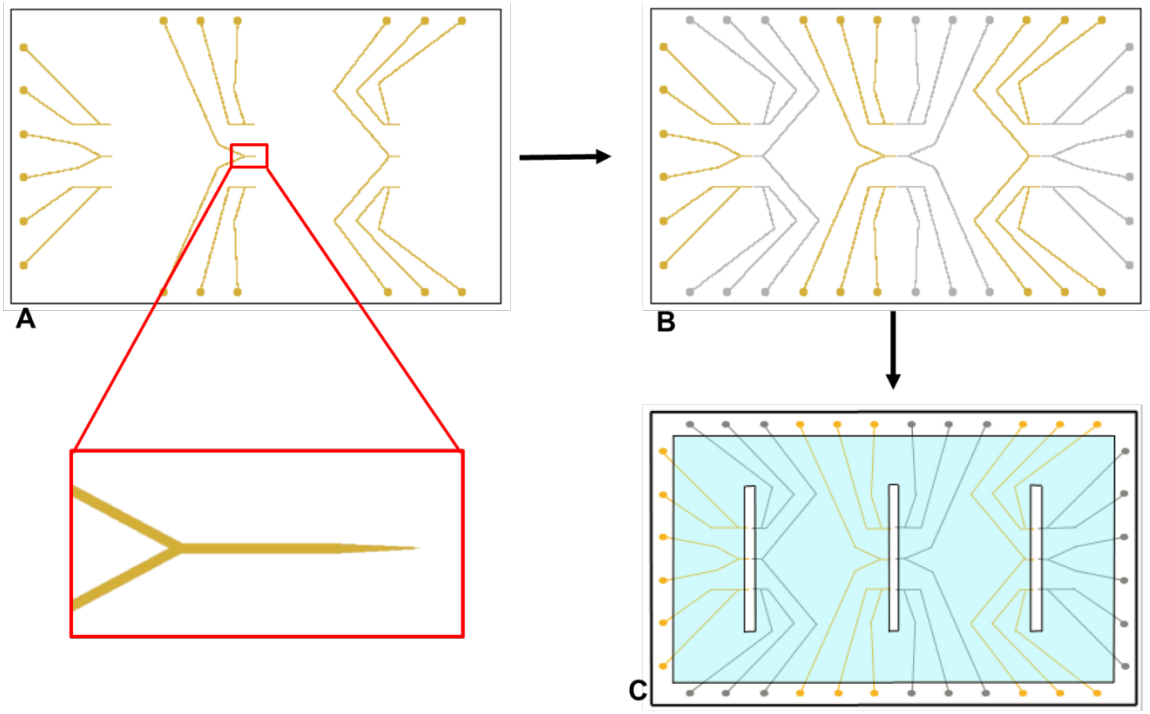

Figure 5.5. Fabrication of integrated two-metal electrode fluidic devices for DNA nanotube growth and nanowire formation and characterization. (A) A glass slide is patterned with gold electrodes, each with two electrical connection points and tapering to a point in the channel regions. (B) The pattern is turned 180° and corresponding nickel electrodes are also patterned onto the glass. (C) Finally, a smaller glass slide with fluidic channels patterned in PDMS on the surface is bonded onto the glass-metal surface to enclose the electrode junctions.

electrode tapers to a point within the channel, which is intended to limit the number of nanowires connecting each junction. It is anticipated that sharp tapering will only allow one nanowire to span the gold-nickel junction, allowing electrical conductivity measurements for a single nanowire. If realized, this work would comprise a significant contribution to the future of self-assembled nanoelectronics and the controlled placement of nanowires.

5.4 3D Printed Multi-Inlet Droplet Generator Devices

Chapter 4.3 describes a PDMS multi-inlet droplet generator device that enabled high-throughput testing of cancer biopsy cells with a variety of drug cocktails. My work on this project focused on the transition of such a device from PDMS soft lithography fabrication to a

3D printed format. Several design iterations resulted in microfluidic devices ranging from one input and two valves up to five inputs and eight valves. Initial testing of these devices showed good fluid flow through the channels and flow direction control using pneumatic valves.

One of the main disadvantages of the 3D printed devices was the inability to form aqueous droplets within a hydrophobic oil phase. This was primarily due to the hydrophilic nature of the PEGDA material that comprises the 3D printed devices. Since these devices are also intended to perform cell sorting, resin material biocompatibility is also desirable. Since initial fabrication of these devices, researchers at BYU have now developed a new 3D printing resin that is biocompatible[7] and are also developing hydrophobic resins for droplet microfluidics.

Another feature of these microfluidic devices that the EMBL collaborators often struggled with was chip-to-world interfacing. These 3D printed devices had a maximum size of 12 mm x 19 mm, significantly smaller than the >4 cm^2 PDMS chips that they were accustomed to using. Additionally, the 3D printed devices had many densely packed ports that needed external tubing affixed for fluid input and pneumatic valve control. For example, one of the 5-input, 8-valve devices shown in Figure 4.11, required connections to 15 ports, each spaced ~1.6 mm apart. Additionally, the number of required connections would only increase as the number of analyte inputs was increased. While this might be a feasible task for an experienced researcher, this prospect could be overwhelming for 3D printing initiates.

The solution to these dense, small connection ports is to relocate the ports onto a secondary interface chip interfaced to the primary chip via 3D printed gasket connections, which have been developed and tested previously with high success.[8] This system would allow all fluidic and pneumatic connection ports to be placed in a separate, reusable 3D print. Although the need to affix external tubing into a device would not be completely eliminated, an interface

chip would allow for greater spacing between connections. Additionally, the interface chip would be reusable for many primary chips, significantly reducing the number of times such gluing would need to be performed.

Once sufficient preliminary work has been performed on the previously designed devices for droplet formation for multiple analytes, the final stage of this project is to increase the number of available input ports to include more analytes simultaneously. The published PDMS device used by the EMBL collaborators included 16 analyte inputs (in addition to oil flow for droplet formation).[9] By comparison, the 3D printed device shown in Figure 4.11 was only able to accommodate four analyte inputs. However, this 4-input device was designed to be easily compounded to accommodate additional inputs.

Figure 5.6 shows a schematic of the basic "plus"-shaped design from Figure 4.11 and schematics of how this design can be compounded for 16- and 64-input microfluidic devices. Importantly, the 64-input device (Figure 5.6C) is shown to scale within the full print area of the custom 3D printer (~12 mm x 19 mm). Even with the high number of inputs in this device, about

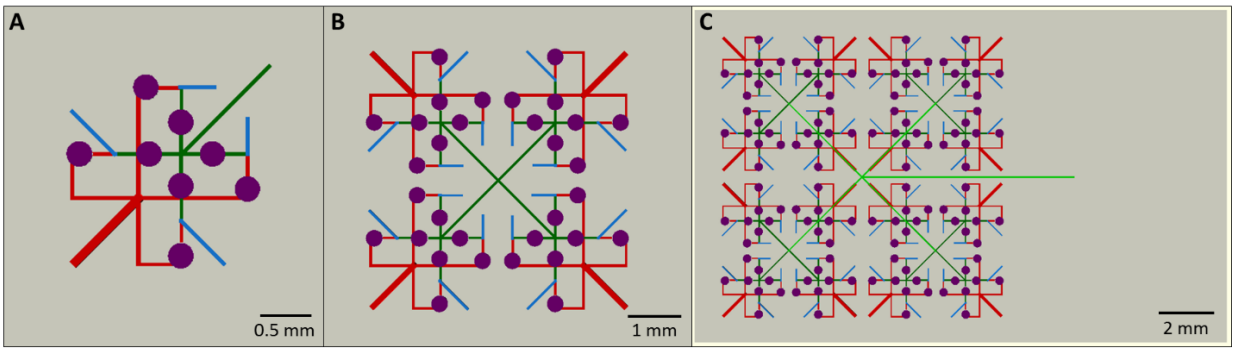

Figure 5.6. Schematics of the aqueous flow portions of multi-input droplet generator microfluidic devices containing fluid input channels (blue), valves (purple), sample-to-oil connection channels (green), and waste channels (red). (A) Basic device design from Figure 4.11 for a 4-input device. (B) Integrated design for a 16-input device. (C) Device with additional integrated units to accommodate up to 64 inputs. The design is pictured on a background to demonstrate the full print area of the 3D printer and illustrate the space still available for oil flow or other sample preparation elements.

a third of the print space is available to be filled with the oil input and flow channels as well as any additional sample preparation elements that may be desirable for an integrated analysis such as cell sorting, filtering channels, or pumps to replace the external syringe pumps currently being used. If such a device were implemented, it would surpass the original PDMS devices in small size, throughput capability, and automation. It could also be easily adapted to accommodate a variety of other drug-testing applications beyond cancer biopsies.

5.5 Concluding Remarks

Microfluidics is a powerful tool to perform analyses at lower cost, higher efficiency, or greater automation than many benchtop instruments. The variety of microfluidic device materials allows microfluidic applications to take advantage of desirable properties and microfabrication methods to obtain optimal experimental results. In this dissertation, I have described four examples of fluidic devices fabricated using hot embossing of a thermoplastic, 3D printing, and soft lithography of PDMS. Each device has applied a different analytical method including microchip electrophoresis, solid-phase extraction, DNA self-assembly, and droplet microfluidics. Finally, each of the described works also has potential for use in biological assays or bioelectronics with increased integration and automation to the current achievements.

5.6 References

1. Esplin, M. S.; Merrell, K.; Goldenberg, R.; Lai, Y.; Iams, J. D.; Mercer, B.; Spong, C. Y.; Miodovnik, M.; Simhan, H. N.; van Dorsten, P.; Dombrowski, M. Proteomic identification of serum peptides predicting subsequent spontaneous preterm birth. *Am. J. Obstet. Gynecol.* **2011,** *204,* 391.e1–8.

2. Nielsen, J. B.; Nielsen, A. V.; Carson, R. H.; Lin, H. L.; Hanson, R. L.; Sonker, M.; Mortensen, D. N.; Price, J. C.; Woolley, A. T. Analysis of thrombin-antithrombin complex formation using microchip electrophoresis and mass spectrometry. *Electrophoresis* **2019,** *40,* 2853-2959.

3. Beauchamp, M. J.; Nielsen, A. V.; Gong, H.; Nordin, G. P.; Woolley, A. T. 3D printed microfluidic devices for microchip electrophoresis of preterm birth biomarkers. *Anal. Chem.* **2019,** *91,* 7418-7425.

4. Sonker, M.; Parker, E. K.; Nielsen, A. V.; Sahore, V.; Woolley, A. T. Electrokinetically operated microfluidic devices for integrated immunoaffinity monolith extraction and electrophoretic separation of preterm birth biomarkers. *Analyst* **2018,** *143,* 224-231.

5. Sahore, V.; Sonker, M.; Nielsen, A. V.; Knob, R.; Kumar, S.; Woolley, A. T. Automated microfluidic devices integrating solid-phase extraction, fluorescent labeling, and microchip electrophoresis for preterm birth biomarker analysis. *Anal. Bioanal. Chem.* **2018,** *410,* 933-941.

6. Parker, E. K.; Nielsen, A. V.; Beauchamp, M. J.; Almughamsi, H. M.; Nielsen, J. B.; Sonker, M.; Gong, H.; Nordin, G. P.; Woolley, A. T. 3D printed microfluidic devices with immunoaffinity monoliths for extraction of preterm birth biomarkers. *Anal. Bioanal. Chem.* **2019,** *411,* 5405-5413.

7. Warr, C.; Valdoz, J. C.; Bickham, B. P.; Knight, C. J.; Franks, N. A.; Chartrand, N.; Van Ry, P. M.; Christensen, K. A.; Nordin, G. P.; Cook, A. D. Biocompatible PEGDA resin for 3D printing. *ACS Appl. Bio Mater.* **2020,** *3,* 2239-2244.

8. Gong, H.; Woolley, A. T.; Nordin, G. P. 3D printed high density, reversible, chip-to-chip microfluidic interconnects. *Lab Chip.* **2018,** *18,* 639-647.

9. Eduati, F.; Utharala, R.; Madhavan, D.; Neumann, U. P.; Longerich, T.; Cramer, T.; Saez-Rodriguez, J.; Merten, C. A. A microfluidics platform for combinatorial drug screening on cancer biopsies. *Nat. Commun.* **2018,** *9,* 2434.